Spin-up and spin-down in linearly stratified fluid over flat bottom

Mattia Romani

N° attribué par la bibliothèque

UNIVERSITÉ JOSEPH FOURIER
ECOLE DOCTORALE TERRE UNIVERS ET ENVIRONNEMENT
Spécialité: Océan, Atmosphère, Hydrologie

UNIVERSITÁ DEGLI STUDI DI TORINO
DIPARTIMENTO DI FISICA GENERALE "A. AVOGADRO"

THÈSE

pour obtenir le grade de
DOCTEUR DE L'UNIVERSITÉ JOSEPH FOURIER

DOTTORATO DI RICERCA IN FISICA
XX CICLO

SPIN-UP AND SPIN-DOWN IN LINEARLY STRATIFIED FLUID OVER FLAT BOTTOM

Thésard: **Mattia ROMANI**

Directeurs: Monsieur Joël SOMMERIA,
Monsieur Arnaldo LONGHETTO

Soutenue le **17 Mars 2008** devant le jury composé de :

Monsieur	Paul BILLANT	Examinateur,
Monsieur	Jan-Bert FLOR	Examinateur,
Monsieur	Peter READ	Rapporteur,
Madame	Marina SERIO	Examinatrice,
Monsieur	Francesco TAMPIERI	Rapporteur

N° attribuito dalla biblioteca

UNIVERSITÁ DEGLI STUDI DI TORINO
DIPARTIMENTO DI FISICA GENERALE "A. AVOGADRO"

UNIVERSITÉ JOSEPH FOURIER
ECOLE DOCTORALE TERRE UNIVERS ET ENVIRONNEMENT
Spécialité: Océan, Atmosphère, Hydrologie

DOTTORATO DI RICERCA IN FISICA
XX CICLO

THÈSE

pour obtenir le grade de
DOCTEUR DE L'UNIVERSITÉ JOSEPH FOURIER

SPIN-UP AND SPIN-DOWN IN LINEARLY STRATIFIED FLUID OVER FLAT BOTTOM

Dottorando: **Mattia ROMANI**

Relatori: Prof. Arnaldo LONGHETTO,
Prof. Joël SOMMERIA

Sostenuta il **17 Marzo 2008** davanti alla commissione composta da :

Prof.	Paul BILLANT	Esaminatore,
Prof.	Jan-Bert FLOR	Esaminatore,
Prof.	Peter READ	Controrelatore,
Prof.ssa	Marina SERIO	Esaminatrice,
Prof.	Francesco TAMPIERI	Controrelatore

Abstract

We present an experimental investigation of spin-up and spin-down for a linearly stratified fluid over flat bottom. This study has revealed two very different behaviors depending on the value of the Burger number, a measure of the relative importance of stratification and Coriolis effects.

For Burger number > 1, the flow remains remarkably axisymmetric in the bulk of the fluid in spite of the large Reynolds number, and no instability is observed. The confinement of the secondary circulation due to the stratification is well described by the theory of Walin (1969). The theory was scaled using the homogeneous spin-up time scale and thus viscous-diffusion effects were omitted. However, the non-uniform spin-up of the interior gives rise to vertical flow gradients which introduce viscous-diffusion sooner than anticipated by the theory. Consequently, the comparison with the theory shows a faster rate of decay of the azimuthal flow even over the shorter spin-up time scale. An attempt to provide an easy procedure to include vertical diffusion of momentum in the Walin's analytical solution is proposed. The early stage of the flow is correctly described by the addition of viscous-diffusion effects, but the faster decay rate of the measurements persists over intermediate times.

For Burger numbers < 1, the flow behavior is substantially different. The deeper penetration of the secondary circulation notably reduces the vertical flow gradients. The decay of the azimuthal velocity is almost vertically uniform and the development of non-axisymmetric disturbances is observed. The flow decay is well described in the early stage by the Walin's theory, but after the initial agreement the experimental results decay slower than the theoretical predictions. The discrepancies correspond to the onset of the instability, at variance with Smirnov *et al.* (2005) claiming that the formation of large-scale eddies provides an additional mechanism for the transport of angular momentum from the solid boundaries. Nevertheless, the radial transport of momentum from the sidewall boundary layer may account for the stronger decay observed over long times. The classical Eady's model is shown to be consistent with the structure of the observed waves in our experimental investigation. Its derivation by Smirnov *et al.* (2005) in cylindrical geometry assuming reliable initial conditions allows a reasonable estimation of the growth rate, which was untenable in the classical theory. Indeed, the mechanism of baroclinic instability becomes the most plausible explanation for the existence of the long-wave instability in spin-up or spin-down process.

Key-words: spin up/down; rotating flow; stratified flow

Résumé

Nous présentons une étude expérimentale du ”spin-up” et ”spin-down” en présence d'une stratification linéaire sur un fond plat. Deux comportements très différents ont été mis en évidence selon la valeur du nombre de Burger, une mesure de l'importance relative de la stratification et des effets de Coriolis.

Pour des nombres de Burger supérieurs à un, l'écoulement est remarquablement axisymétrique en dehors des couches limites, et aucune instabilité n'est observée malgré le grand nombre de Reynolds. Le confinement de la circulation secondaire du à la stratification est bien décrit par la théorie de Walin (1969), qui omet la viscosité. Cependant, le ”spin-up” non-uniforme de l'intérieur provoque des gradients verticaux d'écoulement sensibles aux effets visqueux. En conséquence, la comparaison avec la théorie montre un taux plus rapide de décroissance de l'écoulement azimutal. On propose une prise en compte simplifié de la diffusion verticale de quantité de mouvement dans la solution analytique de Walin. Aux temps courts, l'écoulement initial est correctement décrit par l'addition d'effets diffusifs visqueux, mais l'écart entre la théorie et les mesures persiste pour des temps intermédiaires.

Pour des nombres de Burger inférieurs à un, le comportement de l'écoulement est très différent. La pénétration plus profonde de la circulation secondaire réduit notamment les gradients verticaux de vitesse. La décroissance de la vitesse azimutale est presque verticalement uniforme et le développement des perturbations non-axisymmetriques est observé. Le déclin initial est bien décrit par la solution analytique. Cependant, la décroissance expérimentale est plus faible que la prédiction théorique pour des temps plus longs. L'écart correspond à l'apparition d'une instabilité. Ce résultat est en contradiction avec Smirnov et al. (2005), qui affirment que la formation de tourbillons à grande échelle fournit un mécanisme supplémentaire pour transporter le moment angulaire des frontières vers l'intérieur. En revanche, le transport radial de quantité de mouvement des couches limites latérales vers l'intérieur expliquerait la plus forte décroissance expérimentale aux temps longs. Le modèle classique d'Eady est cohérent avec les structures expérimentales observées. En considérant une dérivation de ce modèle par Smirnov et al. (2005), ainsi que des conditions initiales pertinentes, nous trouvons une estimation raisonnable du taux de croissance de l'instabilité, ce qui n'aurait pas été le cas avec la théorie classique d'Eady. Ainsi, le mécanisme de l'instabilité barocline est l'explication la plus plausible pour l'existence d'une instabilité à grand nombre d'onde dans les processus de ”spin-up” et ”spin-down”.

Mots-clés: spin up/down; fluide en rotation; fluide stratifié

Riassunto

Questa tesi presenta uno studio sperimentale di ”spin-up” e ”spin-down” nel caso di fluido linearmente stratificato in presenza di fondo piatto. Due comportamenti molto differenti sono messi in evidenza a seconda del valore del numero di Burger, che esprime l'importanza relativa della stratificazione rispetto alla forza di Coriolis.

Nel caso di numero di Burger minore di uno, il flusso rimane assisimmetrico nella regione interna, e non sono osservate instabilitá. Il confinamento della circolazione secondaria indotto dalla stratificazione é ben descritto dalla teoria di Walin (1969). Questa teoria é derivata scalando le equazione del moto con il tempo scala di ”spin-up” in caso omogeneo, procedura che omette gli effetti viscosi. Tuttavia, lo ”spin-up” non uniforme nella regione interna origina gradienti di velocitá lungo la direzione verticale sensibili alla diffusione viscosa. Di conseguenza, il confronto con la teoria mostra una rateo di decrescita piú rapido del flusso azimutale giá nel breve tempo scala di ”spin-up”. Viene quindi proposta una procedura non-rigorosa di inclusione degli effetti viscosi nella soluzione di Walin. Ciò permette di descrivere correttamente l'evoluzione durante la fase iniziale, sebbene il rateo di decrescita piú rapido persista su tempi scala intermedi.

Nel caso di numero di Burger maggiore di uno, il comportamento del flusso é sostanzialmente differente. La maggior penetrazione della circolazione secondaria nella regione interna riduce sensibilmente i gradienti verticali di velocitá. La decrescita della velocitá azimutale é pressochè verticalmente uniforme e perturbazioni non-assisimmetriche si originano. La decrescita del flusso é ben descritta dalla teoria di Walin durante la fase inziale, ma successivamente i risultati sperimentali decrescono meno rapidamente della predizione teorica. Le incongruitá corrispondono all'insorgenza di instabilitá, in disaccordo con Smirnov *et al.* (2005) secondo cui la formazione di vortici a grande scale fornisce un meccanismo aggiuntivo per il trasporto di quantitá di moto dalla frontiera. Ciò nonostante, il trasporto radiale di quantitá di moto appare essere responsabile della consistente decrescita osservata su tempi scala lunghi. Il modello classico di Eady risulta consistente con la struttura della perturbazione osservata. La sua derivazione ad opera di Smirnov *et al.* (2005) in geometria cilindrica, tenendo conto di condizioni iniziali appropriate, permette una stima corretta del rateo di crescita dell'instabilitá, inattendibile per mezzo della sola teoria classica. In conclusione, il meccanismo di instabilitá baroclina appare essere la spiegazione piú plausibile per l'esistenza di instabilitá a grande scala durante il processo di ”spin-up” o ”spin-down”.

Parole chiave: spin up/down; fluido in rotazione; fluido stratificato

Contents

List of notations

$(\hat{i}_r, \hat{i}_\theta, \hat{k})$	cylindrical unit vectors
$(\hat{i}_x, \hat{i}_y, \hat{k})$	cartesian unit vectors
(r, θ, z)	cylindrical coordinates
(u, v, w)	cartesian velocity components
(u_r, u_θ, w)	cylindrical velocity components
(x, y, z)	cartesian coordinates
χ	thermal diffusivity
$\Delta\Omega$	angular velocity change
δ	aspect ratio
δ_e	boundary layer thickness
ϵ	Rossby number
κ	salt diffusivity
λ	zonal wavelength
ν	kinematic viscosity
ψ, Ψ, ϕ	stream functions
ρ	density
σ	Schmidt number
τ_s	homogeneous spin-up time scale

Chapter 1

Introduction

An understanding of the combined effects of rotation and stratification is fundamental to geophysical flows. When the fluid is homogeneous and the Coriolis force is large compared with the viscous and inertia forces, the Taylor-Proudman (1917) [72] theorem (Eq.n (2.11)) states that the velocity is uniform along the direction of the rotation vector. However, if the fluid is stratified the constraints which the Taylor-Proudman theorem imposes on the flow do not apply, and the fluid can support significant vertical shears even if the rotation axis is vertical.

When a column of fluid is stretched or squeezed in a rotating fluid, changes in vorticity occur (¶ 2.1). A stable density stratification inhibits vertical motions, therefore altering drastically the flow dynamics. Moreover, horizontal variations in density can also produce many interesting motions in a rotating fluid. These horizontal density gradients may either be due to external boundary conditions or arise from the internal dynamics in response to some forcing. They provide a source of energy which may be released under appropriate conditions, the so called baroclinic instability (¶ 2.5), to produce a wide range of important phenomena.

This thesis concerns the general process by which a fluid in a container adjusts itself to time-dependent boundary conditions. The fluid, density stratified, is assumed to be in solid body rotation in a container over flat bottom. The angular velocity of the container is then impulsively modified, generating a relative flow (*primary circulation*) which adjusts itself in time to the new angular velocity of the boundaries. If the angular velocity of the container is increased (decreased) the process whereby this adjustment occurs has come to be known as spin-up (spin-down).

If the impulsive change in angular velocity is much smaller than the final angular velocity of the container, the process is called *incremental* spin-up and the advective terms in the equations of motion are negligible. Note that the angular velocity change may also be a slowly varying function of time, resulting in a process called *secular* spin-up.

The spin-up of a fluid in a container describes an adjustment mechanism which arises frequently in both the atmosphere and oceans (e.g., wind-driven flows). In particular, winds blowing in the along-shore direction with the coastline on the left when facing downstream cause upwelling in the northern hemisphere (Fig. 1.1). The cross-frontal exchange of shelf and

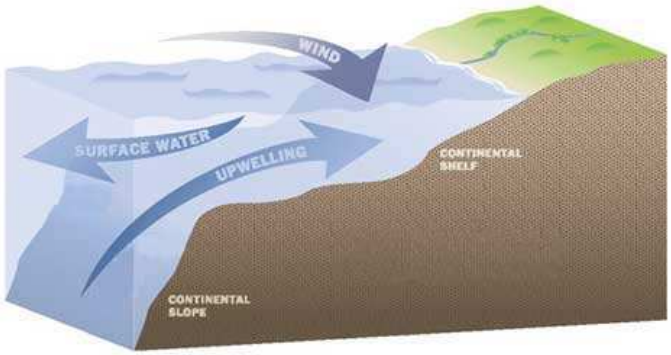

Fig. 1.1: Where Ekman transport (¶ 3.1.2) moves surface waters away from the coast, these are replaced by denser water that wells up from below in the process known as *coastal upwelling*. Note that the *continental shelf* is the extended perimeter of each continent. The shelf usually ends at a point of increasing slope, named *shelf break*. The sea floor below the break is the *continental slope*.

slope waters at the shelf break is an important aspect of the general problem of understanding the transport of heat, salt, pollutants, and nutrients between the shelf and the deep ocean. A coastal front is susceptible to baroclinic instability revealed in the form of frontally trapped unstable waves motions, which are responsible for along-front variability and intensified cross-shelf transport (Barth (1989) [2]).

Certainly, in natural conditions the bottom topography is never flat, but this must not be seen necessarily as a restriction. In fact, a better understanding of the flow dynamics in simple geometry such as a circular cylinder is essential for the development of coastal oceanic models, where various topographic features (e.g., continental slopes, canyons, etc.) modify the flow behavior (Smirnov *et al.* (2005) [68]).

The spin-up problem is also central to an understanding of the dissipative mechanisms for large scale atmospheric and oceanic motions (Pedlosky (1967) [56]), where rotational

effects are dominant (e.g., Ekman layer arrest (Fig. 1.2)).

Moreover, spin-up theory has provided justification for a simple parametrization of the bottom boundary friction in geophysical flows, essentially as a surface drag linear in the geostrophic velocity. Numerical and analytical models of large scale flows thus often assumed that relative vorticity decays exponentially, rather than resolve the boundary layer itself (MacCready & Rhines (1991) [48]).

1.1 Pioneering Works

The fundamental dynamics of the viscous boundary layer established in a rotating system when a current in geostrophic balance flows above a rigid boundary was discussed since 1905 by the Swedish oceanographer Ekman [15]. He was even the first to perform spin-up experiments, changing abruptly from zero to some finite value the rotation rate of a container filled with fluid (Ekman (1906) [16]). Ekman suspended a light aluminium vane at mid-depth in homogeneous and stably stratified fluids and measured the rate at which momentum was transferred from the boundary layer to the level at which the vane was located. He described the differences between the two cases in terms of different effective diffusion coefficients, and concluded that stratification acts to inhibit the penetration of boundary effects.

The first comprehensive experimental study of spin-up was done by McLeod (1922) [50]. He made extensive velocity measurements of lycopodium particles floating on the free surface of a fluid in a cylindrical container which was spun-up and spun-down impulsively. McLeod obtained data for several angular velocities, using cylinders of various diameters and lengths, and noted a departure from his purely diffusive theory which "increases with angular velocity and with the size of the cylinder, but tends to vanish at very low velocities". He attributed the observed differences between theory and experimental results to the effects of the bottom boundary.

Pettersson (1931) [59] repeated the experiments of Ekman and made more careful and detailed observations of the induced flow in the interior regions of the fluid. He confirmed that Ekman's conclusion was correct, i.e., stratification inhibits the upward transfer of momentum. He also observed a secondary circulation, caused by the spin-up of the container, and realized that the upward transfer of momentum was due to this circulation rather than viscous diffusion of momentum. However, the picture of the secondary flow described by Pettersson was flawed: he claimed that the flow was thrown outward near the bottom of the container, flowed upward near the sidewall, turned horizontally inward into the core of the

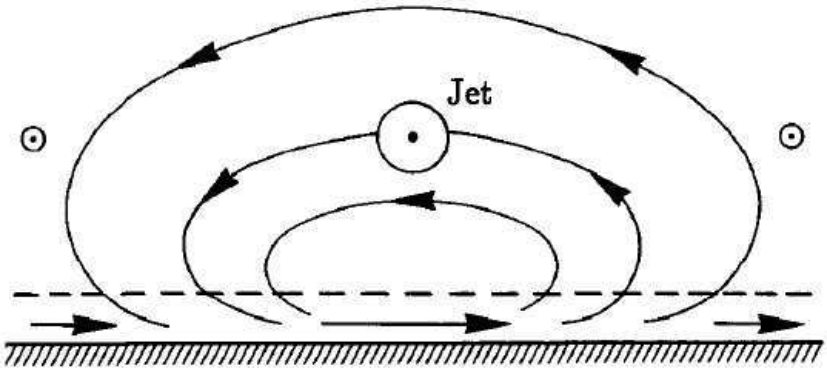

(a) Near the seafloor the current is reduced by friction so that the pressure gradient drives a cross-isobar flow. Lateral variations in the current cause variations of the flux in the Ekman layer, and force flow into, or out of, the interior. Coriolis force acting on this flow then reduces the initial current in the interior.

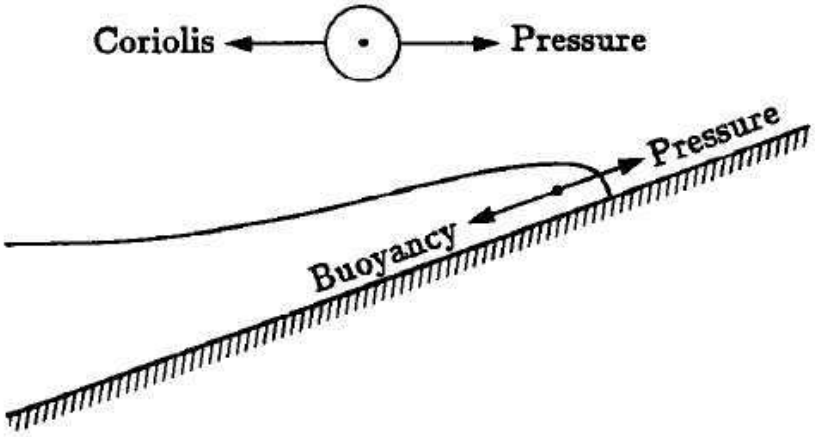

(b) Above a sloping bottom this dissipative process may be disrupted by buoyancy force. As the imbalance of pressure gradient and Coriolis force drives fluid cross-slope, the advection of density gives rise to a buoyancy force which opposes further motion. When the final balance is achieved, there is no further Ekman flux and the interior flow feels a nearly free-slip boundary condition at the seafloor.

Fig. 1.2: Differences in Ekman layer flux between flat and sloping bottom boundary, assuming a quasi-geostrophic flow (¶ 2.4) in the ocean interior. Reproduced from Garrett *et al.* (1993) [27].

flow, and then flowed into the bottom boundary layer via a narrow column at the center of the container. Although Petterson did not analyze his results quantitatively, he pointed out the correct qualitative nature of the process by which the rotation is transmitted to the main body of the fluid.

1.2 Homogeneous Fluid

The modern era of spin-up studies was initiated by the seminal paper of Greenspan & Howard (1963) [32], who considered small, impulsive changes in the rotation rate of arbitrary containers filled of homogeneous fluid in solid body rotation. They presented the complete solution of the linearized problem in case of small viscosity and exhibited the salient features of the flow.

The relative azimuthal flow generated by a rotation rate increase leads to the formation of Ekman layers on the horizontal boundaries. These boundary layers exhibit an outward mass flux and draw fluid from the interior region, which leads to an inward meridional [1] circulation, named *secondary circulation*. This circulation fills the interior, where the direct effects of viscosity are negligible, and uniformly spins-up the fluid to the new angular velocity of the container, as shown in Fig. 1.3. This is somewhat surprising since, if the fluid were

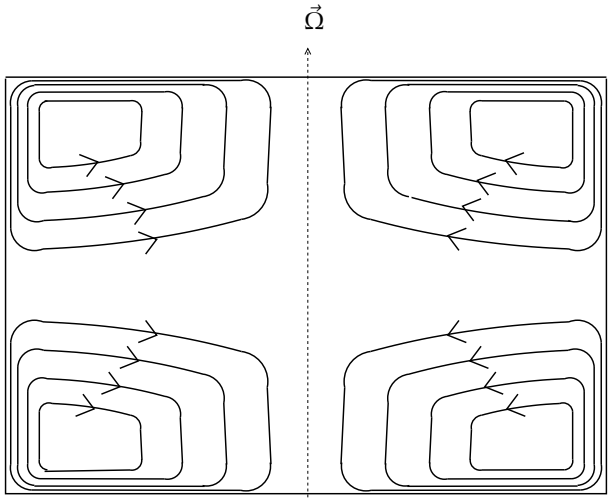

Fig. 1.3: Sketch of meridional streamlines for homogeneous spin-up. The flow direction is reversed for spin-down.

not rotating, then both dimensional analysis and physical reasoning would suggest that the interior fluid spins-up in the longer diffusive time scale.

[1] It is common when describing swirling flows to refer to the (r, z)-plane as the meridional plane.

Fig. 1.4 illustrates the frictionally-induced secondary circulation. Several drops of red dye are added to the fluid in solid body rotation at the surface near the center of the tank. After the change in the angular velocity of the tank the dye is quickly drawn from the interior region, and an outward motion at the bottom of the tank is produced (Fig. 1.4(a)). At the end of the transient spin-up process, the dyed fluid occupies a ring near the sidewall, while the dark area in the middle of the tank is remnants of dye where it was initially added (Fig. 1.4(b)).

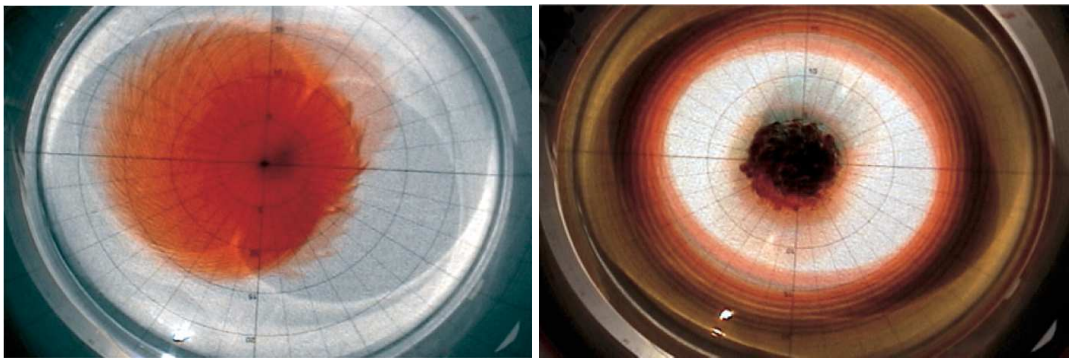

(a) (b)

Fig. 1.4: Spin-up: photographs from a demonstration of secondary circulation. Reproduced from McNoldy *et al.* (2003) [51]

The previous explanation works equally well if the discs are slightly spun-down rather than spun-up. It is necessary only to realize that the sense of the secondary circulation is reversed. However, the spin-down is not exactly symmetric with respect to the spin-up since the fluid particles near the sidewall may be affected by centrifugal instability according to the Rayleigh criterion (see, e.g., Saric (1994) [65]). Note that, since this criterion is based on the assumption that the fluid is inviscid and viscosity is presumably a stabilizing influence for such swirling flows, a velocity profile which is predicted to be unstable on the basis of the Rayleigh criterion may indeed be stable in practice. Moreover, this criterion was derived for steady flows, and Davis (1976) [12] argued that it would be reliable in unsteady problem such as spin-down process only if disturbances grow much faster than the basic flow varies in time.

1.3 Stratified Fluid

The stratified problem differs substantially from the homogeneous one in several ways. The presence of stratification introduces physical processes and mechanisms wholly lacking in the homogeneous system. The situation is sufficiently difficult that almost all theoretical investigations were carried out within the Boussinesq approximation (¶ 2.3), whose two common laboratory realizations are thermal-stratified and salt-stratified fluids.

Holton (1965) [34] considered the spin-up of a salt-stratified fluid and claimed that the Ekman layers took on basically the same form as in the homogeneous case. Diffusive boundary layers may also occur, but these play a passive role in the overall dynamics. The analysis of Holton was qualitatively correct, but had some inaccuracies in the treatment of the vertical sidewall layer (generally, the axis of rotation is assumed parallel to the local gravitational acceleration).

Pedlosky (1967) [56] reexamined the problem and showed that when the sidewall is insulated the vertical boundary layer is unable to transport the mass flux of the Ekman layer. This led Pedlosky to argue that, since there can be no inflow from the vertical boundary layer into the core (as there is in the homogeneous case), spin-up does not occur at all for configurations with a no-diffusion sidewall condition. He incorrectly predicted that the spin-up would then be achieved by diffusion of momentum.

The controversy was eventually resolved by Walin (1969) [74] and Sakuray (1969) [62], who showed that neither Holton nor Pedlosky was totally correct. Holton properly predicted the qualitative flow pattern, but missed the inability of the insulated sidewall layer to transport fluid. Pedlosky, although correctly analyzing the sidewall layer, falsely concluded that Ekman layers do not exist and the interior region spins-up by a strictly diffusive mechanism.

The effect of a stable stratification is indeed to restrict the recirculation of fluid from the Ekman layers to a localized region adjacent to the horizontal boundaries. This mechanism does not require transport into the sidewall layers, but the outward Ekman mass flux enters into the interior directly from the corner regions [2], as shown in Fig. 1.5.

1.4 Flow Instabilities

Although a large body of work has been reported on the incremental axisymmetric stratified spin-up, not much on the non-axisymmetric counterpart has appeared in the literature.

[2] regions where the sidewall intersects the horizontal boundaries

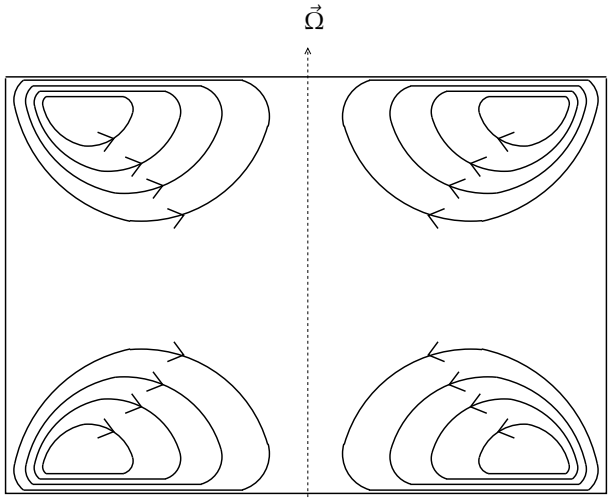

Fig. 1.5: Sketch of meridional streamlines for stratified spin-up. The flow direction is reversed for spin-down.

Experimental (e.g., Buzyna & Veronis (1971) [6]; Saunders & Beardsley (1975) [66]; Lee (1975) [43]) and numerical investigations (e.g., Barcilon *et al.* (1975) [1]; Hyun *et al.* (1982) [39]) of incremental spin-up in stably stratified fluid over flat bottom were performed since 1970s. The numerical models were axisymmetric in nature and cannot be extended to large times when appreciable non-axisymmetry is expected to develop in the flow field. Because of the numerical difficulties in constructing fully three-dimensional models, the objective was to examine the correct structure of the axisymmetric flow during the early phase of spin-up. On the other hand, also the experimental investigations, performed only in small geometries, were restricted in time. Although the possibility of a baroclinic instability existed, estimates of the growth rate indicated that they would not be seen on the spin-up time scale, i.e., the time in which the fluid adjusts to the new angular velocity of the boundaries, which is very short in such small scale systems (e.g., Saunders & Beardsley (1975)).

These studies generally found that, over the spin-up time, the azimuthal flow decays significantly faster than the theoretical predictions of Walin (1969) and Sakuray (1969). It was concluded that viscous-diffusion effects, arising from interior flow gradients due to the localized secondary circulation, may account for the discrepancies with the theory. The above findings brought into question the usual practice of separating the flow field into viscous Ekman layers and inviscid interior region when an investigation of stratified spin-up is attempted (Hyun (1983) [37]).

Pedlosky (1970) [57] investigated the motion of a continuously stratified fluid in a rotating annulus. The flow was driven by the differential rotation from relative rest of a lid on

the annulus in contact with the fluid. This work is the first pointing to baroclinic instability during spin-up in stably stratified fluid, although it pertains to surface forcing rather than an increase in the rotation rate of the whole system. Pedlosky (1970) established that the interior region is characterized by a quasi-steady azimuthal flow which presents a linear vertical shear. He found a minimum vertical shear of the interior azimuthal velocity above which the flow was unstable to non-axisymmetric disturbances.

Linden (1977) [45] performed a series of similar experiments. He confirmed that the axisymmetric basic flow is susceptible to instability due to the growth of non-axisymmetric disturbances. Baroclinic instability can develop through the release of potential energy stored in the horizontal density gradients which are set up in response to the vertical shear. In his experiments the shear was proportional to the Rossby number (¶ 2.2), and so the basic flow became unstable to non-axisymmetric disturbances for high enough Rossby number.

Greenspan (1980) [31] performed exploratory spin-up experiments from rest of a stably stratified fluid. Although the mechanism of the meridional circulation driven by the Ekman layers is still predominant, spin-up from rest is a more complex, inherently non-linear process. The fluid is not rotating initially and the meridional circulation cannot alter the angular velocity of the fluid in the interior region. Before spin-up can occur, all the fluid must be flushed out through the Ekman layers, where it acquires angular momentum before being returned in the interior. The ensuing motion in the interior is divided into rotating and non-rotating fluid separated by a propagating cylindrical shear layer. He showed that, unlike the strictly vertical front in the case of homogeneous fluid (Fig. 1.6(a)), in the stratified case the interface which separates rotating from non-rotating fluid is bowed (Fig. 1.6(b)). In

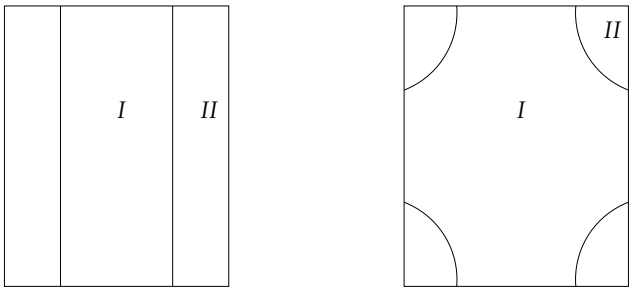

(a) homogeneous case (b) stratified case

Fig. 1.6: Spin-up from rest: sketch of early times showing non-rotating (*I*) and rotating (*II*) fluid regions separated by a propagating shear layer.

fact, since stratification causes the meridional flow to be concentrated in a region adjacent to the Ekman layers, the front moves faster near the horizontal boundaries rather than at mid-depth. Greenspan (1980) showed that the principal mechanism by which a stratified fluid spins-up from rest is the fluid instability, as evidenced by the production of strong penetrative vortices. However, he described only qualitatively the phenomenon, pointing out that it is not clear whether baroclinic instability or the instability of a shear layer were the dominant mechanism in the production of the vortices.

Spence *et al.* (1992) [70] considered the transient response of a linearly stratified rotating fluid to a constant stress applied impulsively to its horizontal upper boundary. They performed numerical and experimental investigations, but the study was restricted to flows which were stable since the objective was to gain an understanding of the transient behavior of the fluid within the spin-up time scale.

Flor *et al.* (2002) [24] and (2004) [23] studied the spin-up from rest of a stably stratified fluid. In the former work, they investigated the initial stage of spin-up, specifically the establishment and growth of the corner regions, which is always characterized by an axisymmetric circulation. They showed that the differences between spin-up from rest and incremental spin-up in stratified fluid appear in the shape of the zone influenced by the Ekman layer. In incremental spin-up, the region adjacent to the horizontal boundary is dome-shaped with maximal thickness at the center of the tank, as shown in Fig. 1.7(a). In fact, the secondary

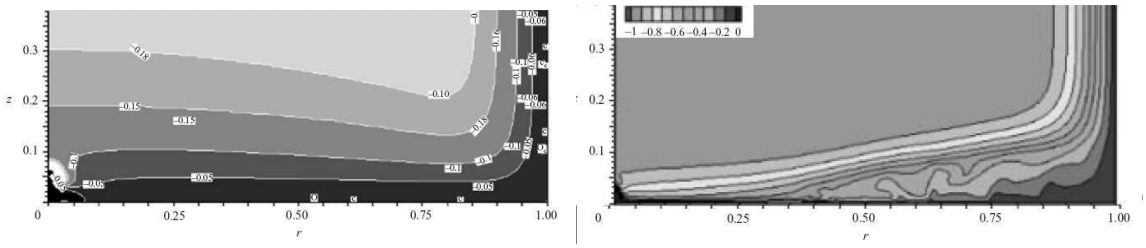

(a) incremental spin-up - $t/T \sim 9.5$ (b) spin-up from rest - $t/T \sim 8$

Fig. 1.7: Contour plots of angular velocity in lower right-hand side quadrant for strong stratification obtained by numerical simulations. Reproduced from Flor *et al.* (2002) [24].

circulation displaces fluid toward the center in the interior, and due to the initial vertical vorticity, which is stretched near the center of the tank, a dome-shaped domain appears. This is in contrast with spin-up from the rest, where there is a clear-cut connection between changes in density and angular velocity: the fluid accumulates in the corner regions (Fig.

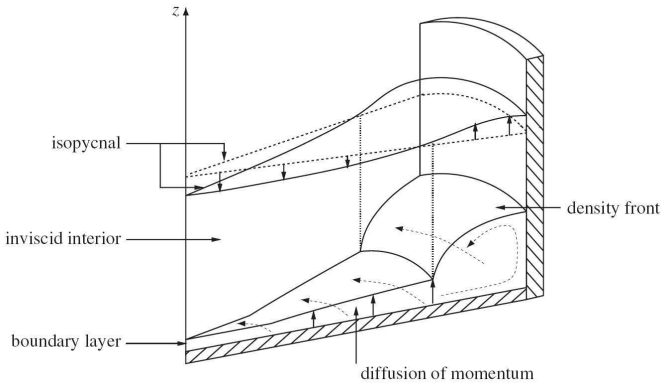

Fig. 1.8: Spin-up from rest: schematic diagram showing the important features of the initial flow, and the resulting effect on the background stable density field. An initial isopycnal surface, prior to the onset of disc motion, is shown as the broken-line planar segment, and the corresponding deformed isopycnal surface in the current state represented by the solid-line surface. Reproduced from Munro & Davies (2006) [54].

1.8) where both the surfaces of constant density and angular velocity are deflected upward, as shown in Fig. 1.7(b).

In the latter work, Flor *et al.* (2004) examined the stability of the initially axisymmetric configuration. At the end of the initial stage, the flow is characterized by a quiescent, vertically-stratified interior core suspended between rotating, homogenized corner regions. They observed that in case of low Burger number (¶ 2.3) the instability of the interior core is initiated by the development of a baroclinic instability at the interfaces between interior and corner regions. The subsequent evolution is interpreted in terms of combined influence of baroclinic and elliptical instabilities of the interior core. Note that Flor *et al.* (2002) pointed out that there were no reported observations of the instability in the interior region in the incremental spin-up problem.

Moulin & Flor (2004) [53] investigated the response of a rotating, linearly stratified fluid to local spin-up by a small rotating disc, with Rossby number around unity. The fluid ejected by the Ekman layer mixes with ambient fluid, and density fronts form at the edges of the disc (Fig. 1.9). They interpreted the continuous release of light fluid by the Ekman layer as an axisymmetric gravity current which spreads until it becomes unstable to non-axisymmetric disturbances, confirming that the baroclinic instability is the dominant mechanism.

Kanda (2004) [40] proposed a method to produce relatively isolated columnar baroclinic vortices in continuously stratified fluids making use of the instability during spin-up and spin-down. In most experimental runs, both from rest and incremental, the axisymmetric

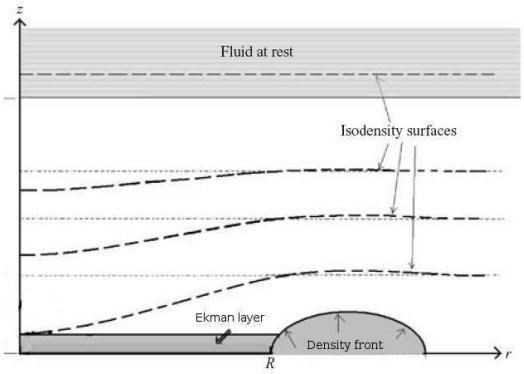

Fig. 1.9: Side-view schematic diagram of the flow near the disc of radius R after the onset of the disc rotation, showing the Ekman layer and the formation of the density front. Reproduced from Moulin & Flor (2004) [53].

flow became unstable and undular waves grew near the sidewall. The instability occurred for both spin-up and spin-down, and stable cases were found only for spin-up from rest. Although no systematic density measurements were conducted, Kanda (2004) supposed the presence of a front structure near the sidewall, with the long-wave instability caused by a similar mechanism to that of the frontal instability, which grows primarily by extracting the available potential energy of the mean flow via a baroclinic instability mechanism. However, some properties reminded him of the classical Eady-type baroclinic instability and he suggested that measurements with higher accuracy of the instability wave number were necessary.

Smirnov *et al.* (2005) [68] coped with non-axisymmetric flow during incremental spin-up in stably stratified fluid. The aim was to analyze the stability characteristics of a zonal flow over flat bottom in order to deepen the interaction of along-shelf currents with a single submarine canyon incised in a long continental slope. They investigated the nature of the long-term behavior of spin-up in a circular cylinder spotlighting on the formation of large-scale eddies. Smirnov *et al.* (2005) proposed a theoretical framework, termed *extended Eady's model*, in which the sheared sidewall layers are taken into account in order to explain the mechanism of eddy formation. They excluded that the instability of the Ekman layer, confined to a thin layer adjacent to the bottom of the container, could have a role in this phenomenon.

Munro & Davies (2006) [54] investigated the response of a rotating, linearly stratified fluid to a forcing induced by differentially rotating a horizontal disc on the bottom boundary. They observed the development of a front in the corner region, with formation of Kelvin-

Helmholtz type billows [3] at the interface. Munro & Davies (2006) reported entrainment and mixing between the two region, but no long-wave instability.

1.5 Motivations

We have illustrated briefly different impulsive spin-up processes whose flow development is affected by long-wave instability. Note that we are interested in the long-wave instability which develops, under appropriate conditions, exclusively in baroclinic fluid. The analysis of the other instabilities which may affect barotropic fluids, such as barotropic instability (see, e.g., Kuo (1949) [42]), goes beyond the scope of this thesis.

The impulsive spin-up processes may be distinguished into two classes: spin-up of the entire system (i.e., forcing induced by modifying the rotation rate of the container) and local spin-up (i.e., forcing induced by differentially rotating a lid in contact with the fluid) in presence of background rotation. The former can be incremental (Kanda (2004), Smirnov *et al.* (2005)) or from the rest (Greenspan (1980), Flor *et al.* (2002) and (2004)), while the latter may concern discs with radius both comparable (Pedlosky (1970), Linden (1977), Spence (1992), Munro & Davies (2006)) or smaller than the horizontal boundaries (Moulin & Flor (2004)). This sorting of previous non-axisymmetric spin-up investigations is summarized in Fig. 1.10.

Note that experiments concerning local spin-up from rest (e.g., Davies *et al.* (1995) [11]) were not considered since they involve the generation of a localized rotation in a non-rotating system. Consequently, these investigations are focussed mostly on turbulence, entrainment and mixing. Moreover, were excluded from our analysis the experiments in differentially heated annulus, initiated since 1950s by Fultz and Hide (e.g., Hide (1958) [33], Fultz *et al.* (1959) [26]) to understand the poleward heat transport from the equatorial latitudes by the atmospheric circulation. This type of experiments also copes with a secondary circulation, but this is due to thermal convection which arises in response to thermal forcing applied continuously to the lateral boundaries.

Different explanations were proposed to elucidate the development of large-scale disturbances. In spin-up from rest, the dynamics of the flow is governed by the corner regions, and the interface between rotating and non-rotating flow is affected by frontal instability. In case of incremental local spin-up, the same mechanism appears to be responsible for the

[3] The instability at the interface between two horizontal parallel streams of different velocities and densities is named *Kelvin-Helmholtz instability.*

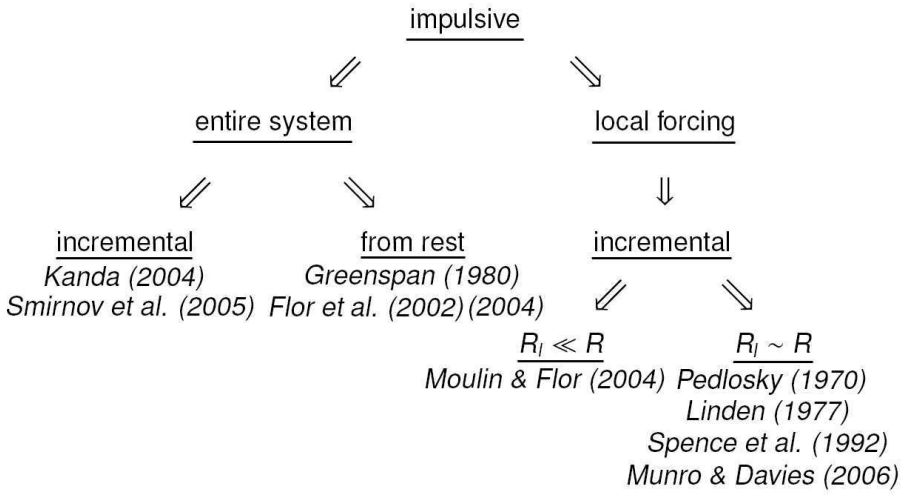

Fig. 1.10: Previous non-axisymmetric spin-up investigations. R and R_l are the radii of horizontal boundaries and lid, respectively.

instability when the forcing is induced by a small disc. However, in case of forcing induced by a disc of dimension comparable with the horizontal boundary, it seems that the corner regions do not play a relevant role in the instability development. In fact, Munro & Davies (2006) did not report any long-wave instability in their experiments, although they observed the evolution of a front in the corner regions. Kanda (2004) supposed that the primary cause of instability is ageostrophy due to large isopycnal deformation near the sidewall, but he did not distinguish between incremental spin-up and spin-up from rest. Moreover, stable cases were found only in spin-up from rest, but these should be the most unstable as long as the instability is attributed to the corner regions. On other hand, Smirnov *et al.* (2005) did not examine the corner regions, but proposed that the vertical sidewall should play a role in the growth of the long-wave instability in incremental spin-up.

Consequently, the mechanism of long-wave instability in incremental spin-up has not been made clear. In order to deepen the source of the instability we performed a series of incremental spin-up and spin-down experiments. Both axisymmetric and non-axisymmetric regimes in stably stratified fluid over flat bottom were considered. The experimental facility used is the large cylindrical rotating tank (¶ 4.2) of the Coriolis-LEGI laboratory, characterized by an aspect ratio $\delta \equiv H/L \sim O(10^{-1})$ relevant in the geophysical context. Moreover, we set a very small Ekman number ($E \sim O(10^{-5})$): it will be shown (¶ 4.2) that this provides a better separation between the time scales over which the spin-up process takes place (¶ 3.1). Consequently, the experimental results may be properly compared with the analytical theory

of Walin (1969) (¶ 3.2), and the non-axisymmetric effects investigated over the outstanding spin-up time scale.

1.6 Plan

This thesis includes eight chapters, organized as follow

- In **chapter** 2, the dynamical equations, fundamental theorems and conventions used through this thesis are discussed.

- In **chapter** 3, the theory of spin-up process is presented, focussing on axisymmetric containers. The Ekman layer is analyzed carefully, and the differences between spin-up in homogeneous and stratified fluid are retraced. The chapter ends with a discussion which summarizes the previous experimental and numerical works in axisymmetric regime.

- In **chapter** 4, the experimental facility is presented, and the experimental runs described and motivated. The main features of measurement techniques and data analysis are illustrated as well.

- In **chapter** 5, the effect of the physical parameters which influence the flow evolution is analyzed. This should be regarded as a preliminary study in order to restrict the investigations in the subsequent chapters.

- In **chapter** 6, the axisymmetric spin-up behavior is analyzed in detail. A direct comparison with the analytical theory is performed and an attempt to improve it presented and discussed.

- In **chapter** 7, the non axisymmetric counterpart is deeply investigated. A quantitative comparison with the Eady's model (¶ 2.5.1) is performed and a visualization of the instability pattern provided.

- In **chapter** 8, the general conclusions are outlined and some perspectives suggested.

Chapter 2

Fundamentals

2.1 Vorticity Basics

In classical mechanics, the conservation of angular momentum is often invoked in the analysis of rigid motions which involve rotation. Analogous conservation laws apply to rotational flows, keeping into account that in a continuous medium, such as the atmosphere or oceans, the definition of rotation is trickier than for a solid object.

The *vorticity* is a vector field defined as the curl of the velocity field, i.e., $\vec{\omega} \equiv \vec{\nabla} \times \vec{u}$, and it gives a microscopic measure of the rotation at any point in the fluid. The vorticity of the fluid as observed from the absolute frame of reference is called *absolute vorticity*, $\vec{\omega}_a$, defined as

$$\vec{\omega}_a \equiv \vec{\nabla} \times \vec{u}_a = \vec{\nabla} \times \left(\vec{u} + \vec{\Omega} \times \vec{r} \right) = \vec{\omega} + 2\vec{\Omega}$$

being $\vec{u}_a$ the absolute velocity. Thus, the absolute vorticity is the sum of *planetary vorticity* $2\vec{\Omega}$ and *relative vorticity* $\vec{\omega}$, i.e., the curl of the velocity $\vec{u}$ observed from the frame of reference rotating with uniform angular velocity $\vec{\Omega}$.

A *vortex line* is a line in the fluid which at each point is parallel to the vorticity vector. A *vortex tube* is formed by the surface which consists of the vortex lines passing through a closed curve C. The *vortex tube strength*, Γ, is defined as the flux of vorticity across any surface with area A whose bonding curve is C and unit vector normal at each point is $\hat{n}$, i.e.,

$$\Gamma \equiv \iint_A \vec{\omega} \cdot \hat{n} \, \mathrm{d}A$$

The flux of absolute vorticity, Γ_a, through a surface A is related to the relative vorticity flux, Γ, by

$$\Gamma_a \equiv \iint_A \vec{\omega}_a \cdot \hat{n} \, \mathrm{d}A = \Gamma + 2\Omega A_n$$

where A_n is the area of A projected on a surface perpendicular to $\vec{\Omega}$. The difference between absolute and relative vorticity flux is thus proportional to the number of planetary vortex lines enclosed by the contour C bounding A.

The *circulation* is a scalar integral quantity which gives a macroscopic measure of the rotation for a finite area of the fluid. It is defined as the line integral of the velocity field around a curve C, i.e.,

$$\Gamma \equiv \oint_C \vec{u} \cdot \mathrm{d}\vec{r}$$

The *Kelvin's theorem* states that the absolute circulation is conserved following the motion, i.e., $\mathrm{d}\Gamma_a/\mathrm{d}t = 0$, if the fluid is barotropic on a material curve C and the viscous force vanishes on it. Since Γ_a is the sum of the planetary and relative vortex tube strengths, Kelvin's theorem provides the mechanism of vorticity induction, i.e., a transfer between relative and planetary vorticity as to conserve the absolute vortex tube strength. As C moves and deforms with the fluid, it always forms the boundary of a tube of fixed absolute vortex strength. If the cross-section of a tube decreases, the intensity of the tube strength, i.e., the absolute vorticity in the tube, must increase in inverse proportion to the tube cross-sectional area.

The presence of viscous effects causes a diffusion of vorticity away from their original fluid elements, and consequently changes the circulation. In baroclinic fluids, the isobaric and isopycnal surfaces are not coincident. The net pressure force hence does not pass through the center of mass of the fluid element, and the resulting torque can produce new vortex lines.

The Vorticity Equation

The vorticity equation concerns the rate of change of the vorticity following a fluid element. In a rotating frame of reference, omitting viscous and baroclinic effects, the equation is

$$\frac{\mathrm{d}\vec{\omega}}{\mathrm{d}t} = (\vec{\omega} + 2\vec{\Omega}) \cdot \vec{\nabla}\vec{u} \tag{2.1}$$

The terms on the right-hand side of Eq.n (2.1) describe two mechanisms called *vortex tube stretching/squeezing* and *vortex line tilting*. The vortex tube stretching/squeezing alters the vorticity parallel to a vortex line by convergence/divergence of the velocity components in the plane perpendicular to the vortex line. This reflects the fact that in a nearly incompressible fluid a decrease of the cross section of a column can be accomplished only by extension along its length so as to preserve volume. A vertically stretching (squeezing) fluid column tends to acquire positive (negative) vertical vorticity. The vortex line tilting alters the vorticity

perpendicular to a vortex line by the shear of the velocity components along the vortex line. The vorticity perpendicular to the vortex line is the component of the vorticity vector tilted by the velocity shear along the vortex line. Note that merely a stretching or tilting of vertical fluid lines is required for $2\vec{\Omega}\cdot\vec{\nabla}\vec{u}$ to operate, in contrast to $\vec{\omega}\cdot\vec{\nabla}\vec{u}$ where a stretching or tilting of vortex lines is needed. This because vertical fluid lines contain planetary vorticity $2\vec{\Omega}$. If $\vec{\omega}$ is initially zero, the tilting and stretching/squeezing of the vortex lines in a fluid in presence of planetary vorticity will introduce, if allowed to proceed, relative vorticity (Kundu (1990) [41]).

Potential Vorticity

Ertel (1942) [17] derived a theorem which provides a constraint on the vorticity. For an inviscid fluid it shows

$$\frac{\mathrm{d}}{\mathrm{d}t}\left(\frac{\vec{\omega}_a}{\rho}\cdot\vec{\nabla}\lambda\right) = \frac{\vec{\omega}_a}{\rho}\cdot\vec{\nabla}\left(\frac{\mathrm{d}\lambda}{\mathrm{d}t}\right) + \vec{\nabla}\lambda\cdot\left(\frac{\vec{\nabla}\rho\times\vec{\nabla}p}{\rho^3}\right) \tag{2.2}$$

where λ is a scalar fluid property. Thus, Eq.n (2.2) states that if: 1) λ is a conserved quantity for each fluid element; 2) the fluid is barotropic or λ can be considered a function only of p and ρ, then the *potential vorticity*

$$\Pi \equiv \frac{(\vec{\omega}+2\vec{\Omega})}{\rho}\cdot\vec{\nabla}\lambda \tag{2.3}$$

is conserved by each fluid element, i.e., $\mathrm{d}\Pi/\mathrm{d}t = 0$. If Π is conserved following a fluid element, when the distance between two adjacent λ-surfaces increases, $\vec{\nabla}\lambda$ must decrease, and the component of the vector $\vec{\omega}_a/\rho$ parallel to $\vec{\nabla}\lambda$ must increase proportionally to keep Π constant. If ρ does not vary very much, then $\vec{\omega}_a$ increases and it may be considered that there is a reservoir of vorticity associated with the packing together of λ-surfaces which can be released as they are stretched by the mechanism of vortex-tube stretching (Pedlosky (1987) [58]). Note that the conservation of potential vorticity is simply a consequence of the mass and angular momentum conservation.

2.2 Homogeneous Fluid Dynamics

We consider only incompressible flows, i.e., flows in which the pressure variations do not produce any significant density variation. One of the requirements for which this is a good approximation is that the vertical scale of motion H is small compared with a *scale height*

defined as a median value of $\rho/|\mathrm{d}\rho/\mathrm{d}z|$ (Batchelor (1967) [3]). This condition is satisfied in the ocean since the scale height is about 40 times the depth (Gill (1982) [29]).

Equations of Motion

The equations governing the motion of a homogeneous incompressible fluid state the conservation of momentum and mass. In a frame of reference rotating with uniform angular velocity $\vec{\Omega} = \Omega\hat{k}$

$$\frac{\partial \vec{u}}{\partial t} + \vec{u}\cdot\vec{\nabla}\vec{u} + 2\Omega\hat{k}\times\vec{u} = -\frac{1}{\rho}\vec{\nabla}\tilde{p} + \nu\nabla^2\vec{u} \tag{2.4a}$$

$$\vec{\nabla}\cdot\vec{u} = 0 \tag{2.4b}$$

Note that the f-plane approximation has been considered, and the sphericity effects will be neglected. The variable $\tilde{p}$ is the *modified pressure* [1], defined as

$$\tilde{p} = p - p_0 - \rho\vec{g}\cdot\vec{r} - \frac{\rho}{2}\left(\vec{\Omega}\times\vec{r}\right)\cdot\left(\vec{\Omega}\times\vec{r}\right) \tag{2.5}$$

where p_0 is a constant. It arises wholly from the effect of the relative motion of the fluid since in solid body rotation the forces due to gravity and centrifugal effects acting on the fluid are balanced by a pressure equal to $\rho\vec{g}\cdot\vec{r}$ and $(\rho/2)\left(\vec{\Omega}\times\vec{r}\right)\cdot\left(\vec{\Omega}\times\vec{r}\right)$. Note that Eq.n (2.5) is valid strictly in homogeneous fluid for which the gravitational force may be represented as the gradient of a scalar quantity.

These equations should be posed on some domain, and supplied with suitable initial and boundary conditions. The mathematical difficulties presented by the Eq.n (2.4a) are so severe that most of the existing solutions are applicable only to circumstances in which it reduces to linear form.

Geostrophic Approximation

Let us suppose that the Coriolis force is large compared with both advection and viscous terms

$$|\vec{u}\cdot\vec{\nabla}\vec{u}| \ll |\vec{\Omega}\times\vec{u}| \tag{2.6}$$

$$|\nu\nabla^2\vec{u}| \ll |\vec{\Omega}\times\vec{u}| \tag{2.7}$$

[1] a term first used by Batchelor (1967)

Introducing L and U, respectively length and velocity scales characteristic of the motion, the conditions (2.6) and (2.7) become

$$\frac{U}{\Omega L} \ll 1 \tag{2.8}$$

$$\frac{\nu}{\Omega L^2} \ll 1 \tag{2.9}$$

The non-dimensional quantities $U/\Omega L$ and $\nu/\Omega L^2$, known as the *Rossby number*, ϵ, and the *Ekman number*, E, indicates the relative importance of, respectively, advective term to Coriolis force and viscous to Coriolis forces.

Restricting attention to steady flow, under the conditions (2.8) and (2.9) Eq.n (2.4a) may be approximate

$$2\Omega\hat{k} \times \vec{u} = -\frac{1}{\rho}\vec{\nabla}\tilde{p} \tag{2.10}$$

Flows in which the balance between Coriolis and pressure gradient forces pertains are named *geostrophic flows*. The geostrophic balance is a diagnostic expression appropriate for quasi-steady, large-scale motions in the atmosphere or oceans. Therefore, L and U are usually *horizontal* length and velocity scales characteristic of the motion. Note that the velocity

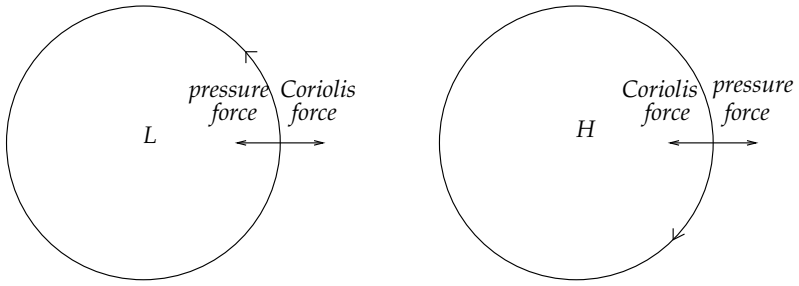

Fig. 2.1: Geostrophic flow around low and high pressure centers

in a geostrophic flow is along the isobars since Eq.n (2.10) implies $\vec{u} \cdot \vec{\nabla}\tilde{p} = 0$. Fig. 2.1 shows a sketch of the geostrophic flow around low and high pressure centers in the northern hemisphere, where the Coriolis force acts to the right of the horizontal velocity vector. This requires the flow to be anticlockwise (viewed from above) around a low pressure region and clockwise around a high pressure region.

Note that in this case the pressure involved is the modified pressure, which includes the centrifugal effects. For this reason some authors (e.g., Holton (1992) [35]) refer to such flows as *gradient flows*, limiting the term geostrophic to straight flows.

An important property of geostrophic flows is discovered by taking the curl of Eq.n (2.10)

and using the continuity equation (2.4b)

$$\frac{\partial \vec{u}}{\partial z} = 0 \tag{2.11}$$

All the three components of the relative velocity are independent of the direction parallel to the rotation axis. This constraint is known as the *Taylor-Proudman theorem*, and it follows that a material line initially parallel to the rotation axis must always remains so as it moves around like a rigid column. Such vertical rigidity is a fundamental property of rotating homogeneous fluids.

2.3 Stratified Fluid Dynamics

The term *stratified fluid* is applied to a flow primarily in the horizontal direction which is affected by a vertical variation of the density. The background rotation leads homogeneous fluids to a strong tendency to behave in a columnar fashion, characterized by a vertical rigidity. By contrast, a stratified fluid under gravity arranges itself so that higher underlie lower densities (*stable stratification*). The vertical layering introduces an obvious gradient of properties in the vertical direction, which affects also the velocity field. Hence, the vertical rigidity induced by the effects of rotation will be attenuated by the presence of the stratification.

Static Stability

Let us first consider a fluid in static equilibrium. Such lack of motion requires the absence of lateral forces and, consequently, horizontal homogeneity: stratification is then purely vertical. If a fluid particle is displaced vertically by a small distance δz from z_A to $z_B > z_A$, without disturbing its environment in hydrostatic balance such as $\mathrm{d}p_s/\mathrm{d}z = -\rho_s g$, being $p_s(z)$ and $\rho_s(z)$ pressure and density of the environment, the vertical acceleration of the particle is

$$\frac{\mathrm{d}^2}{\mathrm{d}t^2}(\delta z) = -g - \frac{1}{\rho_A}\frac{\partial p_A}{\partial z} \tag{2.12}$$

being $p_A \equiv p_s(z_A)$ and $\rho_A \equiv \rho_s(z_A)$ pressure and density of the particle. Let us assume that the pressure of the particle instantaneously adjusts to the environmental pressure during the displacement, so as p_A is replaced by $p_B \equiv p_s(z_B)$ in Eq.n (2.12). Thus, using the hydrostatic relationship of the environment, the pressure can be eliminated in Eq.n (2.12),

$$\frac{\mathrm{d}^2}{\mathrm{d}t^2}(\delta z) = g\left(\frac{\rho_B - \rho_A}{\rho_A}\right) \tag{2.13}$$

Since $\rho_B - \rho_A \simeq (\mathrm{d}\rho_s/\mathrm{d}z)\,\delta z$, Eq.n (2.13) becomes

$$\frac{\mathrm{d}^2}{\mathrm{d}t^2}(\delta z) = -N^2 \delta z \tag{2.14}$$

showing an oscillatory character, being

$$N^2 \equiv -\frac{g}{\rho_A}\frac{\mathrm{d}\rho_s}{\mathrm{d}z} \tag{2.15}$$

In stably stratified fluids, physically Eq.n (2.14) means that, when displaced upward, the particle is heavier than its surroundings, feels a downward recalling force, falls down, and, in the process, acquires a vertical velocity. Upon reaching its original level the particle's inertia causes it to go farther downward and to become surrounded by heavier fluid. The particle, now buoyant, is recalled upward, and oscillations persist about the equilibrium level. The quantity N, defined by the square root of Eq.n (2.15), provides the frequency of the oscillation and is termed *buoyancy frequency*.

Equations of Motion

The equations governing the motion of a stratified incompressible fluid may be written within the Boussinesq approximation

$$\rho_0\left(\frac{\partial \vec{u}}{\partial t} + \vec{u}\cdot\vec{\nabla}\vec{u} + 2\Omega\hat{k}\times\vec{u}\right) = -\vec{\nabla}\tilde{p} - \tilde{\rho}g\hat{k} + \rho_0\nu\nabla^2\vec{u} \tag{2.16a}$$

$$\vec{\nabla}\cdot\vec{u} = 0 \tag{2.16b}$$

$$\frac{\mathrm{d}\tilde{\rho}}{\mathrm{d}t} + w\frac{\partial\rho_s}{\partial z} = \kappa\nabla^2\tilde{\rho} \tag{2.16c}$$

where Eq.n (2.16c) is the density diffusion equation, and the choice of the salt diffusivity κ indicates that we focuss on salt-stratified fluids. In Eq.n (2.16a) the centrifugal term was incorporated in the pressure gradient and the gravitational acceleration $-g\hat{k}$ assumed antiparallel to the rotation vector $\Omega\hat{k}$. Although this last assumption is usually not valid in geophysical application, essentially the same set of equations is obtained without this approximation, providing the depth of the fluid much smaller than the horizontal scale of motion (*shallow water approximation*), which is often the case in geophysical situations (Walin (1969) [74]).

Density and pressure field were split as

$$\rho = \rho_0 + \rho_s(z) + \tilde{\rho}(\vec{r},t)$$

$$p = p_0 + p_s(z) + \tilde{p}(\vec{r},t)$$

assuming that the flow is superposed on a *background state* of relative rest defined by

$$\vec{\nabla} p_s = -(\rho_0 + \rho_s) g \hat{k}$$

The basic stratification, $\rho_s = \rho_s(z)$, implies that the isopycnal surfaces are essentially parallel to the horizontal for solid body rotation. The density perturbation, $\tilde{\rho} = \tilde{\rho}(\vec{r}, t)$, of the basic stratification occurs as a result of the relative motion, and ρ_0 is a reference density such that the density anomaly is small, i.e., $|\rho - \rho_0| \ll \rho_0$.

The Boussinesq approximation consists of taking the density constant when computing the rates of change of momentum from accelerations, but including density anomaly when they give rise to buoyancy term.

Thermal Wind

Assuming a flow in geostrophic and hydrostatic balance,

$$2\Omega \rho_0 \hat{k} \times \vec{u} = -\vec{\nabla} \tilde{p} - \tilde{\rho} g \hat{k} \tag{2.17}$$

let us consider a situation in which the isopycnal surfaces slope downward with x, the surfaces at lower levels representing higher density (Fig. 2.2). This implies that the horizontal density

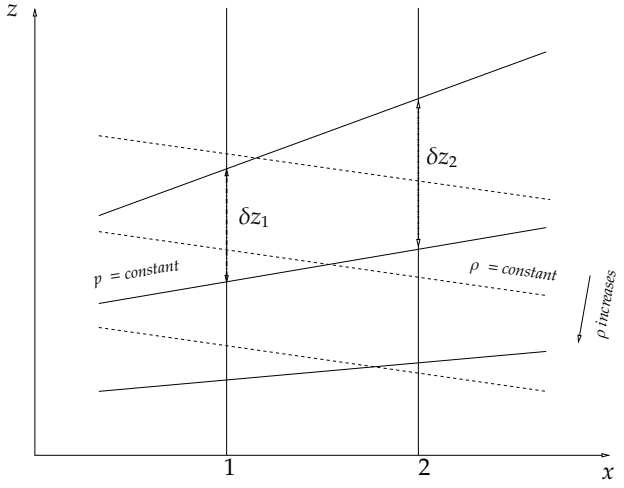

Fig. 2.2: Isobars are indicated by solid lines and isopycnal by dashed lines.

gradient is negative, so that the density is larger along section 1 than section 2. Hydrostatic equilibrium requires that the weights of columns δz_1 and δz_2 are equal, so that the separation across two isobars increases with x, i.e., $\delta z_2 > \delta z_1$. Thereby, the isobaric surfaces must slope

upward with x, resulting in a positive horizontal pressure gradient.

A manipulation of Eq.n (2.17) provides

$$\frac{\partial \vec{u}}{\partial z} = -\frac{g}{2\Omega\rho_0}\hat{k} \times \vec{\nabla}\tilde{\rho} \tag{2.18}$$

Thus, in presence of horizontal density gradient, the geostrophic velocity develops a vertical shear. The meteorologists call Eq.n (2.18) the *thermal wind* equation since in the atmosphere it gives the vertical variation of wind from measurements of horizontal temperature gradients. When isobaric and isopycnal surfaces do not coincide, as in this case, the flow is named to be in *baroclinic* state.

Rotation and Stratification

Let us consider a quasi-steady *stratified non-rotating* fluid, in absence of both viscous and diffusive processes. The governing equations (2.16) assume the form

$$\rho_0 \, \vec{u} \cdot \vec{\nabla}\vec{u} = -\vec{\nabla}\tilde{p} - \tilde{\rho} g \hat{k} \tag{2.19a}$$

$$\vec{u} \cdot \vec{\nabla}\tilde{\rho} + w\frac{\partial \rho_s}{\partial z} = 0 \tag{2.19b}$$

A flow, with horizontal length scales L and velocity scale U, produces a perturbation $\tilde{\rho}$ of the basic stratification ρ_s, whose relation is expressed by Eq.n (2.19b),

$$\tilde{\rho} \sim \frac{\rho_0}{g}\frac{WL}{U}N^2 \tag{2.20}$$

Using Eq.n (2.19a), the hydrostatic balance provides

$$\tilde{p} \sim \rho_0 \frac{WLHN^2}{U} \tag{2.21}$$

and the horizontal balance of forces indicates

$$\frac{W/H}{U/L} \sim \frac{U^2}{N^2H^2} \equiv Fr^2 \tag{2.22}$$

where Fr is called *internal Froude number*. The analogy with the Rossby number, $\epsilon \equiv U/\Omega L$, is immediate. Both Froude and Rossby numbers are ratios of the horizontal velocity scale to a product of frequency and length scale. When Fr is small, stratification effects are important; the stronger the stratification, the weaker the vertical velocity and vertical displacements. In fact, vertical motions in a stably stratified fluid tend to carry heavier fluid upward and lighter fluid downward, and are thus inhibited.

In a *homogeneous rotating* fluid in geostrophic approximation the horizontal divergence

is zero, and consequently the vertical convergence. Actually, the flow cannot be purely geostrophic, and the advective term, whose relative importance is measured by ϵ, yields a correction to the geostrophic velocities of the same relative importance, i.e.,

$$\frac{W/H}{U/L} \sim \epsilon$$

In a *stratified rotating* fluid in geostrophic approximation the analysis remains unchanged, except that the advective term in Eq.n (2.19a) is replaced by the Coriolis force. An analogous procedure provides

$$\frac{W/H}{U/L} \sim \frac{U^2}{N^2H^2}\frac{\Omega L}{U} = \frac{Fr^2}{\epsilon}$$

As a result, the influence of a strong rotation ($\epsilon \lesssim 1$) is to increase the scale of the vertical velocity. However, since a vertical divergence cannot exist without horizontal convergence ($W/H \lesssim U/L$), then $Fr^2 \lesssim \epsilon$ must hold, i.e,

$$\frac{U}{NH} \lesssim \frac{NH}{\Omega L} \tag{2.23}$$

This sets an upper bound for the magnitude of the flow field in a fluid under given rotation (Ω) and of given stratification (N) in a domain of given dimensions (L, H). The inequality in Eq.n (2.23) brings to the *Burger number*, *Bu*

$$Bu \equiv \frac{N^2H^2}{\Omega^2L^2} = \frac{\epsilon^2}{Fr^2} \tag{2.24}$$

It measures the relative importance of stratification and rotation. A value of *Bu* around 1 indicates that stratification and rotation have comparable influences; when *Bu* is small a rotating flow is modified by stratification, and when *Bu* is large is the other way round. The minimum horizontal length scale on which rotational effects are very significant, $L_d \equiv NH/\Omega$, is called the *Rossby radius of deformation*.

In circumstances for which only a single length scale is involved ($L \equiv H$), the relative importance between stratification and rotation is measured by the *stratification parameter S*

$$S \equiv \frac{N^2}{\Omega^2}$$

2.4 Quasi-Geostrophic Dynamics

The geostrophic approximation is very useful: once the pressure field is known, the horizontal velocities, their vertical shear, and the vertical component of vorticity are immediately determined. However, the geostrophic balance is a diagnostic relation which does not

allow to calculate the pressure field or predict its evolution with time. The geostrophic approximation alone, in fact, does not contain enough information to complete the dynamical determination of the motion. Mathematically, the fact that the geostrophic approximation leads to a zero horizontal divergence in the continuity equation means that these three equations do not give three independent items of information. In this sense, the geostrophic equations are degenerate and cannot yield the ultimate steady solution by themselves. Consequently, any pressure field can yield a consistent geostrophic velocity, but, at the level of the geostrophic approximation, it is not possible to distinguish which of the proposed pressure fields is the correct one. Moreover, a zero horizontal divergence implies the absence of any vertical velocity over flat boundaries. This means no lifting and lowering of isopycnal surfaces and thus no pressure disturbances and no motion. The resolution of this constraint requires the consideration of small departures of the flow from exact geostrophic balance.

Charney & Stern (1962) [8] obtained the governing equation in shallow water approximation for a quasi-geostrophic motion in a continuously stratified fluid. For an inviscid flow on a f-plane

$$\left[\frac{\partial}{\partial t}+\frac{\partial \psi}{\partial x}\frac{\partial}{\partial y}-\frac{\partial \psi}{\partial y}\frac{\partial}{\partial x}\right]\left[\nabla_H{}^2\psi+\frac{\partial}{\partial z}\left(\frac{4\Omega^2}{N^2}\frac{\partial \psi}{\partial z}\right)\right]=0 \tag{2.25}$$

where $\psi \equiv \tilde{p}/2\Omega\rho_0$ is the geostrophic stream function such as

$$\begin{aligned} u &= -\frac{\partial \psi}{\partial y} \\ v &= \frac{\partial \psi}{\partial x} \end{aligned}$$

The quasi-geostrophic potential vorticity equation (2.25) states the conservation of the potential vorticity (Eq.n (2.3)) in which the geostrophic and hydrostatic approximations are used to evaluate horizontal velocities and density in terms of pressure. The departure from strict geostrophy determines the evolution of the flow by involving either the advective term, of the order of the Rossby number, and/or the viscous force, of the order of the Ekman number.

2.5 Baroclinic Instability

Baroclinic instability refers to a class of wavelike motions which can arise on large scale flows with vertical shear in which Coriolis and buoyancy forces are important. Charney (1947) [9] and Eady (1949) [14] provided the theoretical foundation of baroclinic instability in the Earth's atmosphere, which became a dominant topic of meteorological research throughout the 1950s and 1960s. Oceanographers became interested in baroclinic instability in 1970s,

following the discovery of energetic mesoscale eddies in the western North Atlantic (e.g., Gill *et al.* (1974) [28]).

The Basic Mechanism

Let us consider an eastward geostrophic current maintained by sloping isopycnal surfaces, as sketched in Fig. 2.3. This is an equilibrium situation only because the Coriolis force is balanced by the horizontal pressure gradient (cf., Fig. 2.2). The horizontal density gradients imply the presence of available potential energy, which may be transferred to small perturbations superimposed to the basic flow by a process called baroclinic instability. Note that the perturbations do not grow by extracting energy from the vertical shear field since the vertical velocity is too small in quasi-geostrophic flows.

Let us consider the displacement of a fluid element from position A in Fig. 2.3 to a new position B. Let the displacement of the fluid element along y and z direction be δy and δz,

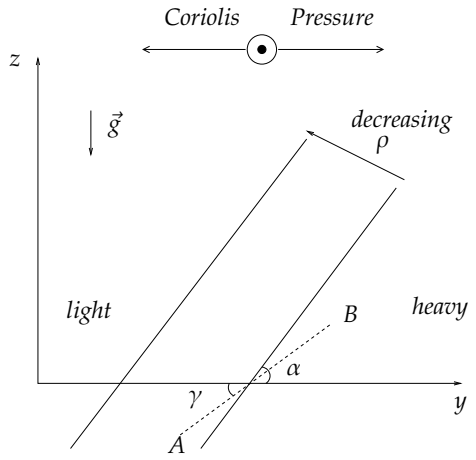

Fig. 2.3: The slope of the isopycnal surfaces with respect to the horizontal.

respectively. Since the fluid is incompressible, the element A keeps is density when moves to the position B and adjusts to the environmental pressure. The force undergone by the fluid element along the displacement direction is

$$F = \left(\frac{\rho_B - \rho_A}{\rho_A}\right) g \sin\gamma \tag{2.27}$$

where γ is the angle of the displacement ($\tan\gamma = \delta z/\delta y$). Since

$$\begin{aligned}\rho_B - \rho_A &\simeq \frac{\partial\rho}{\partial z}\delta z + \frac{\partial\rho}{\partial y}\delta y \\ &= \frac{\partial\rho}{\partial z}\left[\delta z + \frac{(\partial\rho/\partial y)}{(\partial\rho/\partial z)}\delta y\right]\end{aligned}$$

Eq.n (2.27) may be written as

$$F = -N^2 \sin\gamma\left[\delta z - \left(\frac{\partial z}{\partial y}\right)_\rho \delta y\right] \tag{2.28}$$

As long as $N^2 > 0$, the displacements which yield a *restoring* force, i.e., $F < 0$, are characterized by a trajectory such as $\tan\gamma > (\partial z/\partial y)_\rho$. Otherwise, if fluid elements are displaced within the wedge defined by the horizontal and the isopycnal surfaces, i.e., $\tan\gamma < (\partial z/\partial y)_\rho$, then F will be positive and the buoyancy force will accelerate the fluid element further from its initial position. This is the essential mechanism of baroclinic instability, and depends crucially on the slope of the isopycnal surfaces. The releasing of the available potential energy implies that light fluid rises and heavy fluid sinks: baroclinic instability may be seen as a form of convection (*sloping convection*).

The instability condition requires

$$Bu \equiv \frac{L_d^2}{L^2} \leq O(1) \tag{2.29}$$

Length scales of the perturbations favored for baroclinic instability therefore exceed the Rossby radius of deformation (Pedlosky (1987) [58]).

2.5.1 Eady's Model

Let us consider a basic initial state $\psi = \Psi(y, z)$ characterized by the zonal velocity $U_i = -\partial\Psi/\partial y$. In the model proposed by Eady (1949) [14] the velocity U_i is independent of y (e.g., $U_i = U\, z/H$) and the horizontal density gradient is constant. Furthermore, the inviscid flow is confined in the vertical direction by two rigid horizontal boundaries at $z = 0, H$. Let us now assume that the total flow is composed of the basic state Ψ plus perturbations ϕ

$$\psi(x, y, z, t) = \Psi(y, z) + \phi(x, y, z, t) \tag{2.30}$$

If Eq.n (2.30) is substituted in Eq.n (2.25), a nonlinear problem for ϕ results. Let us assume that, at least initially, the amplitude of the disturbance is sufficiently small, i.e., $\phi \ll 1$. This

leads to the linear stability problem,

$$\left(\frac{\partial}{\partial t} + U_i\frac{\partial}{\partial x}\right)\left(\frac{\partial^2\phi}{\partial x^2} + \frac{\partial^2\phi}{\partial y^2} + \frac{4\Omega^2}{N^2}\frac{\partial^2\phi}{\partial z^2}\right) = 0 \tag{2.31a}$$

$$\left(\frac{\partial}{\partial t} + U_i\frac{\partial}{\partial x}\right)\frac{\partial\phi}{\partial z} - \frac{\partial\phi}{\partial x} = 0 \text{ at } z = 0, H \tag{2.31b}$$

The essential physical question is now to determine if, given a particular initial state, the perturbation field ϕ placed on the flow tends to grow or decay.

The existence of fluctuations is to be demonstrated as due to the instability of the flow which would occur in the absence of the fluctuations. Therefore, it is first necessary to know what the fluctuation-free state would be. However, the knowledge of the fluctuation-free state is ordinarily very difficult, and thus it is natural to investigate if there are alternatives. The observed mean flow is inevitably affected by the presence of fluctuations and therefore this state cannot be used to determine if the observed fluctuations may be attributed to an instability process. Instead of precisely calculating the basic state, an initial state may be arbitrarily prescribed. This allows the consideration of classes of initial states, whose stability may then be directly examined in order to deepen criteria for instability (Pedlosky (1987) [58]).

The *normal mode* method of solution of the perturbation problem consists of introducing on the initial state $\Psi(y, z)$ a sinusoidal disturbances of the form:

$$\phi(x, y, z, t) = \Re\Phi(y, z)e^{\imath k(x-ct)} \tag{2.32}$$

where k is the zonal wave number and $c = c_r + \imath c_i$ the phase velocity. If solutions of the form (2.32) are found with $c_i > 0$, then ϕ will grow exponentially since

$$\phi = \Re\Phi(y, z)e^{\imath k(x-c_r t)}e^{kc_i t}$$

The assumption of an exponential time factor is not the most general evolution form which a disturbance may take. However, if exponentially growing solutions are found, they grow faster that any algebraic power, and it is almost plausible that the associate perturbation will emerge first from the background of small disturbances. The wave number k for which kc_i is a maximum yields the wave number of the most unstable wave.

The normal mode problem for Φ is obtained by substituting relation (2.32) into Eq.ns (2.31) to obtain

$$\left(z - c\frac{H}{U}\right)\left(\frac{4\Omega^2}{N^2}\frac{\partial^2\Phi}{\partial z^2} + \frac{\partial^2\Phi}{\partial y^2} - k^2\Phi\right) = 0 \tag{2.33a}$$

$$\left(z - c\frac{H}{U}\right)\frac{\partial\Phi}{\partial z} - \frac{U}{H}\Phi = 0 \text{ at } z = 0, H \tag{2.33b}$$

Real flow are bounded along the y-direction, especially in laboratory experiments. The boundedness in y sets up normal modes in the form

$$\Phi(y,z) = A(z)\cos l_m y \qquad l_m = (m + 1/2)\pi/L \quad m = 0, 1, 2, \ldots \tag{2.34}$$

Then $A(z)$ satisfies

$$\left(z - c\frac{H}{U}\right)\left(\frac{\mathrm{d}^2 A}{\mathrm{d}z^2} - \mu^2 A\right) = 0 \tag{2.35a}$$

$$\left(z - c\frac{H}{U}\right)\frac{\mathrm{d}A}{\mathrm{d}z} - A = 0 \text{ at } z = 0, H \tag{2.35b}$$

where $\mu^2 = (k^2 + {l_m}^2)N^2/4\Omega^2$. The condition of nonsingular solutions of Eq.n (2.35a) and the application of Eq.n (2.35b) yields to

$$c = \frac{U}{2} \pm \frac{U}{\mu H}\left[\left(\frac{\mu H}{2} - \coth\frac{\mu H}{2}\right)\left(\frac{\mu H}{2} - \tanh\frac{\mu H}{2}\right)\right]^{1/2} \tag{2.36}$$

which shows that whether the solutions grow in time depends on the behavior of the

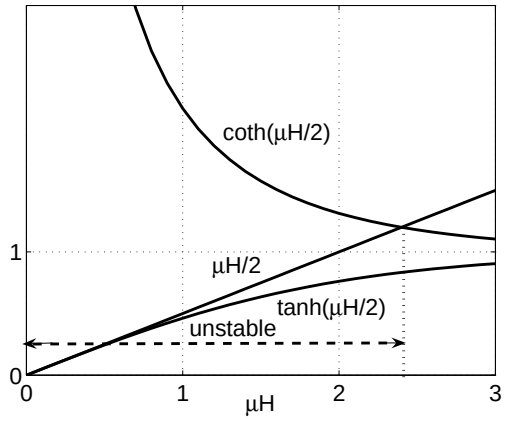

Fig. 2.4: Sketch of the behavior of the functions in Eq.n (2.36).

functions under the radical sign (Fig. 2.4). For all μ, $\mu H/2 \geq \tanh(\mu H/2)$ while $\mu H/2 < \coth(\mu H/2)$ for a critical value of $\mu H/2 = 1.20$. Thus, for the instability to occur must be $\mu H < 2.40$ or, using the definition of μ for the most unstable mode ($m = 0$),

$$k^2 + l_0^2 < 5.76/L_d^2 \;\rightarrow\; k < (5.76/L_d^2 - l_0^2)^{1/2} \tag{2.37}$$

The growth rate of the most unstable mode is

$$kc_i = \frac{kU}{\mu H}\left[\left(\coth\frac{\mu H}{2} - \frac{\mu H}{2}\right)\left(\frac{\mu H}{2} - \tanh\frac{\mu H}{2}\right)\right]^{1/2} \tag{2.38}$$

The structure of the unstable wave is

$$A(z) = \cosh\mu z - \frac{U\sinh\mu z}{\mu cH} \tag{2.39}$$

The solution (2.39) may be multiplied by an arbitrary constant since linear theory is incapable of determining the amplitude of the disturbance.

For $\mu H < 2.40$

$$\phi = |A(z)|e^{kc_i t}\cos l_m y\ \cos(kx - kc_r t + \alpha) \tag{2.40}$$

where the phase angle $\alpha = \alpha(z)$ is given by

$$\alpha(z) = \arctan\left[\frac{c_i U\sinh\mu z}{\mu|c|^2 H\cosh\mu z - c_r U\sinh\mu z}\right] \tag{2.41}$$

Chapter 3

Spin-up & Spin-down

Let us give a physical description of the transient approach to solid body rotation from the initial phases, through spin-up, until the final stages of the motion. We start with the homogeneous case since it gives insight on the most important mechanism of the spin-up process, i.e., the secondary circulation, which is altered by the stratification.

3.1 Homogeneous Case

3.1.1 The Linear Problem

A homogeneous fluid is confined between two horizontal coaxial infinite discs whose separation distance is $2H$. The discs are impermeable and the entire system is assumed to be in solid body rotation about its vertical axis. The rotation rate of both discs is then simultaneously increased of an amount $\Delta\Omega = \epsilon\Omega$. Although the fluid is laterally unbounded, the combination of two plane discs rotating in unison produces a motion which typifies all contained spin-up flows (Greenspan & Howard (1963) [32]).

Let H, Ω^{-1}, U characterize the typical length, time and horizontal velocity of a particular motion. The replacement of the variables $\vec{r}$, t, $\vec{u}$, $\tilde{p}$ by their scaled counterparts $H\vec{r'}$, $\Omega^{-1}t'$, $U\vec{u'}$, $\rho\Omega UH\tilde{p}'$ (e.g., Greenspan (1968) [30]) allows a reduction of the governing Eq.ns (2.4a) and (2.4b) to a non-dimensional form,

$$\frac{\partial \vec{u'}}{\partial t'} + \epsilon\vec{u'} \cdot \vec{\nabla}'\vec{u'} + 2\hat{k} \times \vec{u'} = -\vec{\nabla}'\tilde{p}' + E\nabla'^2\vec{u'} \tag{3.1a}$$

$$\vec{\nabla}' \cdot \vec{u'} = 0 \tag{3.1b}$$

Thus, the spin-up process of a homogeneous fluid is almost entirely determined by the Ekman number, $E = \nu/\Omega H^2$, and the Rossby number, $\epsilon = U/\Omega H = \Delta\Omega/\Omega$. If $E \geq 1$, the Coriolis effect is negligible, and the adjustment mechanism is simple viscous diffusion. We rather assume that viscosity is small, i.e., $E \ll 1$, and the adjustment mechanism is the more complicated but interesting convective spin-up process.

In the limit $\epsilon \to 0$, the advective term is negligible and Eq.n (3.1a) reduces to

$$\frac{\partial \vec{u'}}{\partial t'} + 2\hat{k} \times \vec{u'} = -\vec{\nabla}'\tilde{p}' + E\nabla'^2\vec{u'} \tag{3.2}$$

The axisymmetric form of this equation describes the linear spin-up problem, solved by Greenspan & Howard (1963) [32]. The detailed analysis, which uses Laplace transform method to convert partial to ordinary differential equations, is difficult and is not presented here. However, in quasi-steady approximation the resultant flow may be described in simple terms.

3.1.2 Quasi-Steady Ekman layer

The role of viscous force in geophysical fluid dynamics is related to the structure of the boundary layers. These layers exert a great influence on the dynamics of the flow even far from the regions directly affected by viscosity. Let us limit the analysis to bottom Ekman layer, pointing out that the treatment of the upper Ekman layer is specular since the system is symmetric about mid-depth.

In the literature, the frames of reference rotating with both initial and final angular velocities were considered when describing the spin-up process. In order to avoid ambiguity, let us briefly illustrate the development of the Ekman layer from both the points of view, assuming the fluid bounded by a horizontal surface at $z' = 0$.

In the reference system rotating with the *initial* angular velocity, the impulsive change in the rotation rate produces a shear layer at the bottom surface, which starts to thicken by diffusion. However, the background rotation implies that vertical fluid lines coincide with planetary vortex lines: the vortex line tilting due to the vertical shear of the horizontal velocity then just cancels the diffusion term. An Ekman layer arises, which becomes fully developed and quasi-steady after $t' \sim O(1)$.

The axial symmetry of the resultant flow allows a considerable simplification of the

governing equations (3.1b) and (3.2) when cylindrical coordinates are considered

$$\frac{1}{r'}\frac{\partial(r'u'_r)}{\partial r'} + \frac{\partial w'}{\partial z'} = 0 \tag{3.3a}$$

$$\frac{\partial u'_r}{\partial t'} - 2u'_\theta = E\frac{\partial^2 u'_r}{\partial z'^2} \tag{3.3b}$$

$$\frac{\partial u'_\theta}{\partial t'} + 2u'_r = E\frac{\partial^2 u'_\theta}{\partial z'^2} \tag{3.3c}$$

$$\frac{\partial w'}{\partial t'} = -\frac{1}{\rho}\frac{\partial \tilde{p}'}{\partial z'} + E\frac{\partial^2 w'}{\partial z'^2} \tag{3.3d}$$

In quasi-steady approximation, the Eq.ns (3.3b) and (3.3c) of the horizontal velocity components are

$$-2u'_\theta = E\frac{\partial^2 u'_r}{\partial z'^2} \tag{3.4a}$$

$$2u'_r = E\frac{\partial^2 u'_\theta}{\partial z'^2} \tag{3.4b}$$

The solution satisfying the boundary conditions

$$u'_\theta = r' \quad u'_r = 0 \quad \text{at} \quad z' = 0$$
$$u'_r, u'_\theta \to 0 \quad \text{as} \quad z' \to +\infty$$

is

$$u'_r(r', z') = r' e^{-z'/E^{1/2}} \sin(z'/E^{1/2}) \tag{3.5a}$$

$$u'_\theta(r', z') = r' e^{-z'/E^{1/2}} \cos(z'/E^{1/2}) \tag{3.5b}$$

Thus, a steady flow in a layer near the surface with thickness $z' \sim O(E^{1/2})$ is possible. This steady flow exhibiting a balance between the viscous and Coriolis forces was first noticed by Ekman (1905) [15] studying wind-stress on the ocean surface and it is named *Ekman spiral*. In the bottom layer there is a balance between the externally imposed stress, the friction which the upper exerts on the bottom layer, and the Coriolis force. This balance is reached after a transient motion. Immediately after the impulsive change in the angular velocity, the fluid velocity direction is that of the external stress. As the velocity increases, the Coriolis force turns the velocity direction in clockwise sense, then also the friction exerted by the upper on the bottom layer must turn. At the bottom the equilibrium is reached when the velocity direction is 45° in clockwise sense with respect to the external stress. Therefore, the fluid is transported azimuthally in the same direction as the disc, and the increase in Coriolis force produces a flow radially outwards.

Note that some authors (e.g., Benton & Clark (1974) [4]) explained the development of the Ekman layer as due to an increase of the centrifugal force near the horizontal rigid surface. In fact, they include in the centrifugal term also the radial component of the Coriolis force, which is responsible for the unbalance.

In the frame of reference rotating with the *final* angular velocity [1], the impulsive change in the rotation rate generates in the interior region a depth-independent clockwise azimuthal flow $U'_\theta(r') = -r'$ in geostrophic equilibrium, i.e., $-2U'_\theta(r') = -\partial\tilde{p}'/\partial r'$. The equations of the horizontal velocity components differ from Eq.s (3.4a) and (3.4b) only by the addition of a vertically uniform pressure gradient associated with the geostrophic interior flow. The solution satisfying the boundary condition

$$u'_\theta \to U'_\theta(r') \quad u'_r = 0 \quad \text{as} \quad z' \to \infty$$
$$u'_\theta, u'_r = 0 \quad \text{at} \quad z' = 0$$

is then

$$u'_r(r', z') = -U'_\theta(r') e^{-z'/E^{1/2}} \sin(z'/E^{1/2}) \tag{3.6a}$$
$$u'_\theta(r', z') = U'_\theta(r') \left[1 - e^{-z'/E^{1/2}} \cos(z'/E^{1/2})\right] \tag{3.6b}$$

In this case, the Ekman spiral is the result of the composition of three forces: the pressure gradient force, the Coriolis force and the viscous force. Far from the bottom, the velocity is entirely in the direction of the geostrophic flow. As the bottom is approached, the retarding effect of the friction decreases u'_θ, weakening the radial component of the Coriolis force, while the radial pressure gradient is independent of the depth. Therefore, a velocity in the radial direction must be produced at the bottom layer, flowing from high pressure to low pressure, retarded only by fluid friction. At the bottom surface the velocity vector has turned 45° in anticlockwise sense with respect to the geostrophic velocity. At the level $z' = \pi E^{1/2}$, u'_r nullifies and u'_θ becomes slightly bigger than the geostrophic value U'_θ. The viscous effect is indeed to break the constraint of exact geostrophic balance and produce a flow radially outwards.

The agreement between measured velocity profiles and theoretical predictions is very good for laminar and transitional regimes. Fig. 3.1 presents the results obtained by Sous *et al.*

[1] hereinafter only this frame of reference will be considered

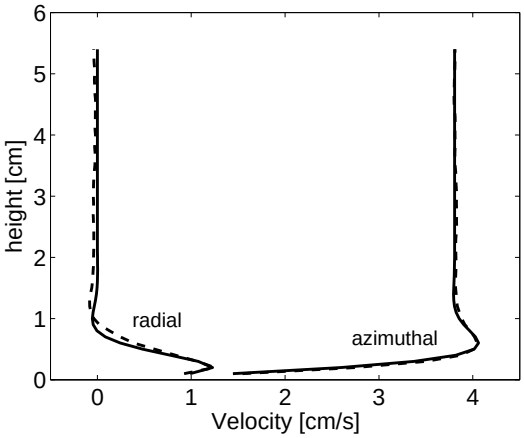

Fig. 3.1: Ekman layer: comparison between measured velocity profiles - - - and theoretical predictions —. Experimental profiles are obtained by averaging successive velocity fields around $t/T \simeq 62.5$, where $T = 40\,s$ is the tank rotation period. Reproduced from Sous *et al.* (2008) [69]

(2008) [69] in laboratory experiments using Stereoscopic Particle Image Velocimetry (¶ 4.4.1), an extension of the traditional Laser P.I.V. technique in which two cameras are used to obtain a depth perception, and thus give access to the out-of-plane component of the velocity.

The continuity Eq.n (3.3a) shows that the divergent radial Ekman flow induces a vertical velocity $w' = -E^{1/2}$ from the geostrophic interior toward the Ekman layer. Thus, the radial and azimuthal velocity components are everywhere proportional to the distance from the vertical axis of rotation, r', while the vertical velocity is independent of r' (Von Karman's similarity solution [2]). A consequence is that the interior azimuthal velocity is a time-dependent solid body rotation, evolving under the action of the horizontal Ekman layers which act to transform the no-slip condition on the horizontal velocity in a more appropriate normal flow condition on the interior flow. In addition, there are inertial oscillations [3], excited by the initial impulse, at twice the rotation frequency but of very small amplitude. Note that since the geostrophic approximation was assumed in the interior region, only information about the motion in the boundary regions is given, and the structure in the interior must be

[2]The similarity framework reduces Navier-Stokes equations from partial to ordinary differential equations, identifying solutions which depend on certain groupings of the independent variables rather than on each of the independent variables separately.

[3]Inertial oscillations, also known as inertial waves, are a type of stationary wave present in the bulk of the fluid, due to the restoring effect of the Coriolis force. A closed container imposes restrictions on the possible frequencies of the waves, then inertial waves are often called inertial modes.

determined.

The total flux per unit area in the Ekman layer caused by viscous force is

$$\begin{aligned}\vec{Q'} &= \hat{i}_r \int_0^\infty \tilde{u}'_r \, dz' + \hat{i}_\theta \int_0^\infty \tilde{u}'_\theta \, dz' \\ &= -\frac{E^{1/2}}{2} U'_\theta (\hat{i}_r + \hat{i}_\theta) \end{aligned} \tag{3.7}$$

being $\tilde{u}'_r \equiv u'_r$ and $\tilde{u}'_\theta \equiv (u'_\theta - U'_\theta)$ the departures from geostrophic flow induced by the presence of the viscous force. The divergence of Eq.n (3.7) is

$$\vec{\nabla'} \cdot \vec{Q'} == -\frac{E^{1/2}}{2} \frac{1}{r'} \frac{\partial (r' U'_\theta)}{\partial r'} = -\frac{E^{1/2}}{2} \omega'_z \tag{3.8}$$

being ω'_z the vertical vorticity of the geostrophic interior. The continuity equation then provides

$$w' = \frac{E^{1/2}}{2} \omega'_z \tag{3.9}$$

The vertical velocity is then proportional to the interior geostrophic vorticity. Lateral variations in the interior flow cause variations of the flux in the Ekman layer and force flow into, or out of, the interior. This mechanism is referred as *Ekman pumping/suction* according to the sign of the vertical velocity, as shown in Fig. 3.2.

The divergent radial flow in the Ekman layer is compatible with continuity requirements

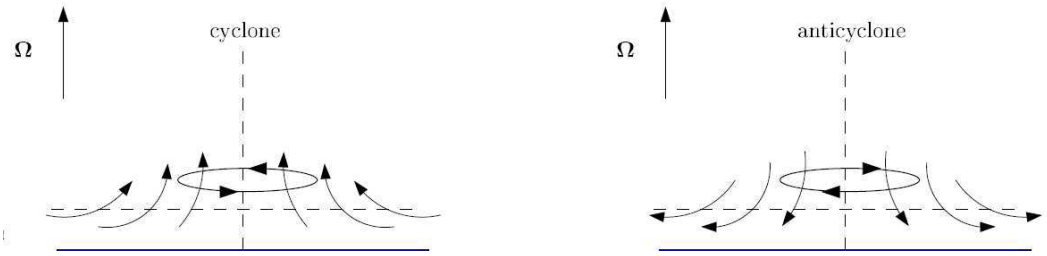

Fig. 3.2: Ekman pumping/suction sketch in case of cyclonic/anticyclonic interior velocity field.

only if an equal radial inflow with velocity $u'_r = -(1/2) r' E^{1/2}$ arises in the interior region. In this way the effect of the horizontal boundary layer is communicated directly to the interior region through a forced *secondary circulation*.

This slow induced Ekman secondary circulation causes planetary vortex tubes in the interior to contract slightly. Since the interior region is practically inviscid, then each vortex tube conserves its absolute circulation (Kelvin's theorem). Therefore, the planetary vortex lines will be gathered closer together, increasing the positive absolute vorticity by reducing the

interior negative relative vorticity. The required additional relative vorticity in the interior results from stretching of the planetary vortex lines by Ekman layer suction velocity. Using dimensional variables it is straightforward to show that the spin-up time may be interpreted as the time required for the interior vertical velocity $w = \epsilon\Omega H E^{1/2}$ to stretch a vortex line an amount ϵH (Benton & Clark (1974) [4]).

$$t \sim \frac{\epsilon H}{\epsilon\Omega H E^{1/2}} = \Omega^{-1} E^{-1/2} \rightarrow t' \sim E^{-1/2} \tag{3.10}$$

This result may be interpreted also as a consequence of the conservation of angular momentum of the fluid contained in the vortex tube. Such an interpretation is possible since the interior region is inviscid, and consequently the stress at the boundary of the vortex tube exerts no torque on the fluid inside. The Ekman layer acts as a sink from low angular momentum fluid in the interior, this fluid being replaced by high angular momentum fluid drawn from larger radii (Greenspan & Howard (1963) [32]).

From an alternate point of view, note that the cross-isobars flow in the Ekman layer from high (at the center) to low pressure (at the sidewall) means that work is being done on the fluid by pressure force. Even now using dimensional variables

$$\begin{aligned} \dot{W} = & -\int_0^\infty \vec{\nabla}\tilde{p} \cdot \vec{\tilde{u}}\, \mathrm{d}z = -\frac{\partial \tilde{p}}{\partial r} \int_0^\infty \tilde{u}_r\, \mathrm{d}z = \\ = & \ 2\Omega\rho U_\theta^2 \int_0^\infty e^{-z/\delta_E} \sin(z/\delta_E)\, \mathrm{d}z = \rho\Omega U_\theta^2 \delta_E \end{aligned}$$

being $\delta_E = HE^{1/2} = (\nu/\Omega)^{1/2}$ the dimensional thickness of the Ekman layer. This work is associated with an energy loss in the interior due to the radial flow from low pressure to high pressure. Thus, the energy loss in the interior region supplies energy to the fluid into the Ekman layer, where it is depleted by viscous force. A geostrophic layer of fluid of depth H, moving with velocity U_θ, possesses a kinetic energy per unit area $K = (1/2)\rho U_\theta^2 H$ and supplies energy at a rate $\dot{W}$ to the Ekman layer. Unless externally maintained, the geostrophic flow will decay through viscous dissipation in a time $t = K/\dot{W}$ identical to Eq.n (3.10) (Pedlosky (1987) [58]).

As the interior fluid spins-up, the driving angular velocity gradient across each Ekman layer weakens, so that the secondary circulation is then eliminated. Finally, at very large times, $t' \sim O(E^{-1})$, viscous diffusion has affected the whole interior region and residual motions are dissipated.

Thus, although the initial and final state of solid body rotation are simple, the transient motion is non-trivial since it involves three time scales corresponding to three distinct physical mechanisms

1. the development of the Ekman layers for $\tau_e = \Omega^{-1}$
2. the spin-up process for $\tau_s = \Omega^{-1}E^{-1/2}$ defined as the time required for the fluid to reach the final state of solid body rotation
3. the viscous decay of any residual motion for $\tau_v = \Omega^{-1}E^{-1}$

All the above results were inferred by Greenspan & Howard (1963) [32] from suitable approximations to the exact Laplace transform solution, which exists for the simple double-disc container. An approximation of the interior azimuthal flow during spin-up time scale (which omits inertial oscillations as well as boundary layer formation) is simply

$$u'_\theta(t') = U'_\theta e^{-t'/\tau'_s} \tag{3.11}$$

3.1.3 Axisymmetric Container

To cope with axisymmetric containers Greenspan & Howard (1963) made use of the concepts of boundary layer theory. In order to determine the flow in the interior region a rigorous procedure is necessary to include small non-geostrophic forces, i.e., the vortex-tube stretching by Ekman suction velocity. Briefly, the basic idea is that, in situations in which the Ekman number is small, the direct effect of viscosity is restricted to thin Ekman layers, while the interior region can be regarded as essentially inviscid. A vertical stretched variable $\zeta = z'/E^{1/2}$ is introduced in the Ekman layers: in these regions the flow is function of the vertical coordinate scaled by the Ekman layer thickness, i.e, $\zeta = z/\delta_e$, rather by the vertical length scale H. Consequently, as $\delta_e \to 0$, the highest derivatives pertinent to the viscous force vary so rapidly that the viscous term becomes important in the Ekman layers even though $E \to 0$, i.e.,

$$E\frac{\partial^2 u'_\theta}{\partial z'^2} = \frac{\partial^2 u'_\theta}{\partial \zeta^2} = O(1)$$

Since the parameter separating the different time scales is $E^{1/2}$, an approximate solution uniformly valid through the spin-up time is sought by introducing into the governing equations an expansion of the solutions in half power of the Ekman number. A quasi-geostrophic inviscid motion in the interior region is matched to a motion in the viscous Ekman layers as to satisfy the boundary conditions. Greenspan & Howard (1963) showed that the fluid spin-up is still completed by the same basic process as occurs between parallel discs, and again in a time $\tau'_s \sim O(E^{-1/2})$. The motion in the interior region is again columnar, but the interior angular velocity at any time $t' < \tau'_s$ is horizontally non uniform (e.g., in a sphere the

fluid at larger radii spins-up more rapidly).

The previous explanation is appropriate if the container has no finite parts of its boundaries parallel to the rotation axis. In this situation, the balance of forces necessary to produce an Ekman layer is not possible on the sidewall, and the expectation was that spin-up may be substantially affected. This conjecture was proved to be wrong: a set of two vertical boundary layers, named *Stewartson layers*, arises from a balance which involves Coriolis force, pressure gradient and *radial* viscous force. Anyway, Ekman layers still form on the horizontal boundaries and these continue to produce spin-up of interior fluid exactly as in double-disc system. The Stewartson layers, of thickness $\sim O(E^{1/4})$, satisfy the no-slip condition for radial as well azimuthal velocities, but are too thick to provide sufficient viscous stresses on the vertical motion. It turns out that an inner layer is required, of thickness $\sim O(E^{1/3})$, in which the flux flowing radially outward in the Ekman layers is turned into the vertical direction. The Stewartson layer is so wide that cannot affect the Ekman layer below it, in which the analysis applies as an ordinary geostrophic flow were located above. Note that the vertical turning of the fluid at the sidewall does not happen only for reasons of continuity. The vertical velocity depends on the sign of the vorticity in the interior region relative to the horizontal boundaries (cf., Eq.n 3.9). Far from the sidewall the vorticity of the boundaries is larger than that of the interior region, therefore the fluid is sucked into the Ekman layer. At the sidewall, the initial vorticity is diffused by viscosity in the Stewartson layer, providing a high fluid vorticity, greater than that at the bottom boundary. Thus, the fluid does not simply enter into the sidewall, but is pumped out of the Ekman layers. The nearly inviscid core in the interior region is not directly affected by the vertical sidewall layers, which are essentially steady on the spin-up time scale, and thus the spin-up process is accomplished as in the case of double-disc system.

If the container is open at the top and the fluid held in it by gravity, the treatment at the upper surface must obviously be modified. The first consequence of a free surface is that, in first approximation, the viscous effects at the top surface are removed: the interior flow may be considered as extending to the upper surface. Secondly, the change in the shape of the free surface between the initial and final parabolic surfaces induces an additional radial motion, modifying the spin-up process. The importance of this effect relative to the secondary circulation is measured by the Froude number [4], $F = \Omega^2 L^2/gH$, where Ω is the angular velocity of the basic rotation. If F is very small, the upper boundary may be considered to be essentially

[4]The Froude number indicates the ratio of advective term to gravitational force.

horizontal.

The theoretical predictions of Greenspan & Howard (1963) were shown to be in good agreement with both numerical computations and laboratory measurements, e.g., Warn-Varnas *et al.* (1978) [75].

3.2 Stratified Case

A continuously salt-stratified fluid is assumed to be in solid body rotation inside a right circular cylinder. Note that the condition for static equilibrium is $\vec{\nabla}\tilde{p} \times \vec{\nabla}\tilde{\rho} = 0$ (cf., Eq.n (2.16a)), but the isobaric surfaces are paraboloids of revolution and the isopycnal surfaces cannot be parallel because of diffusive processes. Therefore, such a state is not possible and a relative flow, referred to as *Sweet-Eddington* circulation, occurs. We ignore this circulation, which can be justified providing a small Froude number. Consequently, in solid body rotation the isopycnal surfaces were assumed to be essentially parallel to the horizontal.

In stratified fluid the physical structure of the system is substantially more complicated, and so the analysis. However, the homogeneous case has shown the existence of separated time scales (i.e., development of Ekman layers, secondary circulation response, viscous effects), suggesting a multi-timing treatment of the spin-up process.

Even now, let H, τ, U characterize the typical length, time and relative velocity of a particular motion, restricting the analysis to the linear case. The replacement of the variables $\vec{r}, t, \vec{u}, \tilde{p}, \tilde{\rho}$ by their scaled counterparts $H\vec{r'}$, $\tau t'$, $U\vec{u'}$, $\Omega U H \rho_0 \tilde{p}'$, $\Omega U \rho_0 \tilde{\rho}' g^{-1}$ (e.g., Duck & Foster (2001) [13]) allows a reduction of the governing equations (2.16) to a non-dimensional form,

$$\tau' \frac{\partial \vec{u'}}{\partial t'} + 2\hat{k} \times \vec{u'} = -\vec{\nabla}'\tilde{p}' - \tilde{\rho}'\hat{k} + E\nabla'^2\vec{u'} \tag{3.12a}$$

$$\vec{\nabla}' \cdot \vec{u'} = 0 \tag{3.12b}$$

$$\tau' \frac{\partial \tilde{\rho}'}{\partial t'} - \frac{Bu}{\delta^2}\vec{u'} \cdot \hat{k} = \frac{E}{\sigma}\nabla'^2\tilde{\rho}' \tag{3.12c}$$

Three additional non-dimensional parameters pertinent to rotating stratified flows appear: the Schmidt number, $\sigma \equiv \nu/\kappa$, which indicates the relative importance of momentum diffusion to density diffusion; the Burger number Bu; and a time-scale parameter $\tau \equiv \Omega^{-1}\tau'$. Note that in case of thermally stratified fluid the appropriate non-dimensional number is the Prandtl number, $Pr = \nu/\chi$.

In a *NaCl*-saline solution $\sigma \sim O(10^3)$ ($T \sim 20°$, any concentration), while in fresh water

$Pr = O(10)$ ($20° \leq T \leq 100°$). These differences do not imply discrepancies in the dynamics of the spin-up since the role of density (temperature) diffusion during the spin-up process becomes important only in case of small σ (Pr) (Sakuray *et al.* (1971) [64]).

The influence of stratification is easily seen referring to Eq.n (3.12c) in case of quasi-steady flow

$$\frac{Bu}{\delta^2} w' + \frac{E}{\sigma} \nabla'^2 \tilde{\rho}' = 0$$

Since in salt-stratified flow $\sigma Bu/\delta^2 \gg E^{1/2}$, the Ekman vertical velocity $w' \sim O(E^{1/2})$ is larger than the vertical advection necessary to balance the density diffusion, i.e., $w' \sim O(\delta^2 E/\sigma Bu)$, and thus it is expected that the flow will be significantly different from the homogeneous case (Linden (1977) [45]).

The process of spin-up of a stratified fluid in a circular cylinder was studied by Holton (1965) [34], who considered the spin-up time scale derived by Greenspan & Howard (1963) in homogeneous fluid, i.e., assuming $\tau' = \tau'_s = E^{-1/2}$. Information in a time scale of $O(1)$ is lost with this substitution, but it has principally to do with inertial-internal gravity modes [5] which are not important for the determination of the spin-up process. Holton (1965) showed that the Ekman layers have the same structure as in homogeneous case since the vertical buoyancy force cannot directly affect its horizontal force balance. Furthermore, density variations do not occur on the small $O(E^{1/2})$ scale of the Ekman layer. Rather, there is a thicker $O(E^{1/4})$ diffusive boundary layer in which density adjustments occur. Therefore, simple Ekman layers develop and the resulting spin-up process is independent of the density conditions on the horizontal boundaries.

A second conclusion from Holton's work is that the interior dynamics is no longer dominated by the Taylor-Proudman theorem (Eq.n (2.11)). Using boundary layer theory Holton (1965) showed that the inviscid interior is governed on the spin-up time scale $\tau'_s \sim O(E^{-1/2})$ by the linearized form of the quasi-geostrophic potential vorticity equation (2.25). In non-dimensional variables

$$\nabla'^2_H \psi' + \frac{\delta^2}{Bu} \frac{\partial^2 \psi'}{\partial z'^2} = 0 \tag{3.13}$$

which provides for an elliptic equation in terms of the time derivative of the lowest order interior pressure field, $\psi' \equiv \partial \tilde{p}'_{(0)}/\partial t'$. Note that the first and the second term in Eq.n (3.13) are, respectively, vertical relative vorticity and vertical stretching. Fixed δ, if $Bu \ll 1$, i.e., weak stratification, vertical stretching dominates, and Eq.n (3.13) reduces to $\partial^2 \psi'/\partial z'^2 = 0$, a

[5] The inertial oscillations excited by the impulsive spin-up are modified by the stratification, resulting in inertial-internal gravity modes.

form of the Taylor-Proudman theorem valid in the homogeneous case. On the other hand, if $Bu \gg 1$, i.e., strong stratification, then the mechanism of vortex stretching is essentially eliminated, and the relative vorticity is conserved for time scales shorter than those of viscous dissipation and density diffusion.

The determination of ψ' requires only specification of a boundary condition sufficient to solve the elliptic equations (3.13), and may be formulated in terms of the vertical velocity evaluated at the top of the Ekman layer. The aim of the analysis is to determine the development in time of the lowest order fields

$$\frac{\partial u'_{\theta\,(0)}}{\partial t'} = \frac{\partial \psi'}{\partial r'} \tag{3.14a}$$

$$\frac{\partial \tilde{\rho}'_{(0)}}{\partial t'} = -\frac{\partial \psi'}{\partial z'} \tag{3.14b}$$

$$u'_{r\,(0)} = w'_{(0)} = 0 \tag{3.14c}$$

Holton (1965) showed that the state resulting from the spin-up process is characterized by non-uniform rotation such as

1. adjacent to the horizontal boundaries, just outside of the Ekman layers, the fluid rotates at the new angular velocity;

2. further away from the horizontal boundaries, the angular velocity discrepancies between the fluid and the boundaries continuously increase on a vertical scale $h_p \sim H/Bu^{1/2}$, a relation first given by Rossby (1938) [60] [6];

3. the recirculation process and penetration depth of the fluid ejected from the Ekman layers into the interior flow is governed by the Burger number. If $Bu \gg 1$, the spin-up of the interior fluid is confined to thin layers near each horizontal boundary, named *rotational shear layers*. The state is quasi-steady, characterized by a linear vertical shear in the azimuthal velocity. Since there are no differences in local angular velocity between the Ekman layers and the adjacent fluid, then no further Ekman pumping occurs.

Holton (1965) based his analysis of the interior region on a mathematically convenient, but arbitrary, condition imposed at the sidewall ($\tilde{p}'_{(0)} = 0$ rather than the correct $\partial \tilde{p}'_{(0)}/\partial r = 0$). He recognized that this assumption does not satisfy the boundary conditions, and boundary layers are required. However, he stated that the sidewall boundary layers play only a passive role in closing the secondary circulation.

[6] note that the original relation was $h_p \sim L/S^{1/2}$, being $S = Bu/\delta^2$

Pedlosky (1967) [56] attempted to obtain a solution for the sidewall layer which closed the secondary circulation. He showed correctly that, when the sidewall is insulated, the vertical boundary layer is unable to carry the $O(E^{1/2})$ mass flux discharged from the Ekman layer at the corners. The physical reason is the inhibition of the vertical motions by buoyancy force, and consequently there is no radial influx from the sidewall layers to the interior. However, he was not able to match the interior solution to the sidewall layer, and this led him to assume that there are no Ekman and Stewartson layers, and viscous diffusion rather than Ekman layer suction were important in the fluid interior.

Holton & Stone (1968) [36] noted that the results of Pedlosky (1967) were at variance with experimental observations also presented by Holton (1965), and pointed out certain inconsistencies with some of Pedlosky's scaling arguments.

The correct model for stratified spin-up was finally derived by Walin (1969) [74] and Sakuray (1969) [62]. They agreed with Pedlosky's considerations about the sidewall boundary layer, but showed that the secondary circulation still exists. Walin (1969) and Sakuray (1969) demonstrated that in the corner region there is the formation of a jet which returns the Ekman layer flux directly into the interior region, forming a meridional secondary circulation restricted to a region adjacent to the Ekman layers. Therefore, in the interior region there is no net contraction of the total bundle of planetary vortex lines, and the interior vertical relative vorticity remains constant in time. Although the total relative vorticity does not increase, the existing relative vorticity imposed by the change in the rotation rate is rearranged. The radial transport of fluid within the Ekman layer induces a vertical velocity which acts to stretch fluid columns and so increases the relative vorticity, generating a downward deformation of the initial isopycnal surfaces. In contrast, the isopycnal surfaces at the sidewall are deformed vertically upwards, causing compression of the fluid columns and a decrease of the relative vorticity. Finally, the net result is to shift the relative vorticity toward the center.

A complete analogy between salt-stratified and thermal-stratified fluids is not possible. In fact, in case of thermal stratification the fluid may or may not exchange heat with the sidewall, depending on the boundary conditions. Instead, in salt-stratified case the sidewall does not allow salt diffusion, and only the non-diffusive boundary condition is applicable. Note that the case of fixed-temperature (diffusive) sidewall was also analyzed (e.g. Sakurai (1969) [61]; Sakuray *et al.* (1971) [63]). Since the fluid may exchange heat with the sidewall, the buoyancy constraint on the vertical boundary layer is not so severe. Calculations show that part of the Ekman layer flow goes through the sidewall layer and part goes directly in

the interior region. Thus, both vorticity production and rearrangement are involved.

When discussing stratified spin-up problems care must be taken concerning the definition of a spin-up time. Since the adjustment is localized and thus position dependent, it is possible to achieve a quasi-steady localized spin-up on the fast time scale

$$\tau'_{ss} \sim \left(\frac{\nu}{\Omega h_p^2}\right)^{-1/2} = \frac{\tau'_s}{Bu^{1/2}} \tag{3.15}$$

which is simply the usual Ekman spin-up time τ'_s valid in the homogeneous case, but based on the effective penetration depth of the secondary circulation, i.e.,

$$h_p \sim H/Bu^{1/2} \tag{3.16}$$

Nevertheless, defining the spin-up time as the time in which the bulk of the fluid adjusts to solid body rotation, then the time taken to spin-up is the longer diffusive time scale $\tau'_v = E^{-1}$. The solution for the lowest order interior velocity and density fields are usually expressed by means of Bessel functions J_α

$$u'_{\theta\,(0)} = -r'\delta + \sum_{n=1}^{\infty} C_n \frac{\cosh m_n z'}{\cosh m_n} J_1(\alpha_n r'\delta)[1 - \exp(-t'/\tau_n)] \tag{3.17a}$$

$$\tilde{\rho}'_{(0)} = \sum_{n=1}^{\infty} \frac{m_n}{\alpha_n} C_n \frac{\sinh m_n z'}{\cosh m_n} J_0(\alpha_n r'\delta)[1 - \exp(-t'/\tau_n)] \tag{3.17b}$$

where $C_n \equiv -2/\alpha_n J_0(\alpha_n)$, $m_n \equiv Bu^{1/2}\alpha_n/\delta$, $\tau_n \equiv (2m_n^2)^{-1/2} \tanh m_n$, and α_n are zeros of the first-order Bessel function.

The qualitative features of Eq.n (3.17a) are illustrated in Fig. 3.3. When $Bu^{1/2}$ is small compared with 1 (Fig. 3.3(a)), the process is essentially identical to the spin-up of a homogeneous fluid, except in a region of thickness $Bu^{1/2}L$ close to the vertical sidewall. When $Bu^{1/2}$ is large compared with 1 (Fig. 3.3(b)), the spin-up process only penetrates to the dimensional height $H/Bu^{1/2}$.

3.3 Previous Works in the Axisymmetric Case

Early laboratory spin-up experiments on stratified flows were performed by Holton (1965) [34], McDonald & Dicke (1967) [49] and Modisette & Novotny (1969) [52] using salt-stratified fluids in circular cylinders. Holton (1965) obtained relative velocities of the fluid by timing the angular displacements of wax pellets which were made neutrally buoyant at various levels. Holton's experiments demonstrated the essential features of the spin-up flow, but the

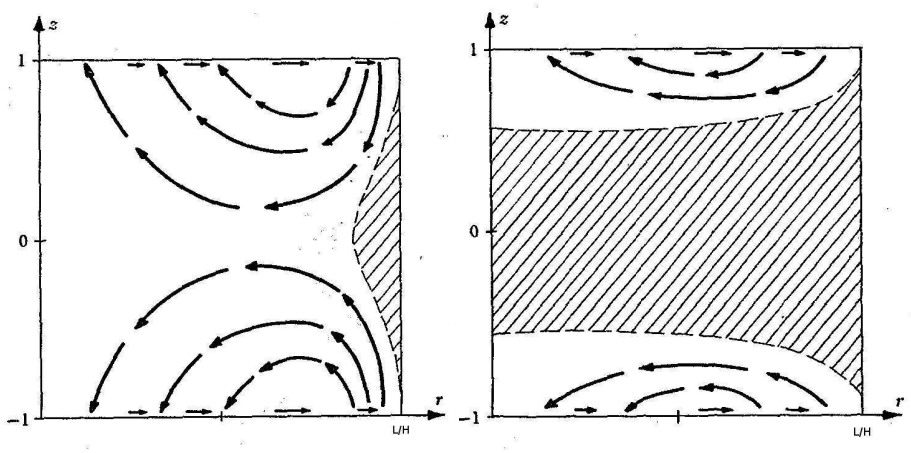

(a) $Bu^{1/2} \sim 0.1$ (b) $Bu^{1/2} \sim 10$

Fig. 3.3: Sketch of the secondary circulation for $t' \sim O(1)$ with weak ($Bu^{1/2} \sim 0.1$) and strong ($Bu^{1/2} \sim 10$) stratification. The shaded areas are essentially unaffected by the secondary circulation. Reproduced from Walin (1969) [74].

quantitative agreement with his linear theory was fortuitous since the sidewall boundary condition used (perfectly conducting sidewall) was inappropriate to his experimental configuration (salt-stratified fluid) (Buzyna & Veronis (1971) [6]).

McDonald & Dicke (1967) observed the damping of the azimuthal motion of the fluid by the use of free surface floats. They concluded that the occurrence of Ekman pumping can be inhibited or eliminated by a sufficient density gradient in the fluid. However, McDonald & Dicke could not easily sense the spin-up process with surface floats, but rather they were observing primarily the viscous-diffusion effects.

Modisette & Novotny (1969) repeated and extended the experiments of McDonald & Dicke (1967). They interpreted McDonald & Dicke's conclusions to mean that convective spin-up can be prevented by a density gradient, and attempted to find a transition between a convective and a purely viscous spin-up. However, their results were of insufficient accuracy due to the coarse nature of their experimental technique.

More accurate experimental studies were conducted by Buzyna & Veronis (1971) [6], Saunders & Beardsley (1975) [66], and Lee (1975) [43]. Buzyna & Veronis (1971) used a salt-stratified fluid in a circular cylinder, measuring the motion of initially radial dye lines in order to obtain the angular displacements of the fluid. They found that, even at relatively small Rossby numbers, the interior fluid spins-up more quickly than predicted by Walin's asymptotic theory. Buzyna & Veronis then speculated that non-linear effects near the corner

regions may be important even at small Rossby numbers. They also noted that the diffusion of salt at the horizontal boundaries before the spin-up decreases the density gradient. The weaker stratification near the boundaries may permit deeper penetration of the secondary circulation, and thus produce longer spin-up time and better agreement with theory.

Saunders & Beardsley (1975) avoided the density diffusion difficulties by using a thermally stratified fluid in a cylinder with insulated sidewall but fixed temperature at the horizontal boundaries. They measured the temperature perturbation field with an array of thermistors and generally found that the measured azimuthal velocities decayed faster than predicted by the theory of Walin (1969). Various causes such as thermal variation of viscosity and probe drag were postulated to account for the discrepancies, which were function of the strength of stratification and the location in the fluid. They noted also that the possibility of baroclinic instability existed, but estimates of the growth rate indicated that they would not be seen on a time scale as short as spin-up.

Lee (1975) used the disturbance-free, high resolution, laser Doppler velocimeter measuring technique in a thermally stratified fluid. He also found that, in general, the measured azimuthal velocities showed faster decay rates than Walin's theory. This established that probe drag alone was not responsible for the discrepancies in previous studies. Lee (1975) detected the oscillations excited by the impulsive start and showed that they were internal-inertial gravity modes. However, he made no measurements of the meridional flow.

Barcilon *et al.* (1975) [1] pointed out that, for high values of the Burger number, the spin-up time is comparable with the rotation period, a circumstance that invalidates the theory, based on a multi-timing treatment of the spin-up process. They performed numerical experiments on thermally stratified spin-up in a circular cylinder, solving the Navier-Stokes equations in axisymmetric form by means of finite-difference technique on a uniform grid. Barcilon *et al.* (1975) again found that the model results decayed faster than the theory of Walin (1969) and established that the effects of non-linearity were not the cause of the discrepancies in the range $\epsilon \leq 0.10$. The meridional stream function plots by Barcilon *et al.* (1975) showed the progressive confinement of the meridional circulation into regions adjacent to the Ekman layers as the stratification increases. From an examination of these plots, they pointed to an oscillation of the inclination of the corner-jet between near horizontal and near vertical positions, claiming an oscillation period of two or three times the rotation period. Barcilon *et al.* (1975) then argued that this oscillation of the corner-jet causes that some fluid spends more time in the viscous vertical boundary layer than it would if the jet was inclined at a

steady angle to the vertical, as given by Walin's theory. While this fluid is within the vertical boundary layer, viscous shear adjusts its angular velocity to that of the sidewall more efficiently than for the interior fluid. The fluid ejected into the interior from the vertical boundary layer yields its newly acquired angular momentum to the interior region. Thus, according to Barcilon *et al.* (1975), the fluid that is first forced into the vertical boundary layer and than into the interior region provides a mechanism for spinning-up the bulk of the fluid.

Later, numerical simulations were carried out by Hyun *et al.* (1982) [39], extending the model of Warn-Varnas *et al.* (1978) [75] to incorporate the effects of thermal stratification. The numerical model was checked by comparing the predictions with the accurate measurements of Lee (1975), showing an excellent agreement. Then, Hyun *et al.* (1982) made a discussion of their numerical results and a comparison with the linearized theory of Walin (1969). Let us summarize the most important points

- The interior azimuthal velocities are spatially non-uniform on the spin-up time scale.

- In the interior, well away from the Ekman layers, the flow decays initially at a slower rate as the stratification increases. On other hand, in the interior, close to the Ekman layers, the flow decays initially at a faster rate as the stratification increases. These results were interpreted as showing the effect of the progressive confinement of the meridional circulation by stratification.

- In general, spin-up proceeds initially more rapidly at smaller radii and decreases as the radius increases, until the viscous boundary layer on the outer wall is reached. This result confirms that the vortex-stretching by meridional circulation is not spatially uniform, but it is stronger at smaller radii

- The overall disagreements between the theory of Walin (1969) and the numerical results, aside from the presence of inertial-internal gravity modes (which were omitted from the theory), are appreciable. In general, there is initial agreement for a time after the impulsive start, but the curves begin to diverge, with the numerical results decaying faster than the theory. The theory accurately predicts the flow evolution in case of locations and times for which the secondary circulation is strong. Correspondingly, if the meridional flow is weak, then agreement is poor.

- The results are only weakly dependent on the Rossby number, and hence non-linearity cannot account for the discrepancies between the theory and the experiments in the range $\epsilon \leq 0.22$.

- The oscillation of the corner-jet inclination was shown to be the result of the superposition of meridional circulation flow and inertial internal gravity modes. This oscillation was noticed previously by Barcilon *et al.* (1975), but they claimed to have observed a much larger period. Hyun *et al.* (1982) suggested that, probably, their error arose from having too few stream function plots, which in turn led to aliasing of the oscillations. In order to account for the experimentally observed faster spin-up, Barcilon *et al.* (1975) argued that this oscillating corner-jet transports angular momentum from the sidewall boundary layer into the interior region. However, since the inward radial distance moved by a fluid particle during the meridional circulation phase of the spin-up is $O(\epsilon R)$, the fluid ejected from the sidewall boundary layer would not reach the interior region. Therefore the suggestion of Barcilon *et al.* (1975) is shown to be untenable

Since the effects of non-linearity and other possible sources were shown to be unimportant, Hyun *et al.* (1982) concluded that the observed discrepancies between the theory and the numerical results on the spin-up time scale are due to viscous diffusion in the interior region, which was omitted from the theory. The effects of viscous diffusion in the interior are enhanced for stratified over homogeneous spin-up since the meridional circulation in presence of stratification produces vertical gradients of azimuthal velocity, whereas in homogeneous fluid the azimuthal velocity decay is essentially independent of the vertical axis.

The above conclusion concerning the viscous effects in the interior region was verified

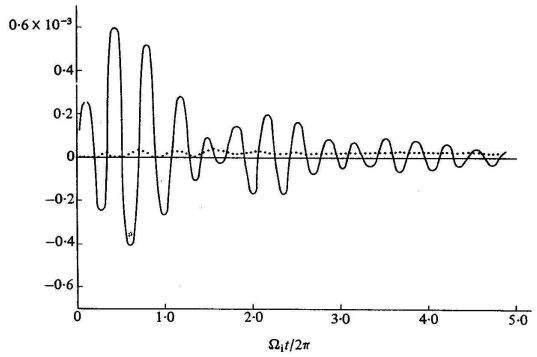

Fig. 3.4: Plot of Coriolis (solid line) and viscous terms (broken line). The ordinate shows the values in c.g.s. units. Simulation for a medium stratified fluid. Reproduced from Hyun *et al.* (1982) [39].

by examining the size of each of the terms in the equation of the azimuthal velocity. In

dimensional variables (cf., Eq.n (2.16a))

$$\frac{\partial u_\theta}{\partial t} = -\frac{1}{r}\frac{\partial}{\partial r}(r u_r u_\theta) - \frac{\partial}{\partial z}(w u_\theta) - \left(2\Omega + \frac{u_\theta}{r}\right)u_r + \nu\left(\nabla^2 u_\theta - \frac{u_\theta}{r^2}\right)$$

Among the terms on the right-hand side of this equation, the non-linear advective terms and the curvature term are several order of magnitude smaller than the Coriolis term, for the linearized problem. Hyun *et al.* (1982) noticed that the Coriolis term oscillates with the period of the inertial-internal gravity modes and, since the theory of Walin (1969) filtered out the inertial-internal gravity modes, the Coriolis term used in Walin's formulation would be obtained by averaging the Coriolis term measured by Hyun *et al.* (1982) over one period of the inertial-internal gravity oscillation. Fig. 3.4 shows that this averaged Coriolis term is larger than the viscous term for early times, but after about one rotation period the averaged Coriolis term becomes comparable to or even smaller than the viscous term. Therefore, omitting the viscous term and retaining only the averaged Coriolis term, as in Walin's theory, would lead to an appreciable underestimation of the acceleration of the fluid in the azimuthal direction.

Other numerical investigations of the thermally stratified problem were conducted by Hyun (1984) [38]. He confirmed that the relative vertical vorticity profiles show an appreciable dependence on the vertical position through the flow field, pointing to the existence of substantial flow gradients.

Spin-up of a stratified fluid is indeed controlled by both inviscid and viscous-diffusion effects. The relative importance of these two is a function of the strength of stratification and the location in the fluid. In the interior region, close to mid-depth, the limited penetration of the meridional circulation creates large flow gradients, which give rise to the dominance of viscous-diffusion over inviscid effects. On the other hand, at a location adjacent to the Ekman layers, the meridional circulation is the principal contributor to spin-up, and thus inviscid overcome viscous-diffusion effects. (Hyun (1983) [37]).

Chapter 4

Experiments, Instruments and Measurements

4.1 Overview

The physical system to be investigated is sketched in Fig. 4.1. An open right cylindrical

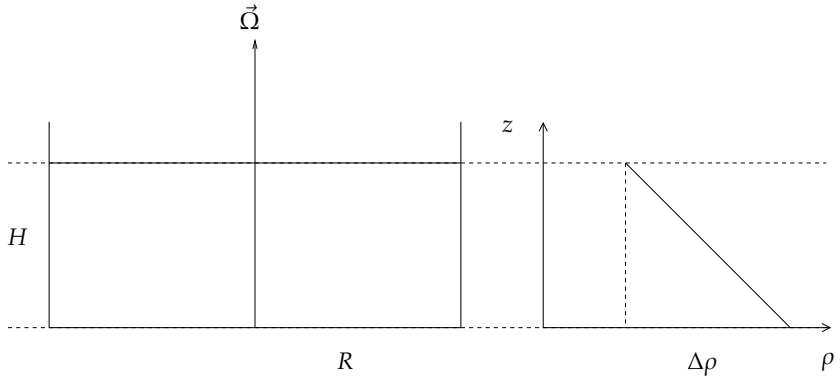

Fig. 4.1: Schematic representation of the physical system

vessel of radius R contains linearly salt-stratified fluid of depth H in solid body rotation at $t = 0$. The increase (decrease) in the angular velocity of the tank generates an anticyclonic (cyclonic) current in the interior region along the azimuthal direction.

The time response of the flow depends on seven dimensional parameters: the rotation rate Ω, the change in the rotation rate $\Delta\Omega$, the buoyancy frequency N, the horizontal length scale L (= R), the depth of the fluid layer H, the kinematic viscosity ν, and the salt diffusivity κ. Using dimensional analysis, the problem can be described conveniently in terms of five

non-dimensional parameters which we take as the Rossby number ϵ, the Burger number Bu, the (vertical) Ekman number E, the aspect ratio δ, and the Schmidt number σ. The fluid depth is kept constant in all the experiments, the Ekman number is very small ($E \sim O(10^{-5})$), and the Schmidt number is large ($\sigma \sim O(10^{3})$). Consequently, the flow evolution depends only on the Burger and Rossby numbers.

A series of spin-up and spin-down run pairs were performed, fixing the final rotation rate of the tank for each pair in order to make a quantitative comparison between spin-up and spin-down at otherwise the same parameters. The angular velocity of the tank was changed from Ω_i to $\Omega = \Omega_i \pm \Delta\Omega$, and thereafter kept constant during each experimental run. The change in the rotation rate of the tank was performed in a time interval of approximatively five seconds, and therefore may be considered as impulsive.

Even if the flow behavior differences in our experiments do not depend on the Ekman number, it is a fundamental parameter in the spin-up process. In fact, as previously explained, the theory of stratified spin-up relies on a multi-timing treatment which reflects the existence of separated time scales (i.e., development of Ekman layers, secondary circulation response, viscous effects). The separation of the three time scales is $O(E^{-1/2})$ (cf., ¶ 3.1), and therefore a very small Ekman number is suitable to properly compare the experimental results with the analytical theory of Walin (1969). Table 4.1 shows the spatial dimensions, the aspect

EXP	**H**	**L**	δ	**E**
Buzyna & Veronis (1971)	6	9.5	0.32	$\sim O(10^{-4})$
Saunders & Beardsley (1975)	4.5	10	0.45	$\sim O(10^{-4})$
Lee (1975)	3	9.5	0.32	$\sim O(10^{-4})$
Kanda (2004)	30	46	0.65	$\sim O(10^{-5})$
Smirnov *et al.* (2005)	19	91	0.14	$\sim O(10^{-4})$

Tab. 4.1: List of the most representative runs of the previous experimental realizations of incremental stratified spin-up (entire system). H and L are, respectively, the vertical and horizontal length scale [cm], δ is the aspect ratio [$-$], E is the Ekman number [$-$].

ratio and the Ekman number for the most representative runs of the previous experimental investigations of incremental stratified spin-up. Note that the first three studies used a closed container, and therefore half depth of the fluid layer has been reported since the system is symmetric about mid-depth. Table 4.1 shows that the value $E \sim O(10^{-5})$ is approached only in the study of Kanda (2004) [40], but this analysis was focussed on the evolution of

isolated baroclinic vortices, rather than on the instability mechanism itself. Moreover, our experimental study ($\{H, L, \delta, E\} = \{60, 650, 0.09, \sim O(10^{-5})\}$) is characterized by a small expect ratio, which allows the results to be relevant in geophysical applications.

Obviously, a better separation between the time scales implies a longer spin-up time scale, which can thus be properly analyzed. Our aim is therefore double

- in **axisymmetric case**, the viscous-diffusion effects, enhanced in stratified over homogeneous spin-up, can be influent not only in the viscous, but also in the shorter spin-up time scale

- in **non-axisymmetric case**, the long-wave instability is expected to develop already in the spin-up time scale, and its effects on the transport of momentum can be properly investigated

EXP	**T**	**Ω**	**ΔΩ**	ϵ	**Bu**
UP 1	50	0.126	$+\Omega/12$	0.08	0.26
DW 1	50	0.126	$-\Omega/12$	0.08	0.26
UP 2	50	0.126	$+\Omega/6$	0.17	0.26
DW 2	50	0.126	$-\Omega/6$	0.17	0.26
UP 3	200	0.031	$+\Omega/3$	0.32	4.34
DW 3	200	0.031	$-\Omega/3$	0.32	4.34

Tab. 4.2: List of performed experimental runs. T is the final (reference) rotation period of the tank [s], Ω is the final rotation rate of the tank [$rad\ s^{-1}$], $\Delta\Omega$ is the change in rotation rate of the tank, ϵ and Bu are the Rossby and Burger numbers [−].

The experimental runs and the relevant parameters are summarized in Table 4.2. Note that the changes in the angular velocity of the tank were chosen as to keep constant in the experiments the interior azimuthal velocity ($u_\theta \simeq 5.5\, cm\, s^{-1}$ at $r = 550\, cm$, just after the start of the run), and have only one pair (UP/DW 2) characterized by a double value of the azimuthal velocity. Finally, a Rossby number, $\epsilon \equiv \Delta\Omega/\Omega$, versus Burger number, $Bu \equiv (NH/\Omega L)^2$, diagram is plotted in Fig. 4.2.

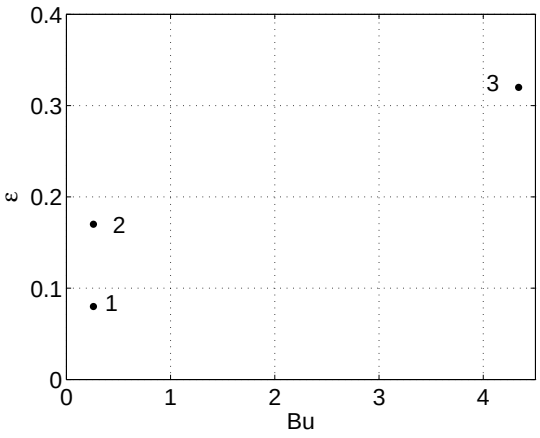

Fig. 4.2: Location of the different experiments in Rossby number (ϵ) versus Burger number (Bu) space.

4.2 Apparatus and Procedure

The spin-up and spin-down run pairs were performed in the large cylindrical rotating tank (Fig. 4.3), 13 m diameter, of the Coriolis-LEGI laboratory. There was no rigid boundary

Fig. 4.3: The Coriolis turntable

at the top of the tank, and it was covered with a floating foam canopy, removed before each run, in order to avoid spurious perturbations caused by shear stresses exerted by the air on the fluid surface during the filling.

The fluid was seeded with neutrally buoyant, light-scattering particles as to use P.I.V. system. Two laser beams (6 W continuous argon lasers) generated as many laser sheets: a horizontal one, 2.5 $m \times 2.5$ m, and a vertical one, 0.6 $m \times 0.6$ m, as sketched in Fig. 4.4 and 4.5. The horizontal laser sheet could scan seven different vertical positions in the bulk of the

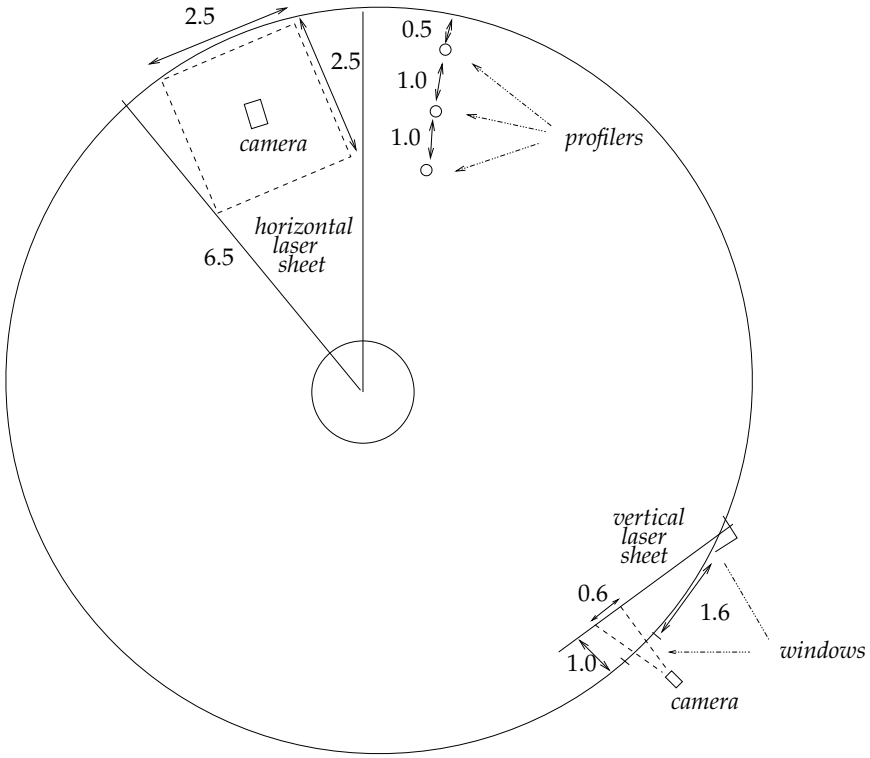

Fig. 4.4: Experimental set-up, top view. The inner cylinder contains the laser used to produce the horizontal laser sheet. The lengths are expressed in [m]

fluid by means of a laser sheet scanning system (Fig. 4.6(a)). Referring to Fig. 4.6(b), the laser beam arrives from the top by optical fibers on a small oscillating mirror (model 6850 of Cambridge Technology) which generates a vertical laser sheet. This small optical assembly moves horizontally on a linear bearing traverse, and the vertical laser sheet is deviated into a horizontal laser sheet by a 45° mirror. In this way, horizontal motion of the optical assembly translates directly into vertical motion of the horizontal laser sheet. A fixed laser sheet in the vertical plane was rather generated by means of a cylindrical lens.

The flow evolution was monitored for at least 100 rotation periods and images were taken

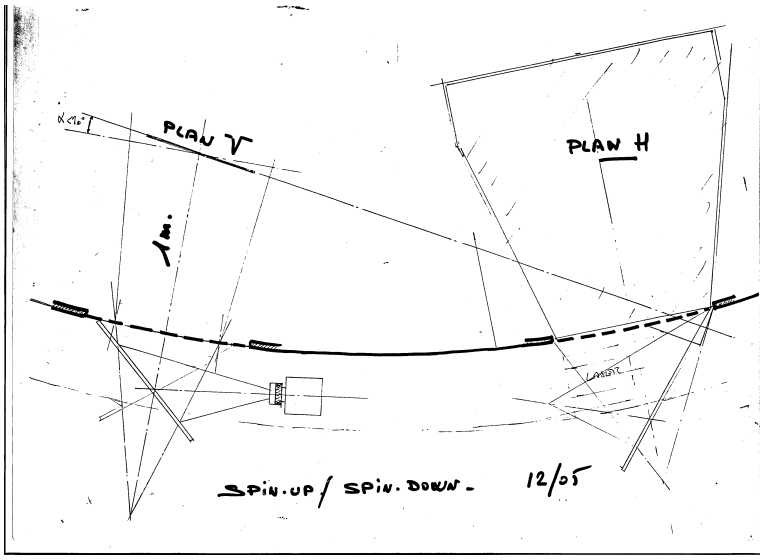

(a) Experimental set-up, draft by Dr. H. Didelle

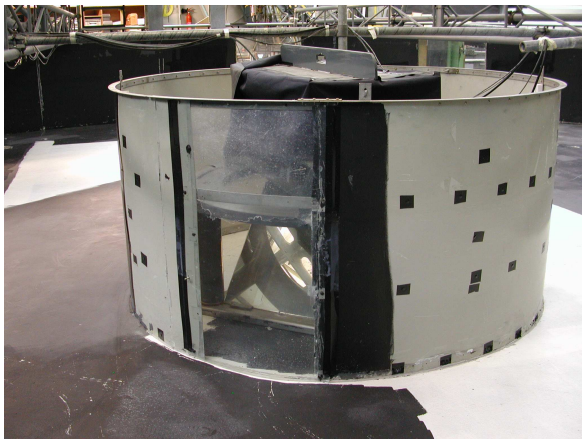

(b) horizontal laser sheet set-up

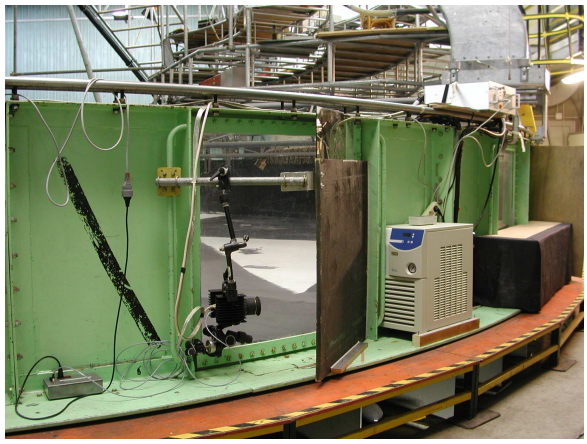

(c) vertical camera set-up

(d) horizontal laser sheet

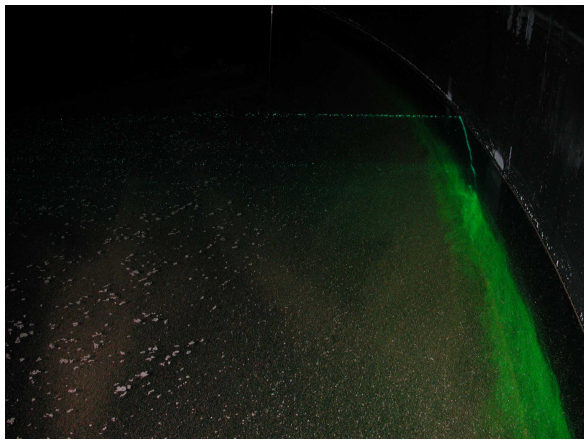

(e) horizontal laser sheet

Fig. 4.5: Experimental set-up: draft and photos

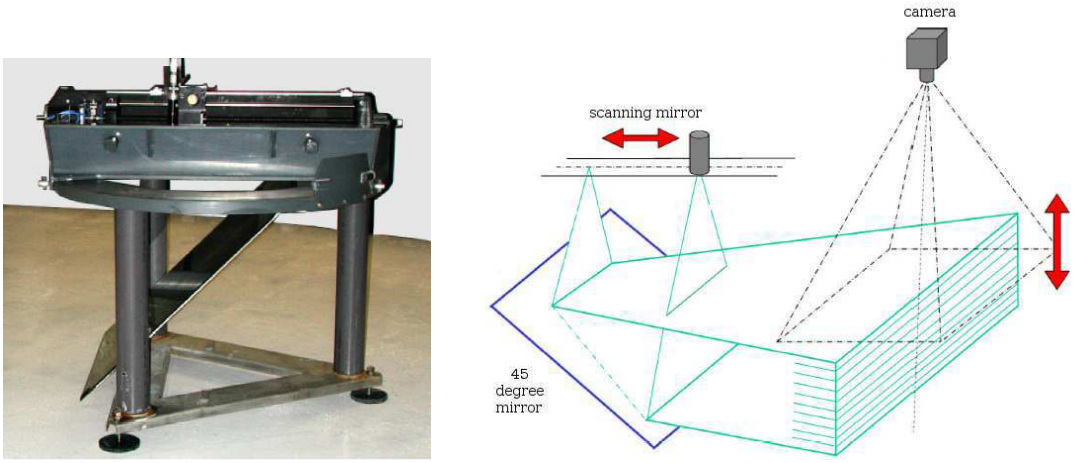

(a) apparatus (b) sketch

Fig. 4.6: Laser sheet scanning system.

by two digital CCD cameras with spatial resolution 1024 pixels × 1024 pixels. Each velocity field was obtained from a burst of four images by means of P.I.V. technique. Such bursts were repeated every 5 s at each horizontal level providing a measurement periodicity at a given height of 35 s. For the fixed vertical laser sheet the measurement periodicity was of 15 s.

4.3 Experimental Set-up

The tank was filled with salt-stratified fluid at approximatively 20°C ($\nu = 0.01\ cm^2\ s^{-1}$) while rotating at the desired rate. The parameter that most conveniently characterizes the initial stable stratification is the buoyancy frequency, $N \simeq 0.7\ s^{-1}$. The background stratification was kept constant, consequently the variation of the Burger number was accomplished only by modifying the rotational rate of the tank. The boundaries were impermeable to the solute, i.e., using the thermal analogy, the boundaries were *insulated*. The total depth of the fluid layer at rest, $H_0 = 60\ cm$, was kept fixed in all the experimental runs. Since the tank was rotating while filling, the fluid was displaced toward the periphery, until the resulting inward pressure gradient prevented any further displacement. Equilibrium then requires that at any point on the free surface the downward gravitational force and the outward centrifugal force combine into a resultant force normal to the free surface. Anyway, the vertical displacements are rather small and the difference in fluid height between the sidewall and the center of the tank can be computed by means of Eq.n (A.8) in Appendix A. For instance,

in case of a rotation period such as $T_i = 50\ s$ ($\Omega_i = 0.126\ rad\ s^{-1}$) it gives

$$H(R) - H_0 = \frac{\Omega_i^2 R^2}{4g} \simeq 1,7\ cm$$

being $H(R)$ the depth of the fluid layer at sidewall ($r = R$). Consequently, the Froude number was relatively small in our runs, and this effect is neglected. The total depth of the fluid layer is therefore considered independent of the radius (i.e., $H = H_0 = 60\ cm$).

Linear Stratification

The stratified fluid was prepared by a technique based on the *slip-under method* used by Fortuin (1960) [25] in the preparation of density gradient columns. Considering Fig. 4.7, a

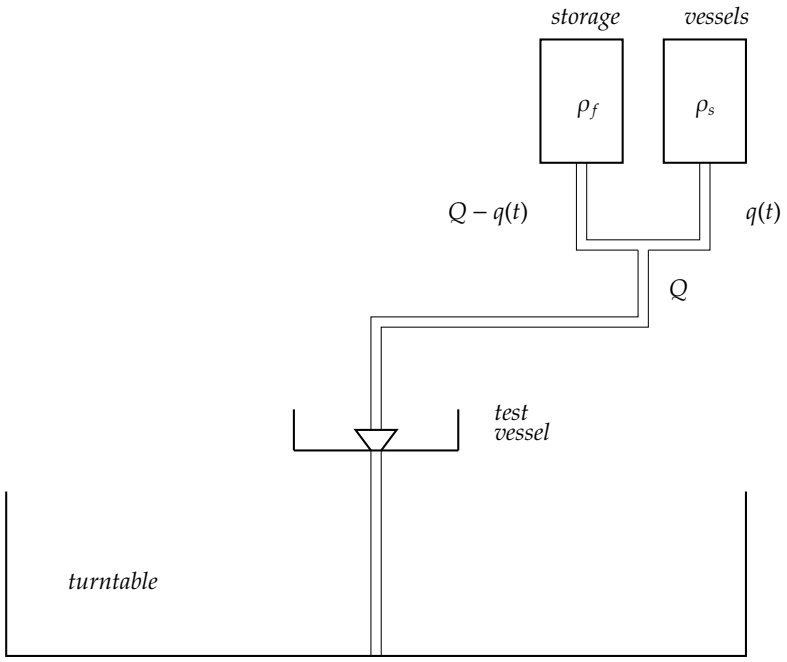

Fig. 4.7: sketch of the filling experimental apparatus

tube is connected to two vessels located in the laboratory frame of reference, one with fresh water and the other with salt water (NaCl) of desired density. As light fluid is pumped at a rate $Q - q(t)$ from the fresh water vessel in the tube, dense fluid from the salt water vessel flows at a rate $q(t)$ through the tube. The salt water flow rate $q(t)$, initially zero, is a linear increasing function of time, and is obtained by means of a computer-controlled volumetric pump. The mixed fluid is pumped at a flow rate Q in a rotating test vessel, located above

the turntable. The total flow rate Q is maintained constant using an ultrasonic sensor which records the fill level of the test vessel. This procedure increases the salt concentration of the fluid, initially fresh water, and in turn its density. Then, the fluid feeds into the turntable through a hole in the bottom edge by means of a filling tube passing down along the rotation axis. The incoming denser fluid displaces the lighter fluid introduced previously. In this way, a linear density gradient is obtained, which depends on the rate of flow from the storage vessels.

Since $\mathrm{d}V = Q\ \mathrm{d}t$ and

$$\begin{aligned} \mathrm{d}m &= (Q-q)\ \rho_f\ \mathrm{d}t + q\ \rho_s\ \mathrm{d}t \\ &= q\ \Delta\rho\ \mathrm{d}t + Q\ \rho_f\ \mathrm{d}t \end{aligned}$$

being ρ_f and ρ_s the density of fresh and salt water, respectively, then the final density is

$$\rho \equiv \frac{\mathrm{d}m}{\mathrm{d}V} = \rho_f + \frac{q}{Q}\Delta\rho$$

The rate of salt fluid flow is imposed linear in time by varying the rotation velocity of the volumetric pump. Therefore

$$\rho(t) = \rho_f + \frac{\alpha}{Q}\ \Delta\rho\ t$$

being α a constant. Finally, the temporal profile of density in the test vessel must be converted to the vertical profile of density in the turntable. In other words, it is possible to make a change of variable since the fluid leaving the test vessel at some time ends up at some particular elevation in the turntable

$$\rho(z) = \rho_f + \frac{\Delta\rho}{H}\ z \tag{4.1}$$

The stratification was characterized by the gradient $\Delta\rho/\rho_0 \simeq 3 \cdot 10^{-2}$ and the temperature of the water is stabilized and controlled with precision better than $1°C$, so that density variations associated with temperature fluctuations are negligible.

4.4 Measurement Technique

4.4.1 P.I.V. & C.I.V.

In order to measure velocities and related properties in our experiments we used the Particle Image Velocimetry (P.I.V.) system. The fluid is seeded with light scattering particles, assumed to faithfully follow the flow dynamics, and the motion of these particles is used to calculate velocity information. A laser beam is formed to a light sheet of a few *mm* thick and the fluid is illuminated. The light scattered by the particles is recorded as series of images by means of a CCD camera. The projection of the fluid velocity in the laser sheet plane is obtained through evaluation of the particle displacement between the images. This procedure is illustrated in Fig. 4.8.

The method used to obtain the displacement field proportional to the velocity field is the Correlation Imaging Velocimetry (C.I.V.), developed by Fincham & Spedding (1997) [22] and Fincham & Delerce (2000) [21]. This technique relies on the cross-correlation (covariance) of the luminous intensity between image pairs, limited to small subdomains (boxes). The velocity vector on each box is determined as the displacement which maximizes the covariance, multiplied by the time between the images. A detailed description of the procedure is illustrated in Appendix B.

Particles

The particles must be sufficiently bright to provide contrasted patterns, and small enough to minimize inertia and sedimentation effects, as well as laser beam absorbtion. We used expandable polystyrene particles of 350 μm (NOVA Chemicals Gedexcel ®), which can be adjusted in density. In fact, these particles swell by heating in water at $70 - 80\ ^{\circ}C$ due to the formation of small pentane gas bubbles, decreasing randomly the density by a few percent from its initial value of 1.05 $g\ cm^{-3}$. After this heating, the particles are sorted by density in order to have a flat distribution of densities matching that of the salt-stratified working fluid, i.e., $1.00 \leq \rho \leq 1.03\ g\ cm^{-3}$. This procedure ensures that an equal number of particles is present at each depth. Note that a non-ionic wetting agent (ILFORD ILFOTOL) is mixed with water to favor the wetting of particles and avoid agglomeration.

The seeding with particles must be dense, typically a density of $d_p \simeq 0.04$ particles per pixel in the images is needed to allow good statistic for correlation. For a field of 1000×1000 pixels, we need therefore $N_l = 4 \cdot 10^4$ particles illuminated by the laser sheet. If

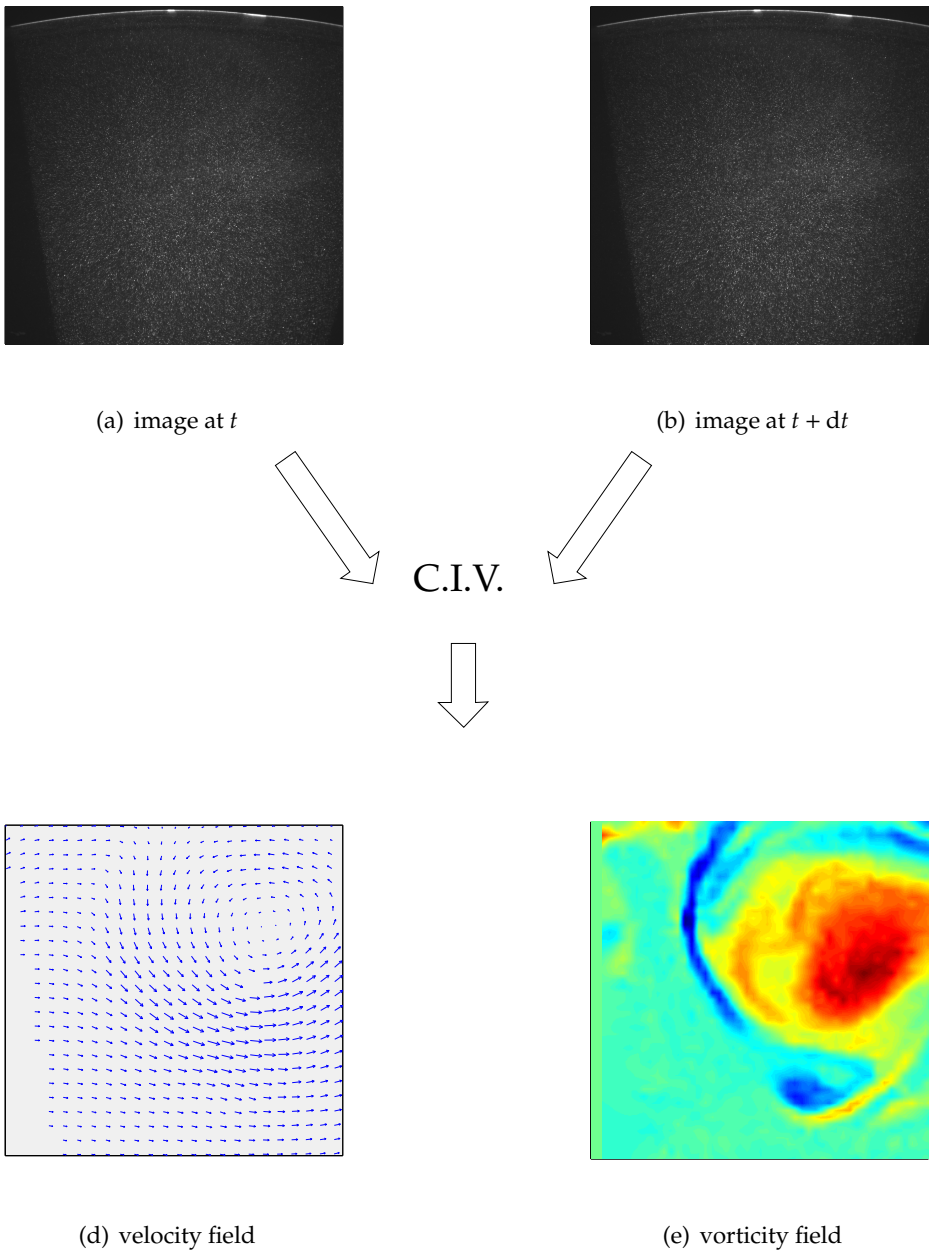

(a) image at t (b) image at $t + \mathrm{d}t$

(d) velocity field (e) vorticity field

Fig. 4.8: Correlation Image Velocimetry: the velocity field is obtained from the cross-correlation between the particle images at time t and at time $t + \mathrm{d}t$. The vorticity field is deduced by differentiation.

the corresponding volume of the laser sheet is V_l, the density of particles in the fluid is

$$n = \frac{N_l}{V_l} = \frac{N_t}{V_t} \tag{4.2}$$

being N_t and V_t, respectively, the total number of particles in the fluid and the volume of the fluid in the tank. The total volume of particles, V, to be seeded in the tank can be obtained by setting in Eq.n (4.2) $V = N_t V_p$, being V_p the volume of a single particle, i.e.,

$$V = \frac{V_t}{V_l} V_p N_l$$

4.4.2 Data acquisition

The image acquisition and the laser sheet displacement are controlled by the software ACQUIX, developed by Dr. G. Delerce. Since two computers were used for data acquisition, it was not necessary that the two cameras worked in synchronous. The cameras used were two DALSA, one with objective SCHNEIDER (focal length 25 *mm* and relative aperture 1) and the other with objective SIGMA (focal length 20 *mm* and relative aperture 1.8). The former was used for the horizontal laser sheet (shutter speed $\tau_{hs} = 1/15\ s$) and the latter for the vertical laser sheet (shutter speed $\tau_{vs} = 1/30\ s$). The frame periods between the images of each burst were not uniform in order to allow a best choice of time interval for the image cross-correlation. The acquisition provided a series of bursts for each experimental run, whose parameters are illustrated in the following sections.

UP/DW 1

(a) horizontal laser sheet (b) vertical laser sheet

Fig. 4.9: Time intervals between consecutive images expressed in units of shutter speed.

The frame periods for each burst are sketched in Fig. 4.9, providing a comparison between images with different time intervals, as sketched in Tab. 4.3.

UP/DW 2

The frame periods for each burst are sketched in Fig. 4.10, providing a comparison between images with different time intervals, as sketched in Tab. 4.4.

time intervals				
	horizontal		vertical	
image pairs	[unit of τ_{hs}]	[s]	[unit of τ_{vs}]	[s]
2 – 3	7	0.466	4	0.133
3 – 4	10	0.666	6	0.200
2 – 4	17	1.133	10	0.333
1 – 2	26	1.733	13	0.433
1 – 3	33	2.200	17	0.566
1 – 4	43	2.866	23	0.766

Tab. 4.3: Frame periods for the bursts of the runs UP/DW 1.

(a) horizontal laser sheet (b) vertical laser sheet

Fig. 4.10: Time intervals between consecutive images expressed in units of shutter speed.

time intervals				
	horizontal		vertical	
image pairs	[unit of τ_{hs}]	[s]	[unit of τ_{vs}]	[s]
2 – 3	4	0.266	2	0.066
3 – 4	10	0.660	6	0.200
2 – 4	14	0.933	8	0.266
1 – 2	26	1.733	13	0.433
1 – 3	30	2.000	15	0.500
1 – 4	40	2.666	21	0.700

Tab. 4.4: Frame periods for the bursts of the runs UP/DW 2.

UP/DW 3

The frame periods were the same of the experimental runs **UP/DW 2**.

Multilevel analysis

LEV	**vertical positions** h [cm]					
	UP 1	DW 1	UP 2	DW 2	UP 3	DW 3
1	0	0	0	0	0	0
2	4	5	5	5	5.5	5.5
3	9	10	10	10	11	11
4	14	16	16	16	15.5	15.5
5	20	23	23	23	21.5	22
6	27.5	30.5	30.5	30.5	28	28.5
7	37	35.5	39.5	39.5	34	34

Tab. 4.5: Vertical positions of the horizontal laser sheet

The horizontal laser sheet could scan seven different vertical levels in the bulk of the fluid, and one burst was made at each position every 5 s. The vertical positions of the horizontal laser sheet are summarized in Tab. 4.5, being h the depth from the free surface.

4.4.3 Calibration Procedure

To get actual velocity data, it is first necessary to calibrate the images, transforming pixel displacements into real distances, using some reference object. The objective is to find the external (position and orientation relatively to a world coordinate system), and the internal parameters of the camera (principal point or image center, focal length and distortion coefficients).

Tsai's model for camera calibration

The camera calibration technique used at Coriolis laboratory is the one proposed by Tsai (1986) [73], retained for its accuracy and simplicity. Its implementation needs corresponding $3D$ point coordinates and $2D$ pixels in the images. It uses a two-stage algorithm, computing the position and orientation in first stage and the internal parameters of the camera in second stage. Note that the real power of this technique is felt in Stereoscopic P.I.V., but it is even used in the traditional P.I.V. technique in order to standardize the calibration procedure.

Experimental set-up

The calibration process should be performed very carefully to get sufficient measurement precision. It is necessary to know exactly the position of the calibration target, its distance from the bottom or any fixed element, and its angles with vertical and horizontal axis.

The procedure at Coriolis laboratory uses a calibration target with a grid of markers placed in the acquisition area inside the laser sheet in the final experimental configuration. One image of the target must be recorded and the image marker locations are found by means of the software ACQUIX, developed by Dr. G. Delerce.

4.5 Velocity Fields

The velocity fields and their spatial derivatives, as well as information about the C.I.V. processing, were stored in NetCDF [1] file format. The cameras co-rotate with the tank, and thus the frame of reference rotating with the final angular velocity of the tank is considered. The software UVMAT, based on MATLAB graphic user interfaces and developed by Dr. J. Sommeria, was used to analyze images and velocity fields. It is also a powerful toolbox for post-processing since it is designed to easily include new functions written by the user in standard computer languages.

The main difference between spin-up and spin-down runs concerns the direction of the relative flow in the interior region. Since the rotating direction of the tank is anticlockwise, the change in the rotation rate generates a clockwise (anticyclonic) and an anticlockwise (cyclonic) relative flow, respectively, in spin-up and in spin-down. Assuming the azimuthal axis orientation anticlockwise, then the azimuthal velocity field is negative in spin-up and positive in spin-down. In order to compare spin-up and spin-down velocity fields, let us reverse the azimuthal spin-up velocity field.

As to compare different runs, the velocity of the flow at a given radial position was scaled with the azimuthal velocity just after the start of the run at the same radial position, i.e., $U^i(r) \equiv u^i_\theta = |\Delta\Omega^i r|$ where the i-apex variable indicates the run considered. Therefore, the range of the non-dimensional azimuthal velocity field is $0 \leq u'^i_\theta \leq 1$ for all the runs.

[1] Network Common Data Form is a machine-independent format for representing scientific data, suitable for large arrays. Each piece of data can be directly accessed by its name without reading the whole file. New records can be added to the file without perturbing the remaining information

The procedure to convert cartesian velocity fields in polar coordinates is illustrated in the following steps. Note that, in order to avoid long expressions, horizontal and vertical velocity fields are indicated, respectively, as TOP and SIDE VIEW data.

Referring to Fig. 4.11, let O be the center of the tank and $\vec{r}$ the vector position. The local cartesian and polar frames of reference are respectively $(\hat{i}_x, \hat{i}_y)$ and $(\hat{i}_r, \hat{i}_\theta)$.

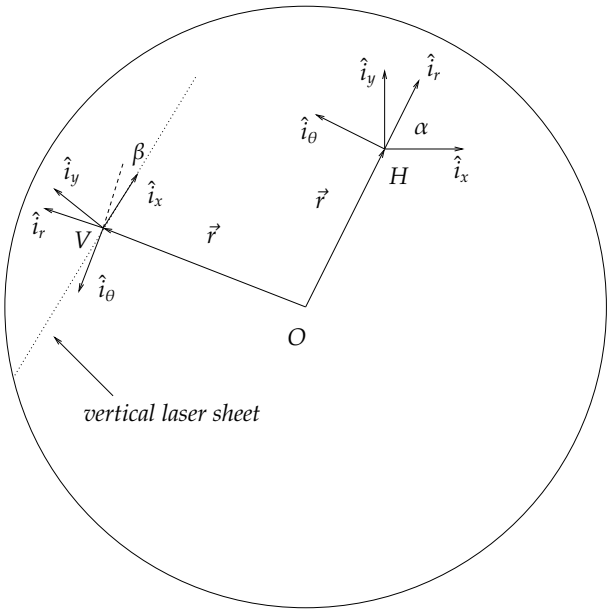

Fig. 4.11: Relation between local cartesian and polar frames of reference

TOP VIEW Data

Let us consider a point H on the horizontal laser sheet and let α be the angle between the two local frames of reference. The relation between cartesian (u_x, u_y) and polar velocity components (u_r, u_θ) can be found by expressing the cartesian in function of the polar axis

$$\hat{i}_x = \cos\alpha\hat{i}_r - \sin\alpha\hat{i}_\theta \tag{4.3a}$$

$$\hat{i}_y = \sin\alpha\hat{i}_r + \cos\alpha\hat{i}_\theta \tag{4.3b}$$

Since

$$\vec{u} = u_x\hat{i}_x + u_y\hat{i}_y \tag{4.4a}$$

$$\vec{u} = u_r\hat{i}_r + u_\theta\hat{i}_\theta \tag{4.4b}$$

using Eq.ns (4.3) in Eq.n (4.4a) and comparing with Eq.n (4.4b), it is straightforward to obtain

$$\begin{aligned} u_r &= u_x \cos\alpha + u_y \sin\alpha \\ u_\theta &= -u_x \sin\alpha + u_y \cos\alpha \end{aligned}$$

SIDE VIEW Data

Let us consider a point V on the vertical laser sheet and let β be the angle between the two local frames of reference. The sought relation may be found by following an analogous procedure

$$u_r = -u_x \sin\beta + u_y \cos\beta \tag{4.5a}$$

$$u_\theta = -u_x \cos\beta - u_y \sin\beta \tag{4.5b}$$

Assuming that, generally, the radial velocity is negligible (Fig. 4.12), then Eq.ns (4.5) reduce

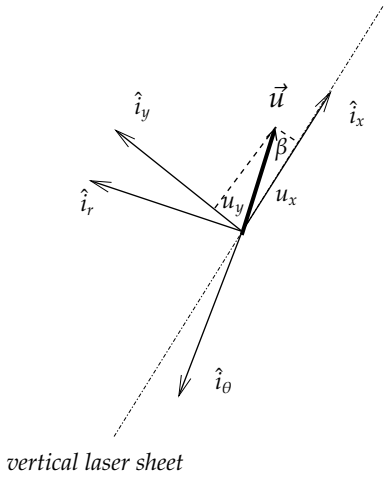

Fig. 4.12: Local cartesian and polar component of the velocity field. Assuming that, generally, the radial velocity is negligible, then the horizontal velocity may be considered along the azimuthal direction.

to

$$\begin{aligned} u_r &\simeq 0 \\ u_\theta &\simeq -\frac{u_x}{\cos\beta} \end{aligned}$$

4.5.1 Consistency test

Since TOP and SIDE VIEW data concern the same experimental runs, it is necessary to check the consistency between them. Fig. 4.13 shows a comparison of the non-dimensional

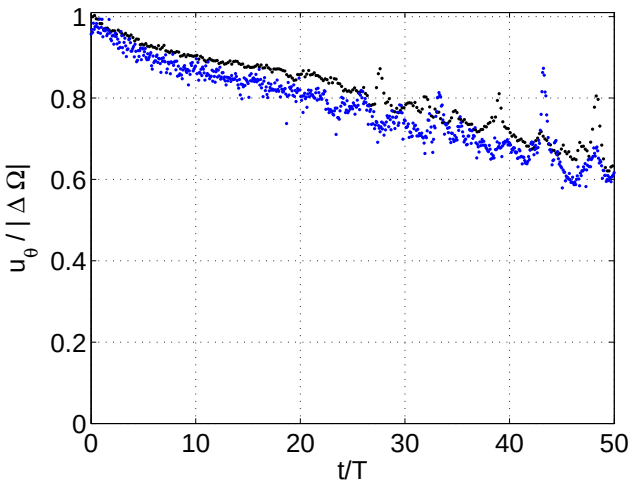

Fig. 4.13: UP 3 ($\{\epsilon, Bu\} = \{0.32, 4.34\}$) - non-dimensional azimuthal velocity [−] - temporal evolution: —●— TOP data; —●— SIDE data

azimuthal velocity versus time (scaled by the tank rotation period). The temporal decay of the azimuthal velocity represents the adjustment mechanism to the new angular velocity of the container (i.e., the system approaches a state of relative rest). The TOP VIEW data concern a stripe-average at fixed radial position, while the SIDE VIEW data involve a stripe-average at fixed vertical location. Hereinafter, if not otherwise indicated, the velocity fields will be spatially averaged in this way. In case of Fig. 4.13, the horizontal stripe is located at the radial position, $r = 550\ cm \rightarrow r' = r/R \simeq 0.85$, corresponding approximatively to the location of the vertical laser sheet, while the stripe height, $z = 24\ cm \rightarrow z' = z/H \simeq 0.4$, is the same of the vertical location considered for the horizontal laser sheet (the seventh level).

Fig. 4.13 shows that, generally, the SIDE VIEW data are below the TOP VIEW data. We believe that this is due to the fact that the horizontal laser sheet assumes a convex upward configuration, therefore accomplishing a small overestimation of the velocity field. However, TOP and SIDE data agree to within a few per cent, establishing the accuracy of the measurements, and from this point we proceed to use both data, according to our requirements.

4.5.2 Grids

Considering a velocity field, each velocity vector is applied on a grid point. By default, a cartesian grid is considered, but the visualization of a polar velocity field on a cartesian grid

may be misleading (Fig. 4.14(a)). Therefore, we applied the polar velocity vectors on a polar grid (Fig. 4.14(b)).

In order to facilitate the visualization of the velocity field, the azimuthal variable was multiplied by a scalar factor corresponding to the radius of the turntable (i.e., $R = 650$)

$$\theta = R\theta_r \tag{4.6}$$

being θ_r the real azimuthal variable. Since the values along the azimuthal axis are not the physical ones, they will be omitted on the graphs when not necessary.

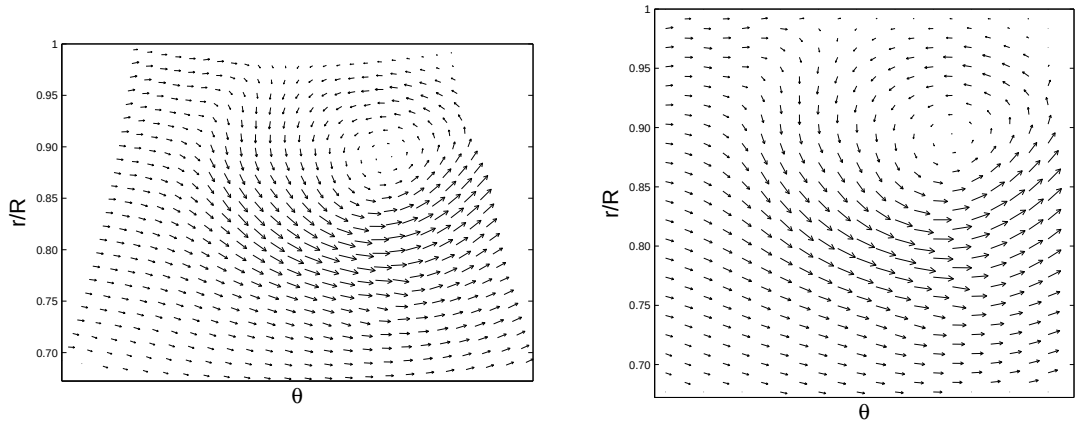

(a) cartesian grid (b) polar grid

Fig. 4.14: Example of polar velocity field in different grids

Chapter 5

Preliminary Analysis

In ¶ 4.1, dimensional analysis has indicated that the flow evolution of our experimental runs depends only on the Burger and Rossby numbers. Previous experimental works (¶ 3.3) have shown that the incremental spin-up (spin-down) process is not affected by the Rossby number in the range $\epsilon \leq 0.22$. Consequently, we expect that a preeminent role will be played by the Burger number, which measures the relative importance of stratification and rotation.

The value of the Burger number controls the penetration of the secondary circulation in the interior region (cf., Eq.n 3.16), and therefore the vertical profile of the azimuthal velocity. Moreover, a low Burger number means large horizontal length scale and small Rossby radius of deformation, suggesting that baroclinic instability might develop.

It has been long understood (Briley & Walls (1971) [5]) that spin-down is significantly different from spin-up even in linear regime. In fact, the fluid particles near the cylindrical sidewall may rapidly experience a centrifugal instability for impulsive spin-down.

5.1 Influence of the Rossby Number

TOP VIEW Data

In order to check the influence of the Rossby number let us consider the runs UP 1 ($\{\epsilon, Bu\} = \{0.08, 0.26\}$) and UP 2 ($\{\epsilon, Bu\} = \{0.17, 0.26\}$) for which the Burger number is fixed. The non-dimensional azimuthal velocity versus time at $\{r/R, z/H\} \simeq \{0.80, 0.75\}$ (Fig. 5.1) shows that the basic decay trend is similar for the two runs, and the discrepancies concern only the oscillations superimposed to the basic flow. Nevertheless, some velocity fluctuations are nearly coincident (cf., Fig. 5.1(a)) suggesting that the general properties of the associated

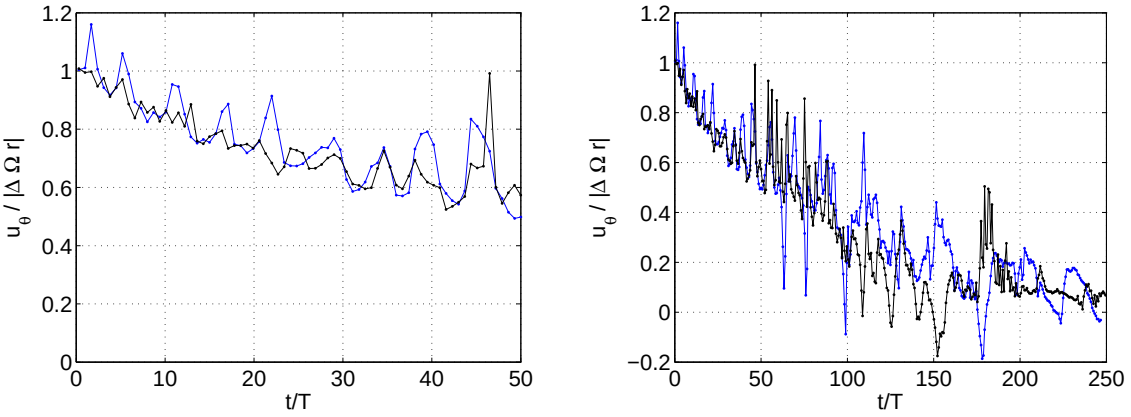

(a) short time (b) long time

Fig. 5.1: TOP VIEW - $\{r/R, z/H\} \simeq \{0.80, 0.75\}$ UP 1 —●— vs UP 2 —●— - non-dimensional azimuthal velocity [−] - temporal evolution

instability (e.g., the oscillation period) are unaltered.

Fig. 5.2 shows the azimuthal velocity decay at different radial positions for the runs

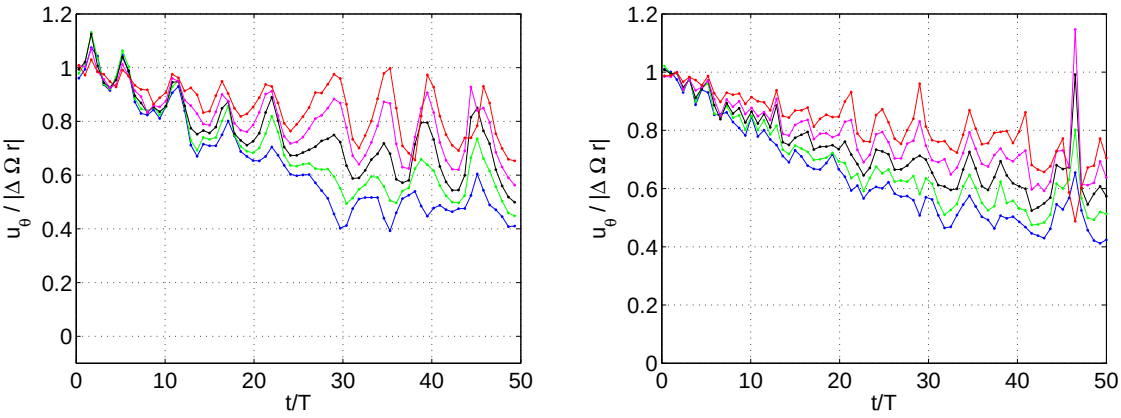

(a) UP 1 ($\{\epsilon, Bu\} = \{0.08, 0.26\}$) (b) UP 2 ($\{\epsilon, Bu\} = \{0.17, 0.26\}$)

Fig. 5.2: TOP VIEW - $z/H \simeq 0.75$ - non-dimensional azimuthal velocity [−] - temporal evolution at different radial positions: —● $r/R = 0.70$; —● $r/R = 0.75$; —● $r/R = 0.80$; —● $r/R = 0.85$; —● $r/R = 0.90$

considered. It appears that the velocity oscillations are almost radially uniform in both cases, but the run characterized by a smaller Rossby number (i.e., UP 1) presents a better coherence of the fluctuations. Although previous experimental works have shown that the flow behavior is not altered by a Rossby number $\epsilon \leq 0.22$, our analysis exhibits that this is

confirmed strictly for the dynamics of the spin process, i.e, the adjustment mechanism to the new angular velocity of the container, represented by the basic decay trend. In fact, a double of the Rossby number seems to affect the long-wave instability that might develop in the flow evolution. Since we are interested really in this flow instability, hereinafter we will leave out a deeper study of the effects of non-vanishing Rossby numbers.

5.2 Influence of the Burger Number

Let us consider what are the differences in the flow dynamics between runs characterized by small and large Burger numbers. Thereby, we consider the runs UP 1 ($\{\epsilon, Bu\} = \{0.08, 0.26\}$) and UP 3 ($\{\epsilon, Bu\} = \{0.32, 4.34\}$).

5.2.1 Evolution of the Vertical Shear

SIDE VIEW Data

In quasi-geostrophic regime a homogeneous flow in a container consists of two regions: an interior one where the flow dynamics is independent of depth, and boundary layers adjacent to rigid boundaries in which the velocity field adjusts to satisfy the no-slip condition. The effect of the change in the rotation rate of the tank is transmitted to the interior region by a vertical velocity $w' \sim O(E^{1/2})$ independent of the depth.

In a stably stratified fluid, the buoyancy force associated to the vertical density gradient tends to inhibit this motion. Consequently, for strong enough stratification, the Ekman layer does not play a significant role in the flow dynamics. The most outstanding effect of the stratification is evident in the vertical profiles of azimuthal velocity. Fig. 5.3 shows their temporal evolution in the runs considered, omitting the regions closer to tank bottom and free surface.

Just after the change in the rotation rate of the tank ($t/T = 0$) the fluid is approximatively characterized by solid body rotation at the imposed angular velocity ($u'_\theta \simeq 1$). As time elapses, the two runs show a different dynamics. In the run UP 3 (Fig. 5.3(a)), the azimuthal velocity develops in about 15 rotation periods a quasi-steady vertical shear in the interior region. This vertical shear reflects the velocity gradients created by the secondary circulation, and gives insight to the restriction of the spin-up of the fluid, due to the stable stratification.

In the run UP 1 (Fig. 5.3(b)), due to the deeper penetration of the secondary circulation, the vertical shear of the azimuthal velocity is notably smaller with respect to the run UP 3 in the

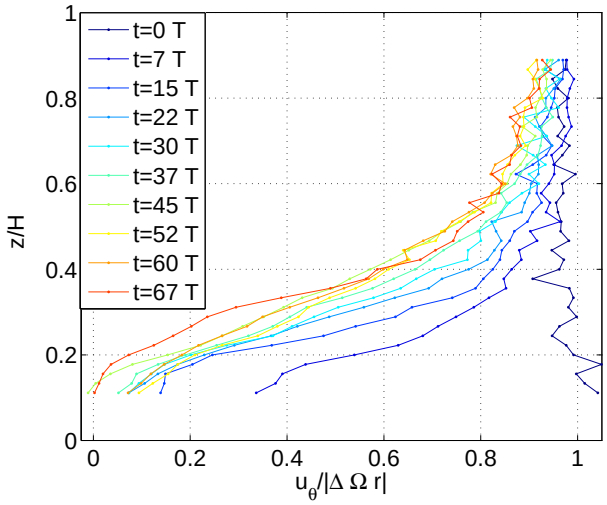

(a) UP 3 ($\{\epsilon, Bu\} = \{0.32, 4.34\}$)

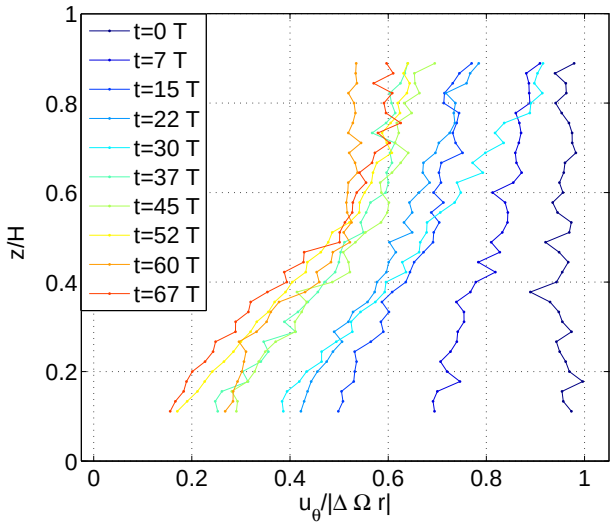

(b) UP 1 ($\{\epsilon, Bu\} = \{0.08, 0.26\}$)

Fig. 5.3: SIDE VIEW - non-dimensional azimuthal velocity [−] - vertical profile - temporal evolution

region $0.1 \leq z/H \leq 0.5$. The vertical shear is proportional to the horizontal density gradients by Eq.n (2.18), and this implies that the isopycnal surfaces are steeper in the run UP 3 than in the run UP 1 in this region. In the latter run, the configuration of the isopycnal surfaces is compatible with the presence of baroclinic instability according to Eq.n (2.29). Baroclinic instability acts to convert the available potential energy in kinetic energy of the perturbations, flattening out the isopycnal surfaces into a horizontal configuration, as evidenced by Fig.

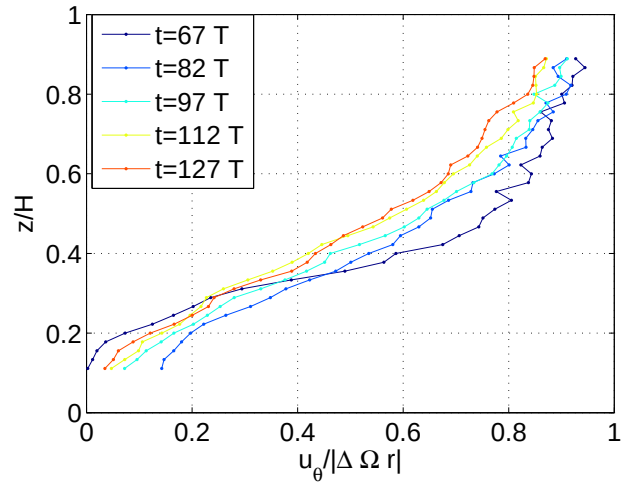

(a) UP 3 ($\{\epsilon, Bu\} = \{0.32, 4.34\}$)

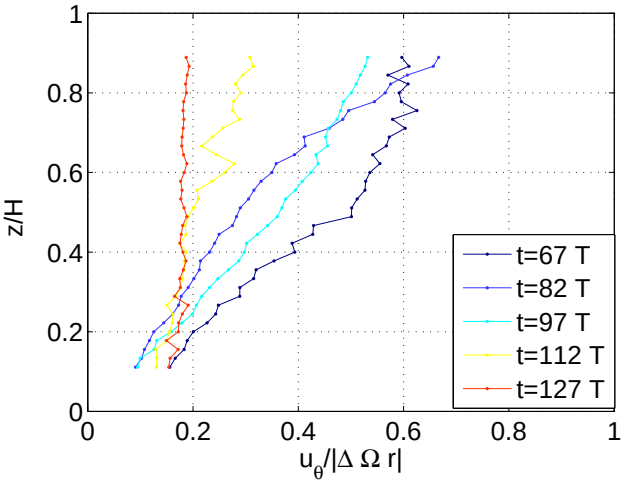

(b) UP 1 ($\{\epsilon, Bu\} = \{0.08, 0.26\}$)

Fig. 5.4: SIDE VIEW - non-dimensional azimuthal velocity [−] - vertical profile - temporal evolution

5.3(b).

The bottom Ekman layer is the region where the interior azimuthal velocity adjusts to the velocity of the bottom boundary, and this layer decays as the interior fluid gradually spins-up. The Ekman layer eventually vanishes when the secondary circulation is eliminated. Bearing in mind that $u'_\theta(z' = 0) = 0$, the vertical profile of the run UP 3 (Fig. 5.3(a)) develops in $t/T \sim 15$ a smaller vertical shear at the bottom than the profile of the run UP 1 (Fig.

5.3(b)). This even if the run UP 3 is characterized by a thicker Ekman layer [1] (smaller background rotation) than the run UP 1. These measurements suggest that the Ekman layer is significantly weakened in flow with dominating stratification (i.e., large Burger number), according to previous studies (e.g., Linden (1977) [45]).

The long time evolution of the vertical profile of the azimuthal velocity is shown in Fig. 5.4. In case of $Bu > O(1)$ (i.e., run UP 3 - Fig. 5.4(a)), the flow reaches a nearly uniform vertical shear (linear vertical profile) in the interior region after $t/T \sim 100$, showing a slow decrease of the azimuthal velocity. In case of $Bu < O(1)$ (i.e., run UP 1 - Fig. 5.4(b)), the flow shows a faster decrease of the azimuthal velocity in the upper half part of the fluid, suggesting that the baroclinic instability may increase the vertical transport of horizontal momentum, as stated by Smirnov *et al.* (2005) [68]. Moreover, the vertical shear of the flow in the interior decreases in time, and at $t/T = 127$ the azimuthal velocity is almost vertically uniform in the interior region, pointing that the fluid is returned in a state of minimum potential energy.

5.2.2 Decay of the Azimuthal Velocity

TOP VIEW Data

Fig. 5.5 shows a comparison between the runs UP 1 and UP 3 of the non-dimensional azimuthal velocity versus time at $z/H \simeq 0.75$ for different radial positions. Note that, since $T = 50\ s$ for UP 1 and $T = 200\ s$ for UP 3, by scaling the time with the tank rotation period T then the measurement frequency is four times greater in the run UP 3 than in the run UP 1.

The change in the angular velocity of the tank generates an anticyclonic current along the azimuthal direction, as shown in Fig. 5.6. In the run UP 3 ($\{\epsilon, Bu\} = \{0.32, 4.34\}$) the velocity field is characterized by circular streamlines oriented along the azimuthal direction. The axisymmetry of the flow is retained through the spin-up process, as shown in Fig. 5.7 [2], with some small eddies due to the horizontal shear of the current near the sidewall, as shown in Fig. 5.7(c). The effect of this behavior is evident in Fig. 5.5: the stability of the flow implies a slow velocity decay with fluctuations of the order of 10^{-2}. Fig. 5.9(a) shows the temporal evolution of the radial profile of the azimuthal velocity at $z/H \simeq 0.75$. The initial solid body velocity profile, established immediately after the change in the rotation rate of

[1] $\delta_e = E^{1/2}H = (\nu/\Omega)^{1/2}$

[2] The velocity vectors may be compared each others only inside each sub-image. In fact, as the the angular velocity of the fluid adjusts to that of the boundaries, an increase of the scale factor is necessary in order to properly visualize the flow.

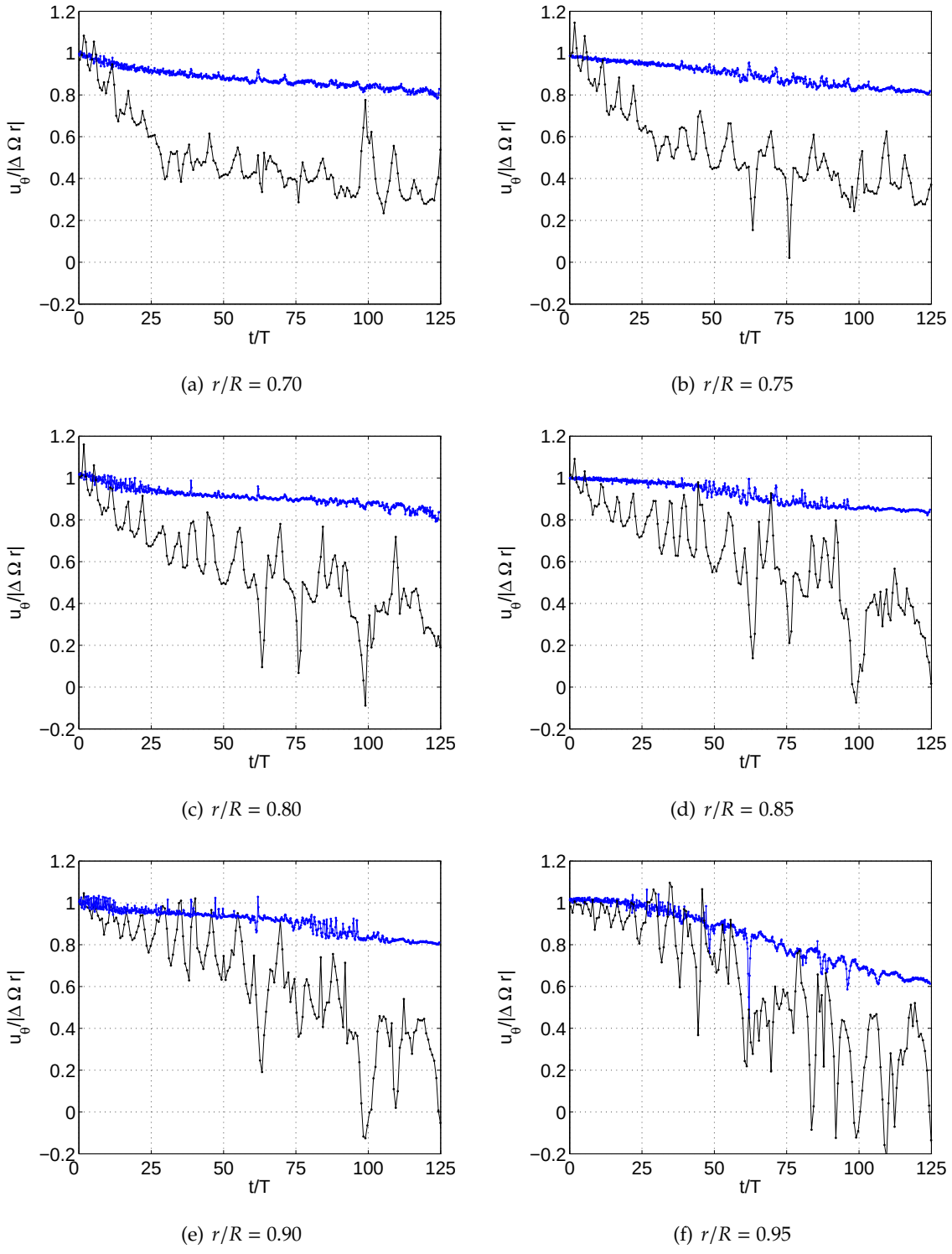

(a) $r/R = 0.70$ (b) $r/R = 0.75$

(c) $r/R = 0.80$ (d) $r/R = 0.85$

(e) $r/R = 0.90$ (f) $r/R = 0.95$

Fig. 5.5: TOP VIEW $z/H \simeq 0.75$ - non-dimensional azimuthal velocity [−] - temporal evolution at different radial positions: —●— UP 1 ($\{\epsilon, Bu\} = \{0.08, 0.26\}$); —●— UP 3 ($\{\epsilon, Bu\} = \{0.32, 4.34\}$)

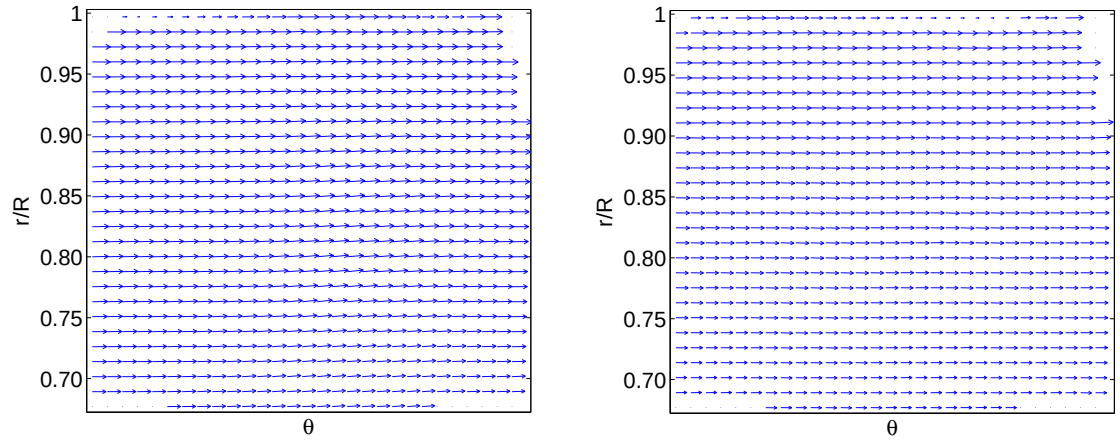

(a) UP 1 ($\{\epsilon, Bu\} = \{0.08, 0.26\}$) (b) UP 3 ($\{\epsilon, Bu\} = \{0.32, 4.34\}$)

Fig. 5.6: TOP VIEW lev 4 - velocity field - $t/T = 0$

the tank, transforms into a boundary layer profile. With time the influence of the sidewall drifts toward the center of the tank, extending to $r/R \sim 0.90$ after 120 rotation periods. Note that outside the sidewall boundary layer the azimuthal velocity decreases maintaining a solid body velocity profile in the interior region such as $z/H \simeq 0.75$.

In the run UP 1 ($\{\epsilon, Bu\} = \{0.08, 0.26\}$) the velocity field shows two different regimes: at the outset of the experiment just a relative small discrepancy is evident with respect to the previous case, and the streamlines preserve a circular shape, as shown in Fig.s 5.8(a) and 5.8(b). In the temporal evolution (Fig. 5.5) it corresponds to a series of growing oscillations, quite regular in period, superimposed to a faster decay with respect to the run UP 3. During the second stage, after about 50 rotation periods, a drastic change occurs in the flow development. The streamlines strain from circles into ellipses and non-axisymmetric disturbances appear in the velocity field, which can even lead to local reversal flow, as in Fig.s 5.8(d) and 5.8(f). The effect on the azimuthal velocity temporal evolution consists in wider and lesser regular oscillations, superimposed to a generally slower decay trend than the first stage, as shown in Fig. 5.5. The temporal evolution of the radial profile of the azimuthal velocity is more complex than in the run UP 3. Fig. 5.9(c) show that the azimuthal velocity decays generally faster at smaller radii during the first 50 rotation periods. Later in time, the non-axisymmetric disturbances perturb completely the radial profile of the azimuthal velocity.

The runs UP 1 and UP 3 are characterized by a different final rotation period, which implies different Burger numbers, and a different change in the rotation rate of the tank,

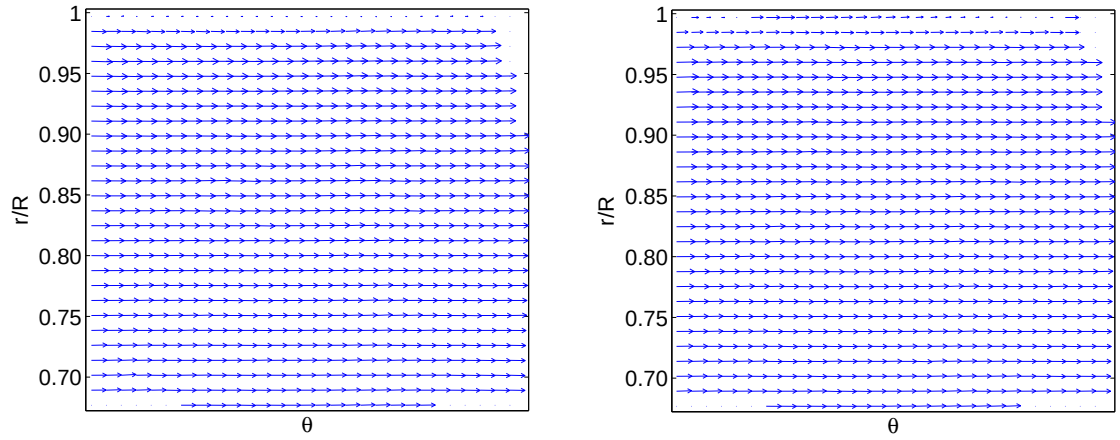

(a) $t/T = 24$

(b) $t/T = 43$

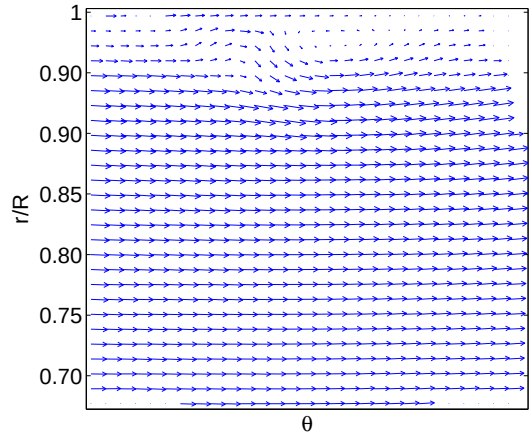

(c) $t/T = 62$

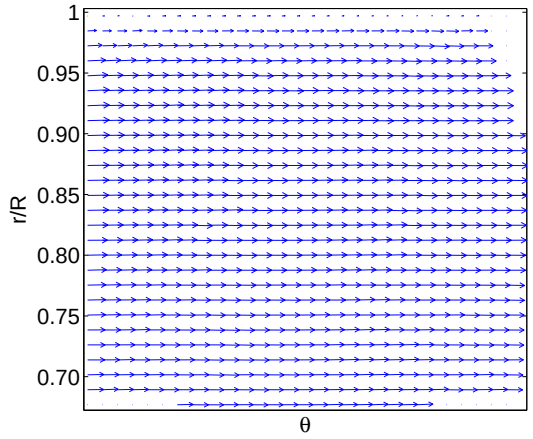

(d) $t/T = 84$

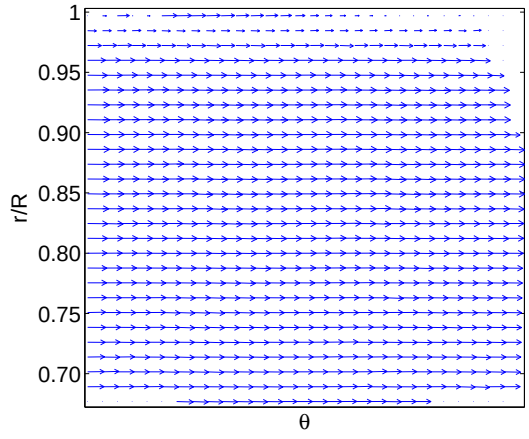

(e) $t/T = 97$

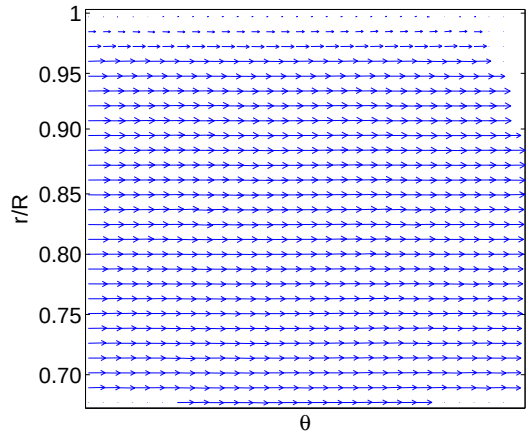

(f) $t/T = 109$

Fig. 5.7: TOP VIEW $z/H \simeq 0.75$ UP 1 ($\{\epsilon, Bu\} = \{0.08, 0.26\}$) - velocity field

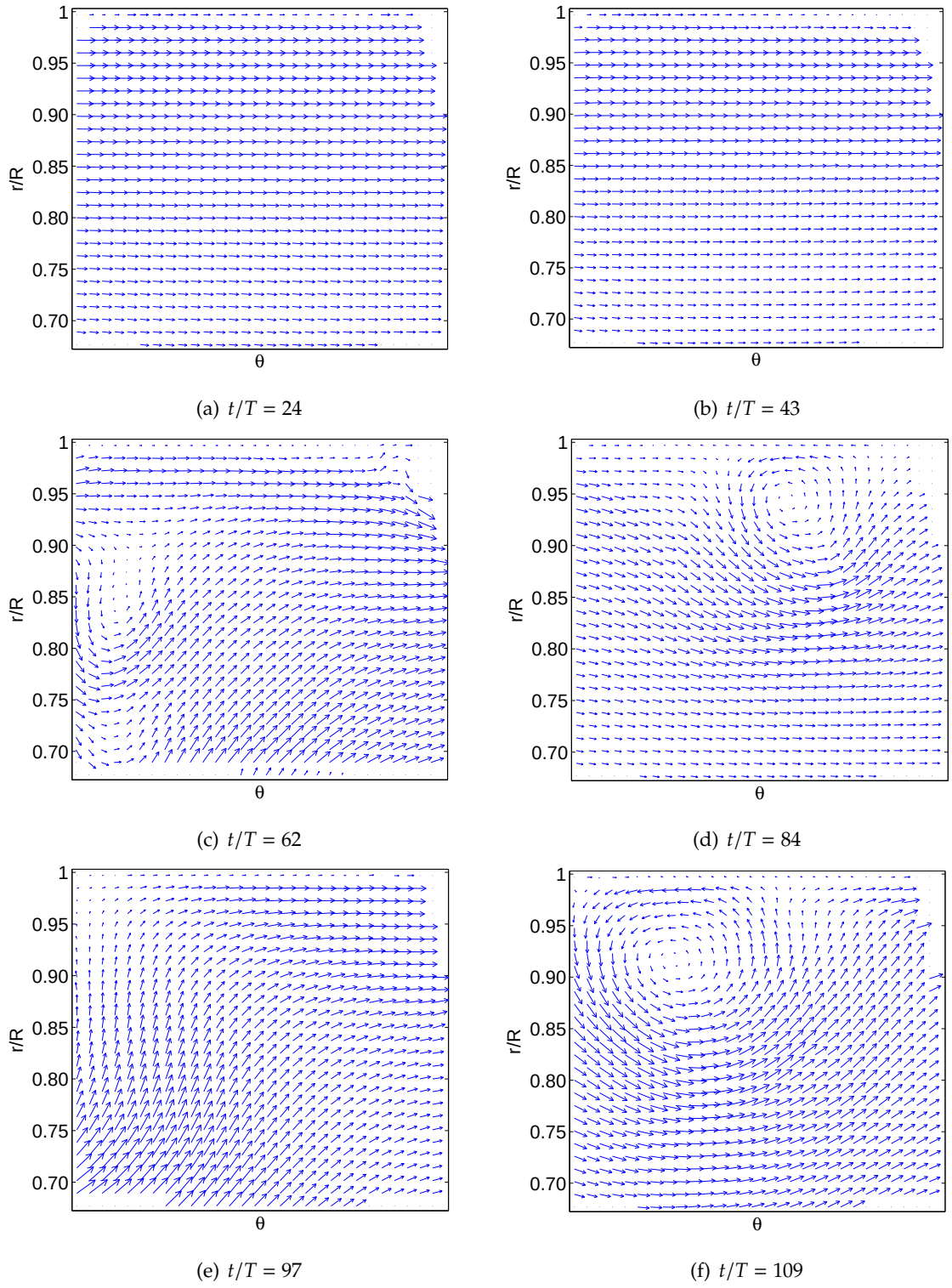

(a) $t/T = 24$ (b) $t/T = 43$

(c) $t/T = 62$ (d) $t/T = 84$

(e) $t/T = 97$ (f) $t/T = 109$

Fig. 5.8: TOP VIEW $z/H \simeq 0.75$ UP 3 ($\{\epsilon, Bu\} = \{0.32, 4.34\}$) - velocity field

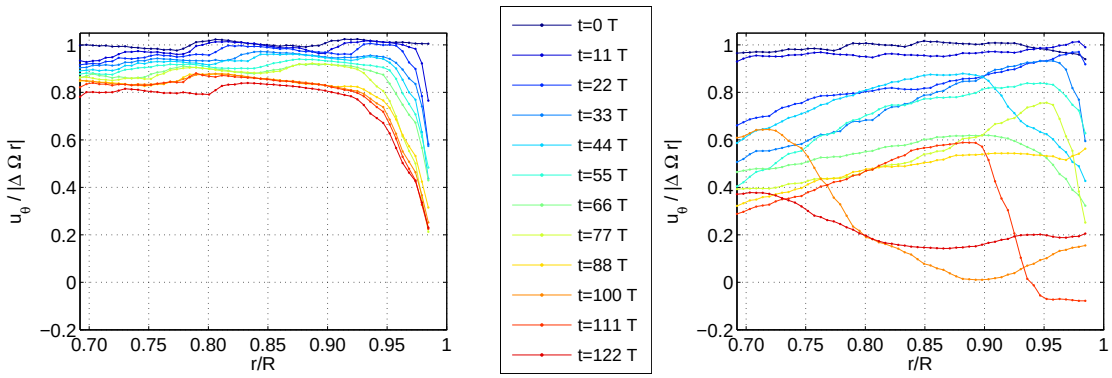

(a) UP 3 ($\{\epsilon, Bu\} = \{0.32, 4.34\}$) (b) legend (c) UP 1 ($\{\epsilon, Bu\} = \{0.08, 0.26\}$)

Fig. 5.9: TOP VIEW $z/H \simeq 0.75$ - non-dimensional azimuthal velocity [−] - radial profile temporal evolution

which means different Rossby numbers. Smirnov *et al.* (2005) [68] proposed that the formation of large-scale eddies depends on the relative values of Rossby and Burger numbers. More precisely, for sufficiently small ϵ at fixed Bu and for sufficiently large Bu at fixed ϵ the flow could be stabilized. The latter criterion seems to be in agreement with our results: the runs UP 1 ($\{\epsilon, Bu\} = \{0.08, 0.26\}$) appears to be baroclinically unstable, while the run UP 3 ($\{\epsilon, Bu\} = \{0.32, 4.34\}$) is baroclinically stable. In the run UP 3 the Rossby number was notably larger than in the run UP 1, however the flow could be made stable by setting the Burger number large enough.

The effects of the advective terms in the equations of motions were considered modest for $\epsilon \leq 0.22$, and it appears that even in case of larger Rossby number ($\epsilon = 0.32$) the nonlinearity does not seem to play a relevant role in the development of the axisymmetric flow. Therefore, we confirm that the discrepancies exhibited in the flow behavior between the runs UP 1 and UP 3 depends on the value of the Burger number. Recognizing that the decrease of the azimuthal velocity means that momentum is being transferred from the solid boundaries to the bulk of the fluid, the instability associated with $Bu < O(1)$ may contribute to enhance it. In fact, Smirnov *et al.* (2005) [68] reported that "the formation of large-scale eddies through the development of instabilities provides an additional mechanism for the transport of angular momentum", reducing the time of the spin-up process.

5.3 Spin-up vs Spin-down

Let us consider pairs of spin-up and spin-down runs characterized by the same Rossby and Burger numbers

run 1: $\{\epsilon, Bu\} = \{0.08, 0.26\}$ run 2: $\{\epsilon, Bu\} = \{0.17, 0.26\}$ run 3: $\{\epsilon, Bu\} = \{0.32, 4.34\}$

5.3.1 Decay of the Azimuthal Velocity

TOP VIEW Data

Fig. 5.10 shows a comparison of the non-dimensional azimuthal velocity versus time at $z/H \simeq 0.75$ for a radial distance relatively near to the sidewall ($r/R = 0.80$). During spin-down the fluid motion is perturbed by flow instabilities which originate at the sidewall, while it is always centrifugally stable in the case of spin-up. Fig.s 5.10(a) and 5.10(b) show that the velocity decay is faster in spin-down than in spin-up, since the effect of the centrifugal instabilities is to decelerate the fluid more rapidly by extracting energy from the mean flow. Note that in the run 3 ($\{\epsilon, Bu\} = \{0.32, 4.34\}$), characterized by baroclinically stable flow, the spin-down run shows a drastic decay around $t/T \simeq 25$ (Fig. 5.10(c)). Therefore, if a flow is locally centrifugally unstable, then the whole dynamics of the spin process might be modified.

Lopez (1996) [46] and Lopez & Weidman (1996) [47] found that in addition to centrifugal instability near the sidewall, inflectionally unstable circular waves arise at the outer edge of the bottom boundary layer. However, it appears from their studies that this instability does not influence the spin-down much unless the centrifugal instability is somehow eliminated. Consequently, spin-down is a complex problem with at least two instability mechanisms that lead to more rapid spin-down, and much more complicated dynamics than could possibly be anticipated from the linear theory (Duck & Foster (2001) [13]).

5.3.2 Meridional Circulation

TOP VIEW Data

It has been shown that the main difference between spin-up and spin-down concerns the direction of the basic flow in the interior region. Consequently, the secondary circulation is reversed in the two cases: it is directed inward (outward) in case of spin-up (spin-down) in the interior region.

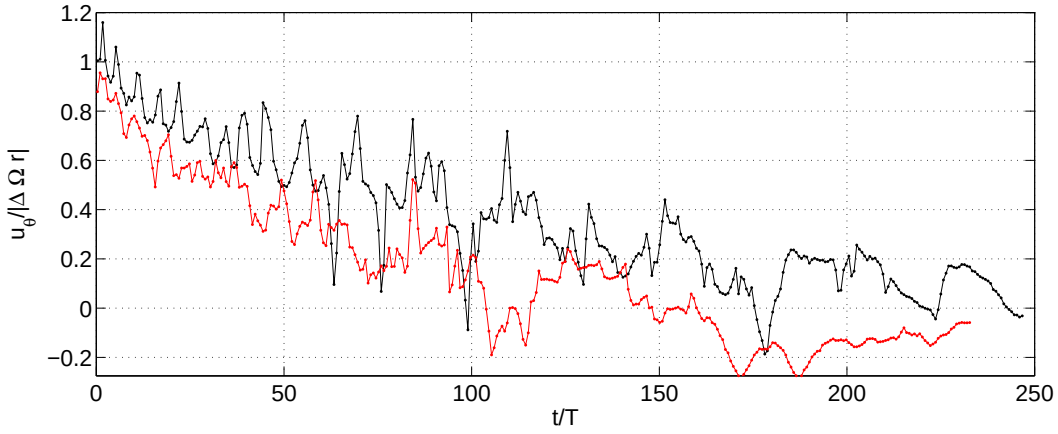

(a) run 1 ($\{\epsilon, Bu\} = \{0.08, 0.26\}$)

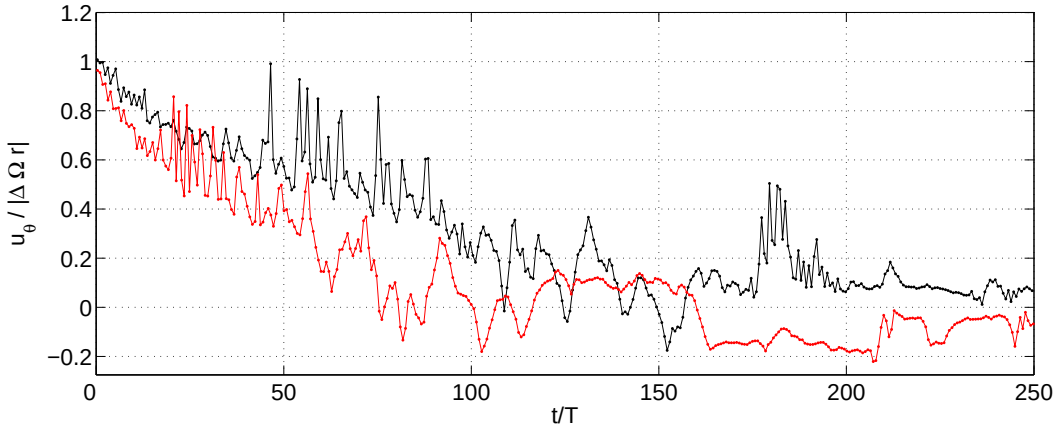

(b) run 2 ($\{\epsilon, Bu\} = \{0.17, 0.26\}$)

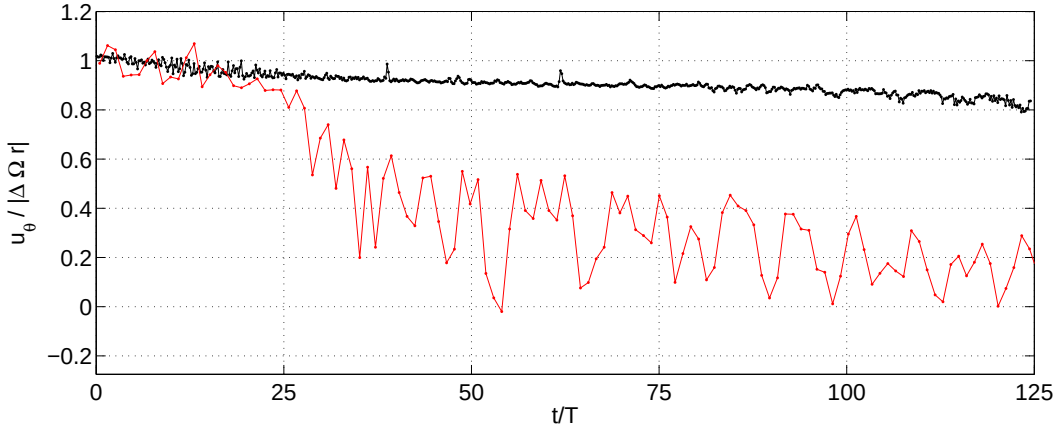

(c) run 3 ($\{\epsilon, Bu\} = \{0.32, 4.34\}$)

Fig. 5.10: TOP VIEW $\{r/R, z/H\} \simeq \{0.80, 0.75\}$ - Spin-up —●— vs Spin-down —●— - non-dimensional azimuthal velocity [−] - temporal evolution

In order to visualize the secondary circulation in the interior region, since this radial flow is characterized by a very small magnitude ($u'_r \sim E^{1/2}$, being $E \sim O(10^{-5})$), the first step was to ensure that the calibration for the TOP VIEW data were sufficiently accurate. The method used consisted in controlling that the radial velocity were zero in the interior region for the run characterized by dominating stratification, i.e., the run UP 3 ($\{\epsilon, Bu\} = \{0.32, 4.34\}$). In fact, the stable stratification restricts the secondary circulation in a region adjacent to the bottom, and no radial motion is expected in the interior such as $z/H \simeq 0.75$. Fig. 5.11(a)

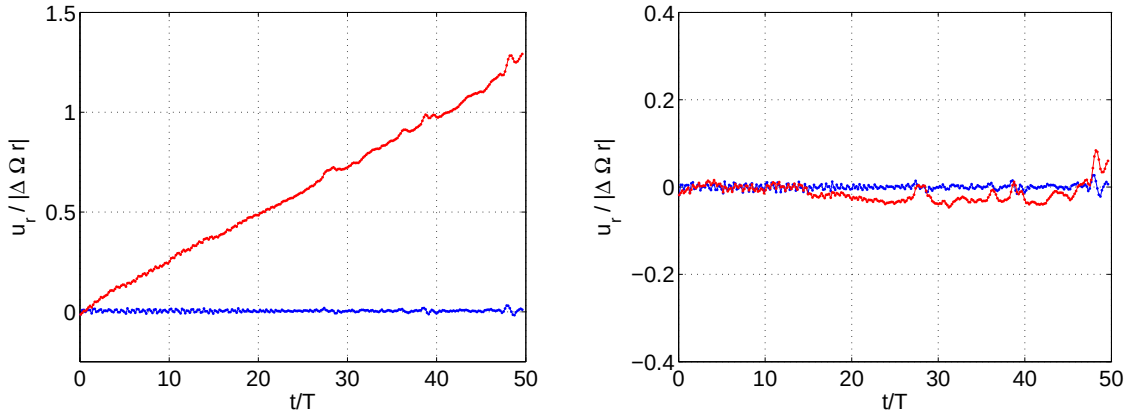

(a) "wrong" configuration

(b) "right" configuration

Fig. 5.11: TOP VIEW $\{r/R, z/H\} \simeq \{0.80, 0.75\}$ UP 3 ($\{\epsilon, Bu\} = \{0.32, 4.34\}$) - non-dimensional radial velocity [−] and its cumulative sum - temporal evolution

shows the non-dimensional radial velocity and its cumulative sum, which represents the net effect, versus time at the level considered. Although the radial velocity is around zero, with fluctuations of very small amplitude, the cumulative sum exhibits a linear increase in time with no physical meaning. This behavior must be due to a continuous slight overestimation of the radial velocity, and it is peculiar of systematic errors. We supposed that the cause could be due to an error in the positioning of the center of the tank during the calibration procedure. More precisely, considering the local cartesian frame of reference (¶ 4.5), the error might affect the x-position of the center of the tank, where the polar frame of reference is centered. Referring to Fig. 5.12, the misleading streamlines associated with the wrong position of the center of the tank induce a false positive radial velocity component in the interior region in case of spin-up. Knowing the radial and azimuthal velocity components in the "wrong" frame of reference and assuming the flow purely azimuthal (i.e., along the axisymmetric streamlines) in the "right" frame of reference, then it is possible to obtain the

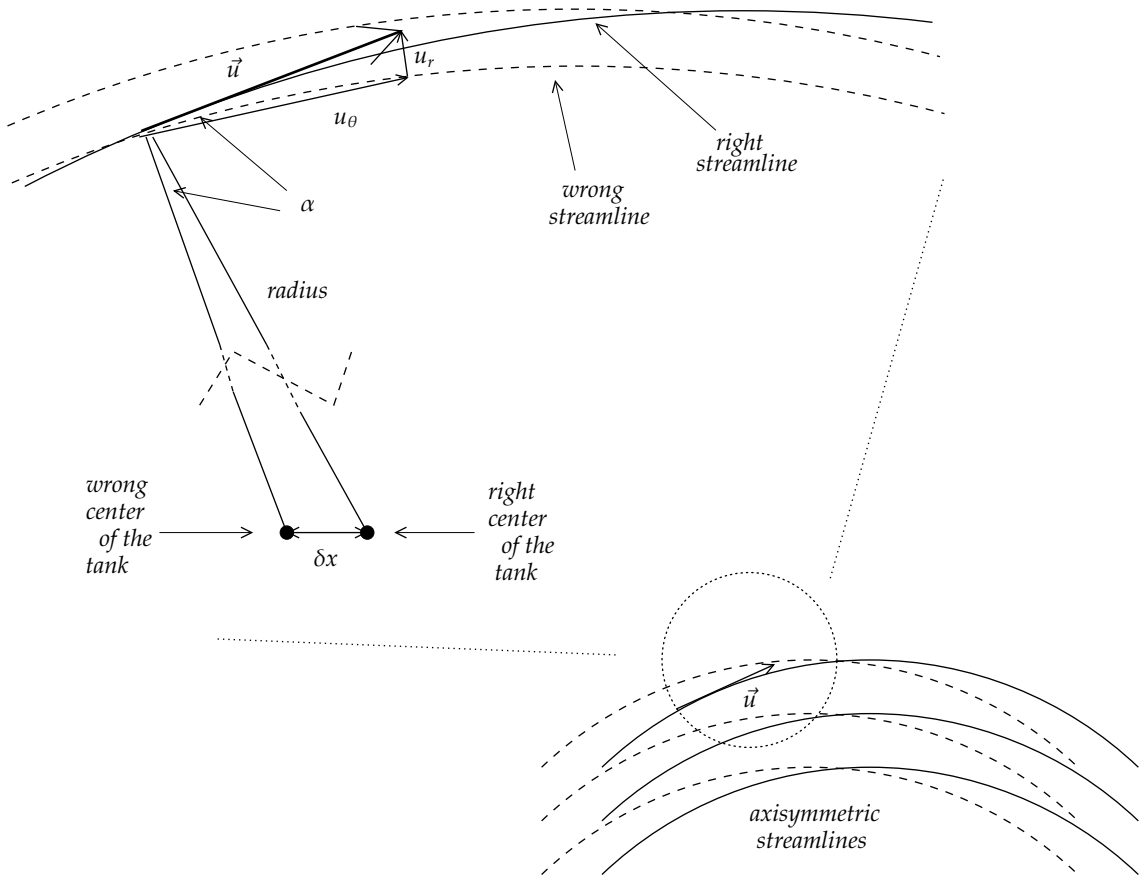

Fig. 5.12: The misleading streamlines associated with the wrong center of the tank induce a false positive radial velocity component in the interior region in case of spin-up.

angle between the wrong and right streamlines, i.e.,

$$\tan\alpha = \frac{u_r'}{u_\theta'}$$

at each time. A temporal average on $t/T \sim 50$ was used to calculate $\overline{\tan\alpha} \simeq 4.8 \cdot 10^{-3}$, which allows to compute a possible correction of the position of the center of the tank, i.e., $\overline{\delta x} \simeq 2.5\ cm$, being $\delta x = r \tan\alpha$.

Fig. 5.11(b) corresponds to Fig. 5.11(a) after the shift of the center of the tank: also the cumulative sum of the radial velocity shows a profile around zero, confirming our hypothesis about the source of the error.

Using the correction, we computed the non-dimensional radial velocity and its cumulative sum versus time at $z/H \simeq 0.75$ for the runs 2 ($\{\epsilon, Bu\} = \{0.17, 0.26\}$). Fig. 5.13 shows that the secondary circulation penetrates deeper in the interior region since the relative importance of stratification with respect to rotation is weaker in the runs 2 rather than in the

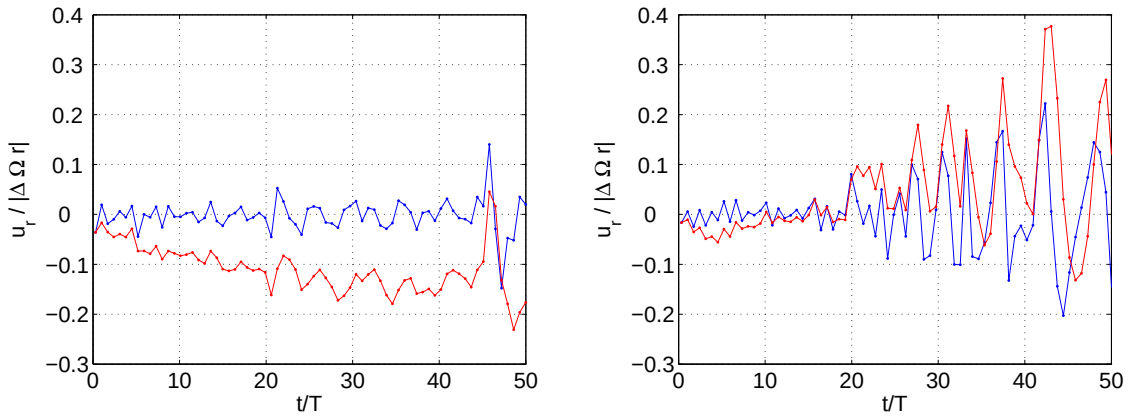

(a) Spin-up (b) Spin-down

Fig. 5.13: TOP VIEW $\{r/R, z/H\} \simeq \{0.80, 0.75\}$ 2 $(\{\epsilon, Bu\} = \{0.17, 0.26\})$ - non-dimensional radial velocity $[-]$ —●— and its cumulative sum —●— - temporal evolution

runs 3. As expected, in the interior region the secondary circulation, visualized by means of the cumulative sum of the radial velocity, is directed inward in case of spin-up (Fig. 5.13(a)) and outward in case of spin-down (Fig. 5.13(b)).

The spin-down run is affected by centrifugal instability, which starts to grow at approximatively $t/T \simeq 25$. Note that the onset of the centrifugal instability in the run DW 2 as evinced from the radial velocity in Fig. 5.13(b) was hidden by the long-wave instability in the azimuthal velocity decay (Fig. 5.10(b)). Notably, it corresponds to the onset of centrifugal instability in the (axisymmetric) run DW 3 at the same radial position (Fig. 5.10(c)). However, a deeper investigation of the centrifugal instability goes beyond the scope of this thesis (see, e.g., Neitzel & Davis (1981) [55]).

5.4 Summary

Dimensional analysis has indicated that the flow evolution depends only on the Burger and Rossby numbers, and in this chapter a preliminary study of the experimental runs has been performed.

We have found that a weak nonlinearity (i.e., $\epsilon = 0.17$) does not alter the general decay trend of the spin-up process. Nevertheless, our results show that the long-wave instability is affected by small differences in the Rossby number even for $\epsilon < 0.22$, the threshold at which the nonlinearity effects were ruled out from the flow dynamics in the literature.

Our results suggest that the Burger number plays a preeminent role in the flow development, controlling the penetration of the secondary circulation, and thus the spatial structure of the velocity field. The vertical profile of the azimuthal velocity suggests the onset of the long-wave instability in case of $Bu < O(1)$, but its specific nature remains to be addressed.

The weakening of the Ekman layer with dominating stratification has been experimentally visualized and the secondary circulation displayed in the interior region, both in spin-up and spin-down runs. The spin-down runs have been found locally centrifugally unstable according to previous studies.

Chapter 6

Stable spin-up

In this chapter the results of the run characterized by axisymmetric velocity field (UP 3: $\{\epsilon, Bu\} = \{0.32, 4.34\}$) are presented. The reason of the preference of spin-up rather than spin-down is that whereas the former is stabilized by its rotation in an early stage, the latter is inevitably complicated by short-wave centrifugal instability near the sidewall.

6.1 Vertical Penetration of the Meridional Flow

TOP VIEW Data

Fig. 6.1 shows the non-dimensional azimuthal velocity versus time at various vertical locations and radial positions. The vertical locations of the horizontal laser sheet are summarized in Tab. 6.1. The levels considered are located in the interior region, relatively well away from the Ekman layer.

The interior azimuthal velocity is not uniform along the vertical direction, and the Taylor-Proudman theorem is no longer applicable. The theoretical penetration depth is $h_p \simeq 39\ cm$ (Eq.n (3.16)), corresponding to $h'_p \simeq 0.65$. The secondary circulation is thus partially limited, due to the strong relative importance of stratification with respect to rotation (i.e., large Burger number). However, the aspect ratio of the experimental facility is $\delta \sim O(10^{-1})$, allowing the secondary circulation to penetrate relatively deeper in the interior region even with dominating stratification. Fig. 6.1 shows that the velocity decay is enhanced at the vertical locations (mainly, the levels 6 and 7) where the secondary circulation is situated (i.e., the rotational shear layer). Note that the velocity decay decreases considerably as the height increases, confirming the confinement of the secondary circulation.

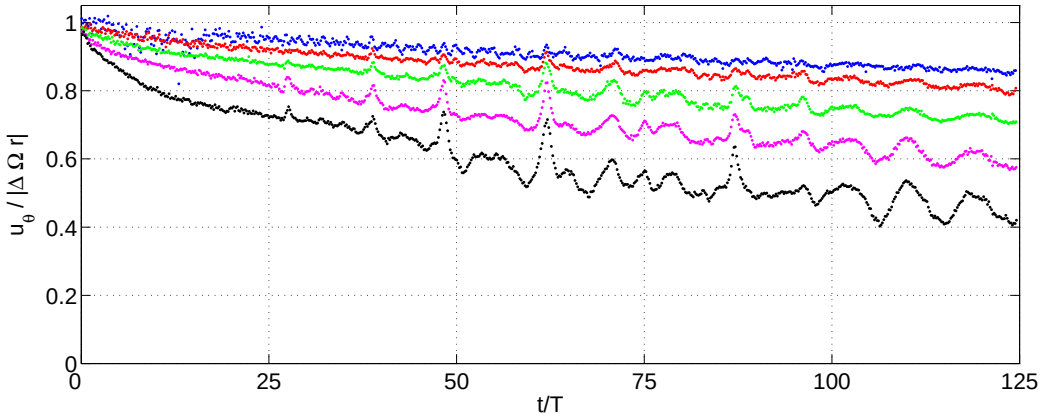

(a) $r/R = 0.70$

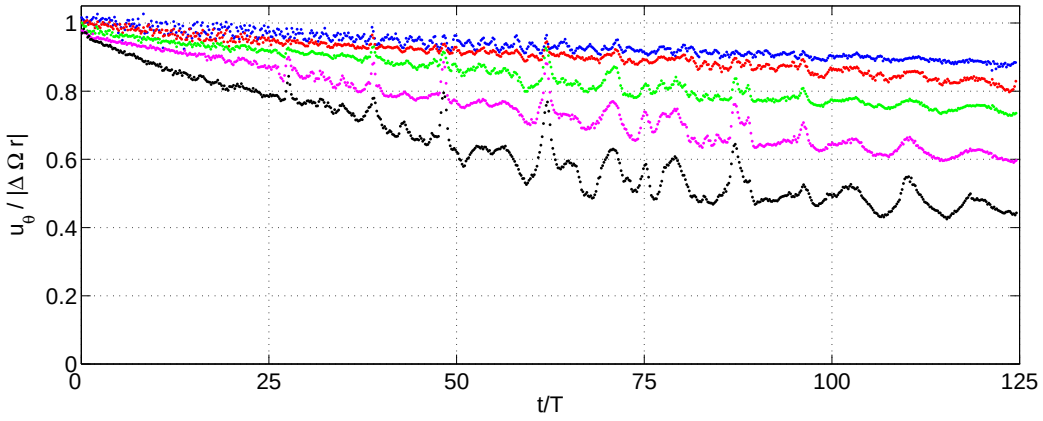

(b) $r/R = 0.80$

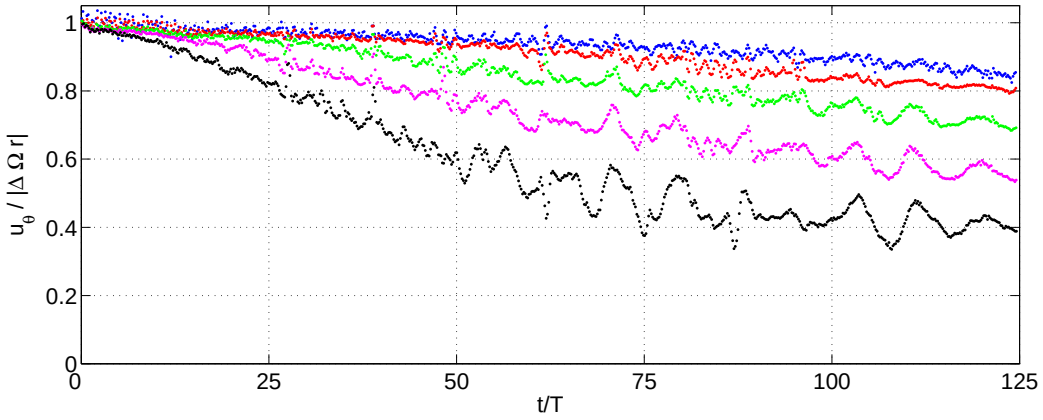

(c) $r/R = 0.90$

Fig. 6.1: TOP VIEW UP 3 ($\{\epsilon, Bu\} = \{0.32, 4.34\}$) - non-dimensional azimuthal velocity [–] - temporal evolution at different vertical locations: level 3; level 4; level 5; level 6; level 7

LEV	**vertical positions**	
	$z\ [cm]$	$z'\ [-]$
1	60	1
2	54.5	0.91
3	49	0.82
4	44.5	0.74
5	38.5	0.64
6	32	0.53
7	26	0.43

Tab. 6.1: UP 3 ($\{\epsilon, Bu\} = \{0.32, 4.34\}$) - vertical positions of the horizontal laser sheet

6.2 Radial Dependence of the Vortex Stretching

TOP VIEW Data

Fig. 6.2 displays the non-dimensional azimuthal velocity versus time at various vertical locations and radial positions. For later discussion, Walin's theoretical predictions for the interior region are also shown. Due to the experimental configuration used, only the velocity field in the radial range $0.65 \leq r/R \leq 1$ was available by means of the TOP VIEW data.

Fig. 6.2 shows that the azimuthal velocity is not uniform along the radial direction. This result is in accordance with Hyun *et al.* (1982) [39]: the spin-up proceeds initially more rapidly at smaller radii and decreases as the radius increases, out of the sidewall boundary layer. This confirms that the vortex-stretching by meridional circulation is stronger at smaller radii.

Note that at approximatively $t/T \sim 50$ the experimental velocities at different radial positions show the same magnitude, suggesting that the radial non-uniformity of the vortex stretching is a transient process.

6.3 Comparison to Walin's theory

Let us perform a comparison between the analytical theory of Walin (1969) [74] and our experimental results. Note that, according to Hyun *et al.* (1982), the initial rotation rate Ω_i was chosen for the scaling. The linear expression derived by Walin (1969) for the decay of the

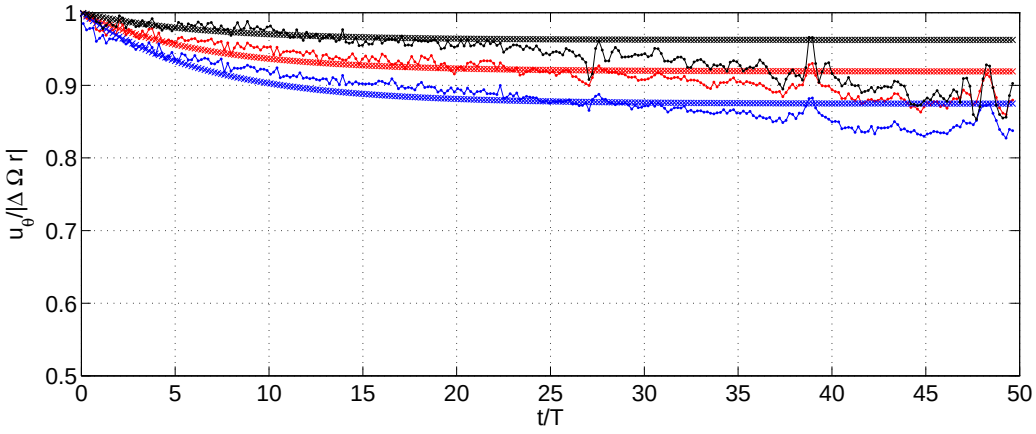

(a) level 5: $z/H = 0.64$

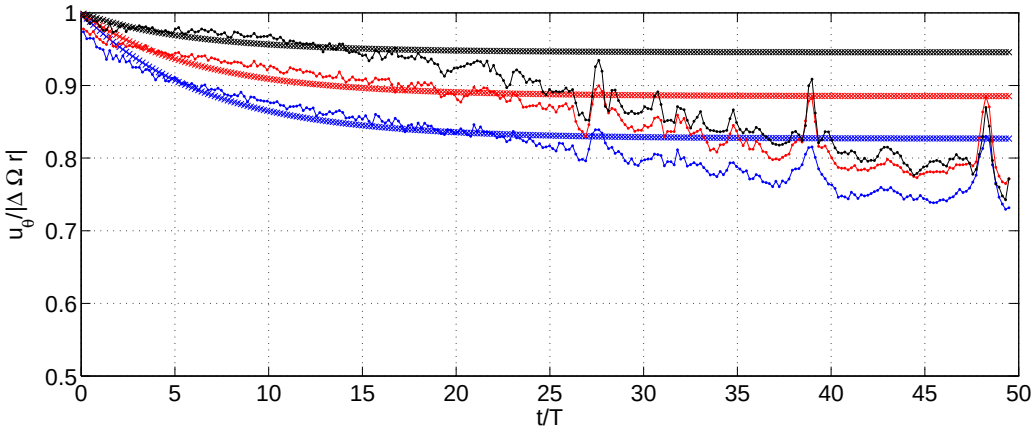

(b) level 6: $z/H = 0.53$

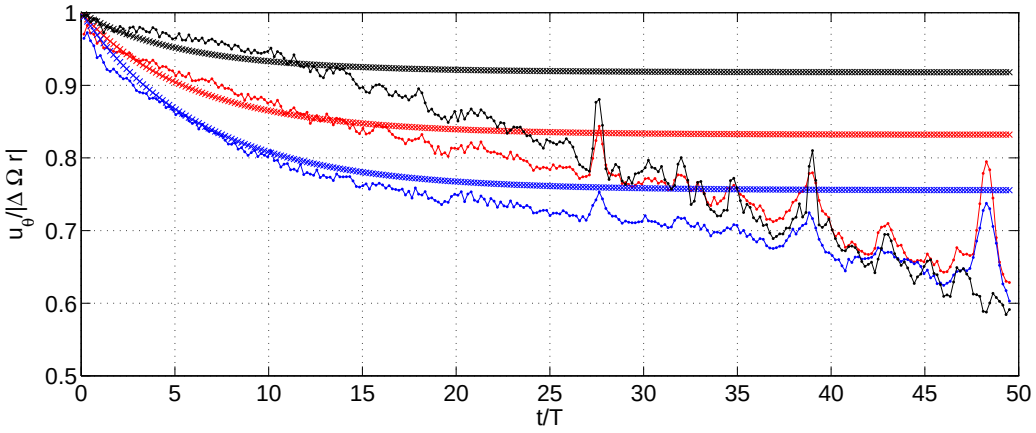

(c) level 7: $z/H = 0.43$

Fig. 6.2: TOP VIEW UP 3 ($\{\epsilon, Bu\} = \{0.32, 4.34\}$) - non-dimensional azimuthal velocity [−] - temporal evolution at different radial positions. Experimental results: —●— $r/R = 0.70$; —●— $r/R = 0.80$; —●— $r/R = 0.90$. Walin's theory: ▨ $r/R = 0.70$; ▨ $r/R = 0.80$; ▨ $r/R = 0.90$

azimuthal velocity in the interior region was shown in Eq.n (3.17a). It could be argued that these are unjustified comparisons since the theory is linear ($\epsilon = 0$) while the experimental results are for $\epsilon = 0.32$. As previously explained, Hyun *et al.* (1982) [39] showed that the results are only weakly dependent on the Rossby number in the range $\epsilon \leq 0.22$, and we confirmed experimentally this results in ¶ 5.1. Moreover, it has been shown (¶ 5.2.2) that, even in case of larger Rossby number ($\epsilon = 0.32$), the nonlinearity does not play a relevant role in the development of the axisymmetric flow.

The Walin's solution was derived in presence of top and bottom horizontal boundaries,

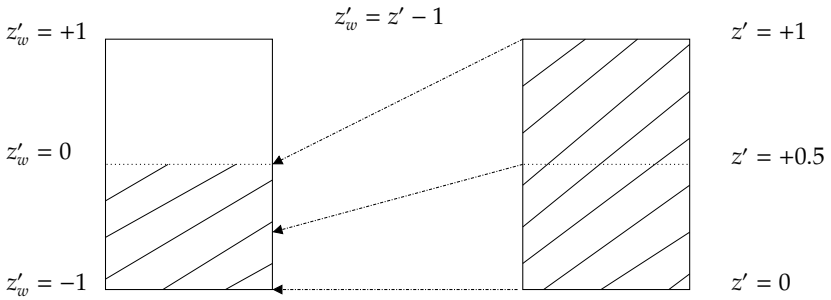

Fig. 6.3: Relation between non dimensional heights: Walin's configuration (left); our runs (right)

e.g., for a close cylinder filled with fluid, while our runs were performed in an open tank, in presence of a free surface. The Walin's solution, symmetric about mid-depth, is usually studied in the lower half part of the fluid, which corresponds to the range $0 \leq z'_w \leq -1$, being z'_w the non-dimensional height used in the Walin's solution. In order to match the whole fluid column in our experiments with the lower half part of the Walin's configuration we used the relation $z'_w = z' - 1$, being $0 \leq z' \leq +1$ (Fig. 6.3).

TOP VIEW Data

Fig. 6.2, which shows the spatial structure of the azimuthal velocity decay, reports also the theoretical predictions of Walin (1969). The theory properly reproduces the experimental velocity decay in early times, but after this initial agreement the curves begin to diverge, with experimental results decaying faster than the theory. The theory of Walin (1969) was scaled using the homogeneous spin-up time scale since it was supposed that viscous-diffusion effects were only significant on the large viscous time scale, as in homogeneous case. However, in agreement with previous experimental and numerical works (¶ 3.3), the comparison with the theory shows a faster rate of decay for the experimental measurements.

Note that the discrepancies between our experimental results and Walin's theory increase in time moving radially outward. The same feature is reported in the comparison between the numerical results of Hyun *et al.* (1982) [39] and Walin's theory (Fig. 6.4), although they used a larger radial range with respect to that available in our experiments.

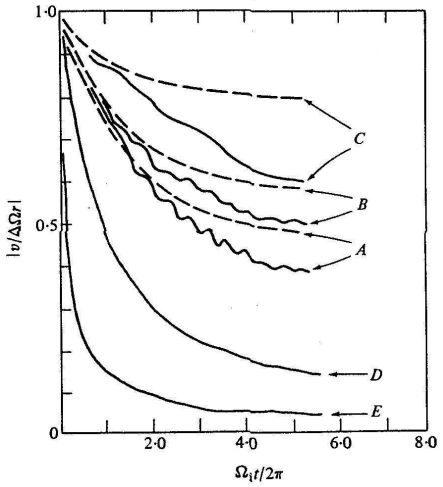

Fig. 6.4: Non-dimensional azimuthal velocity at mid-depth at different radial positions: A) $r/R = 0.23$, B) $r/R = 0.50$, C) $r/R = 0.77$, D) $r/R = 0.96$, E) $r/R = 0.98$. The theoretical prediction for the points in the interior region are shown in broken lines. The Burger number of the simulations, calculated with the initial angular velocity, is $Bu_i = 3.84$ ($Bu_i = 9.47$ for UP 3). Reproduced from Hyun *et al.* (1982) [39].

SIDE VIEW Data

Since all the previous works, both experimental (e.g., Buzyna & Veronis (1971) [6]; Saunders & Beardsley (1975) [66]; Lee (1975) [43]) and numerical (e.g., Barcilon *et al.* (1975) [1]; Hyun *et al.* (1982) [39]), limited the analysis in a time $t/T \sim 8$, we have considered first the non-dimensional azimuthal velocity versus time in the temporal range $0 \leq t/T \leq 20$. Fig.s 6.5 and 6.6 show the experimental results compared with the theoretical predictions of Walin (1969), and for later discussion our improvements to the Walin's theory are also shown.

In the interior region, relatively close to the Ekman layer (Fig. 6.5), again there is an initial agreement for a short time after the start of the run, but the curves begin to diverge, with experimental results decaying faster than the theory. Due to the well separation between the time scales this behavior is observed not only on the viscous, but even over the shorter spin-up time scale. The spin-up time $\tau_{ss} \sim 13.5\ T$, computed by means of Eq.n (3.15), has been reported in Fig. 6.5(a) as a green vertical line.

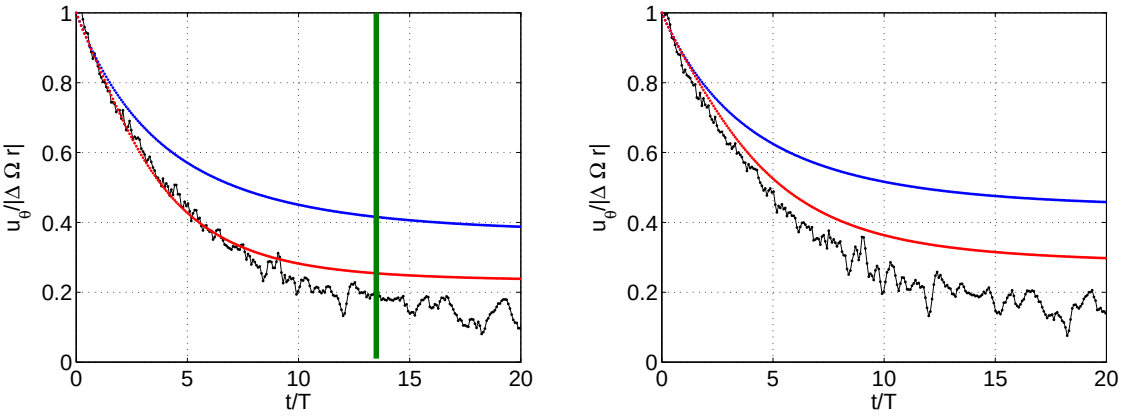

(a) $z/H = 0.10$ (b) $z/H = 0.13$

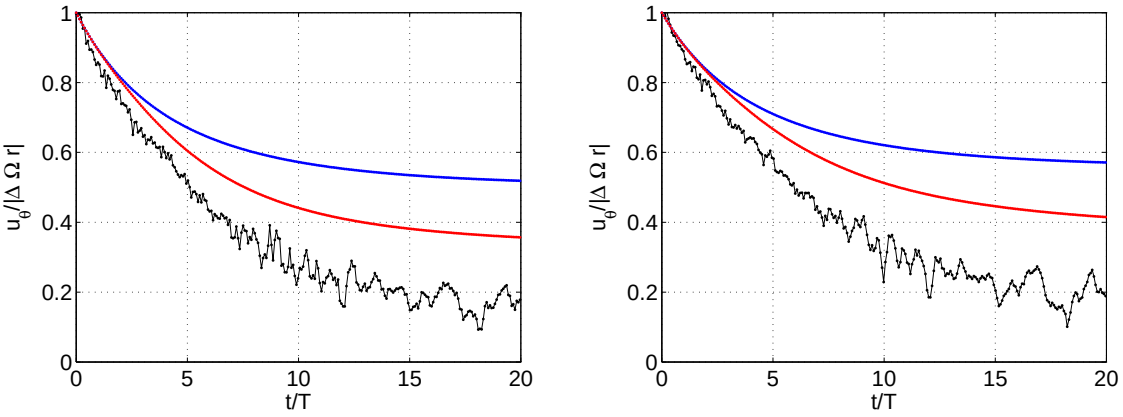

(c) $z/H = 0.16$ (d) $z/H = 0.19$

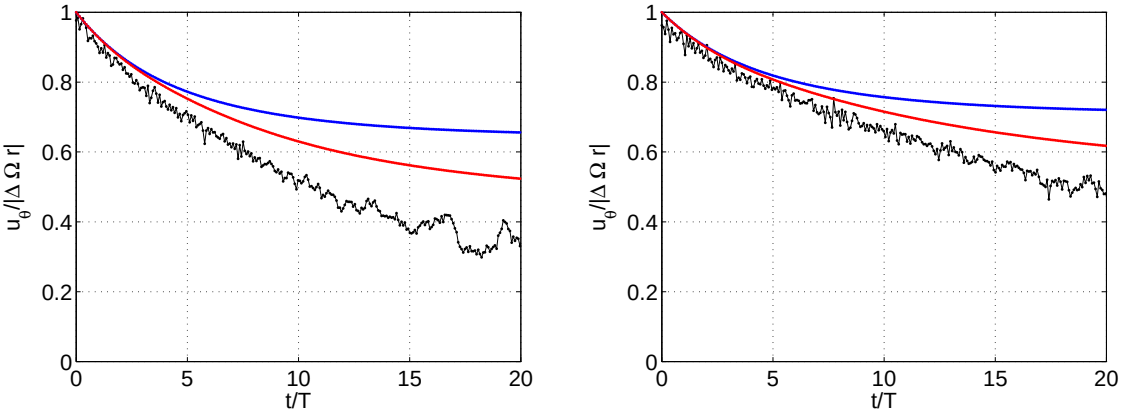

(e) $z/H = 0.22$ (f) $z/H = 0.25$

Fig. 6.5: SIDE VIEW UP 3 ($\{\epsilon, Bu\} = \{0.32, 4.34\}$) - non-dimensional azimuthal velocity [−] - temporal evolution at different vertical locations: —●— experimental results; —●— Walin's theory; —●— our model. The spin-up time has been reported in fig. 6.5(a) as a green vertical line.

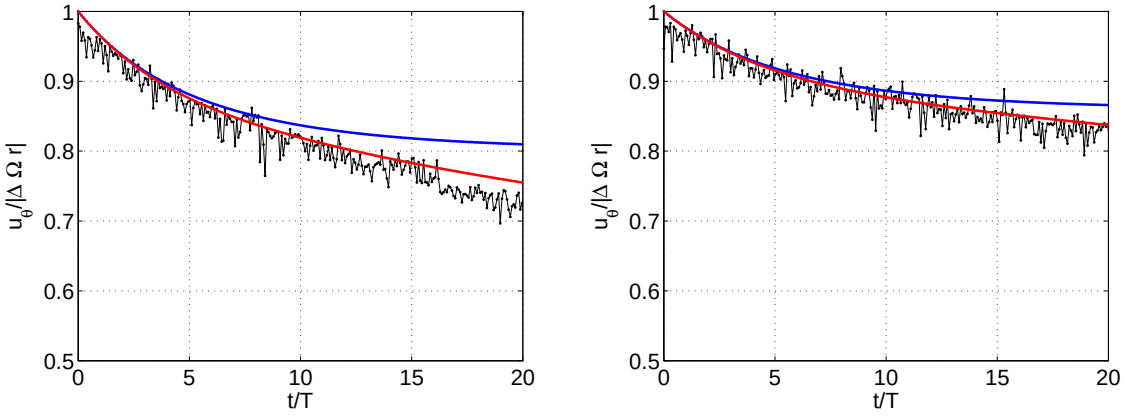

(a) $z/H = 0.35$

(b) $z/H = 0.45$

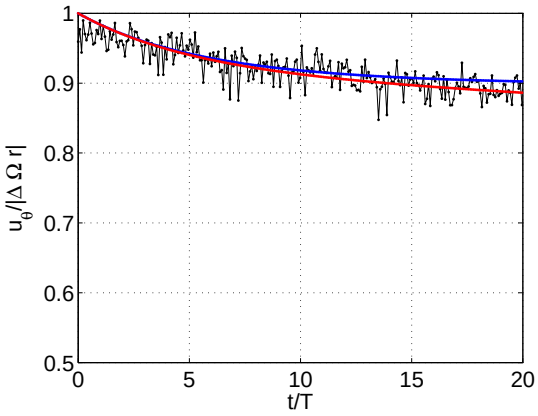

(c) $z/H = 0.55$

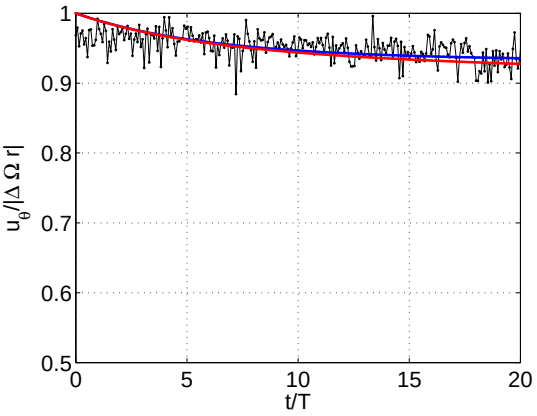

(d) $z/H = 0.65$

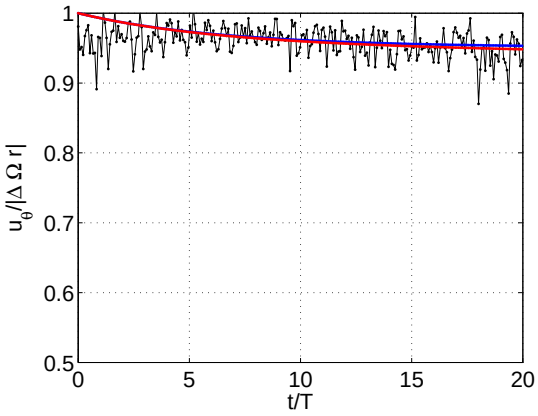

(e) $z/H = 0.80$

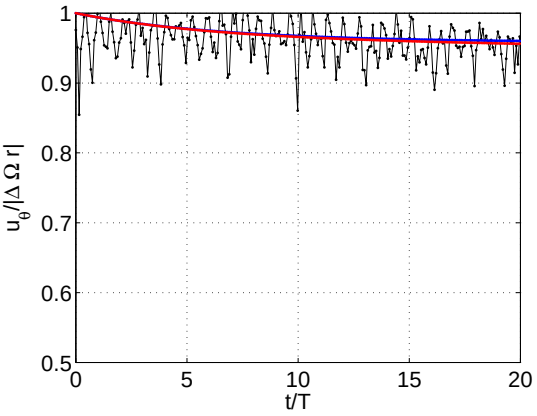

(f) $z/H = 0.90$

Fig. 6.6: SIDE VIEW UP 3 ($\{\epsilon, Bu\} = \{0.32, 4.34\}$) - non-dimensional azimuthal velocity [–] - temporal evolution at different vertical locations: —●— experimental results; —●— Walin's theory; —●— our model

Let us remember that care must be taken concerning the definition of spin-up time when discussing stratified spin-up problems. The spin-up time expressed by Eq.n (3.15) describes a quasi-steady localized spin-up process valid in the rotational shear layer. The Walin's solution shows an asymptotic behavior since it keeps in account only the secondary circulation, omitting viscous-diffusion effects. Thereby, in a region adjacent to the Ekman layer the spin-up time must coincide with the time in which the Walin's solution reaches his asymptotic value. In the run UP 3 the penetration depth is $h'_p \sim 0.65$, and therefore the azimuthal temporal profile of Fig. 6.5(a) is computed in the region mostly affected by the spin-up mechanism. This explains the good accordance between the Walin's solution and the theoretical spin-up time scale (cf., Fig. 6.8(a), a long time evolution of fig. 6.5(a) where the spin-up time has been also reported).

In the interior region, well away from the Ekman layer (Fig.s 6.6(a)-(b)-(c)), the accor-

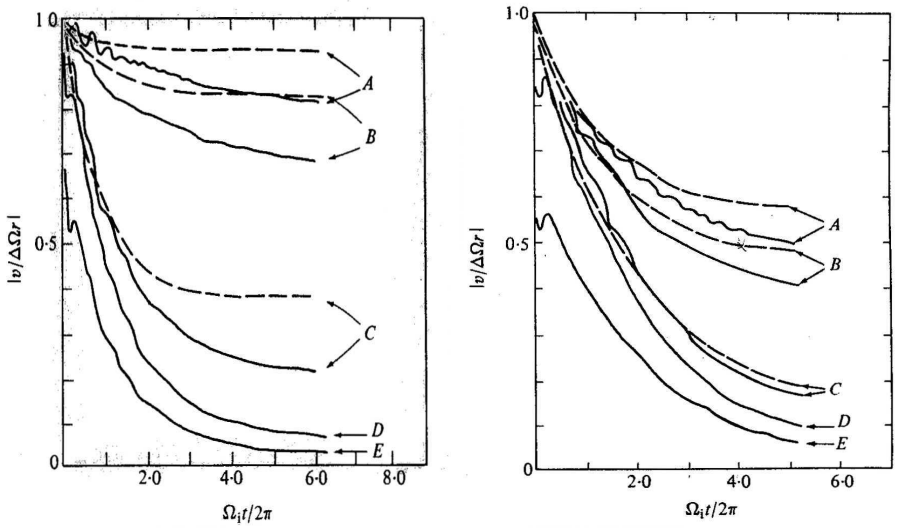

(a) $Bu_i = 16.97$ (b) $Bu_i = 3.84$

Fig. 6.7: Non-dimensional azimuthal velocity at mid-radius at different vertical locations: A) $z/H = 0$, B) $z/H = -0.42$, C) $z/H = -0.82$, D) $z/H = -0.93$, E) $z/H = -0.97$. The theoretical prediction for the points in the interior region are shown in broken lines. The Burger number of the simulations, Bu_i, is calculated with the initial angular velocity ($Bu_i = 9.47$ for the run UP 3). Reproduced from Hyun *et al.* (1982) [39].

dance between the curves increases in the temporal range considered. Hyun *et al.* (1982) found larger discrepancies between their numerical results and Walin's theory in case of strong stratification (Fig. 6.7(a)). Moreover, in case of weak stratification they found that the disagreement, again wider with respect to our comparison, increased approaching mid-

depth (Fig. 6.7(b)). Note that the numerical simulation of Hyun *et al.* (1982) were conducted in a close cylinder filled with fluid, and the same reasoning made for Walin's solution is valid. Hyun *et al.* (1982) did not explain the causes of these discrepancies between relatively strong and weak stratified flow. We suggest that the curve (*C*) is located in the rotational shear layer in case of weak stratification (Fig. 6.7(b)), and thus the Walin's solution shows a very good agreement. In case of strong stratification (Fig. 6.7(a)), the curve (*C*) is located out of the region directly affected by the secondary circulation. Therefore, the viscous-diffusion effects, omitted in the Walin's solution, may account for the discrepancies between numerical results and Walin's solution.

We report also the results for the upper half part of the fluid (Fig. 6.6(d)-(e)-(f)), absent in the work of Hyun *et al.* (1982) since the configuration used was symmetric about mid-depth. In the temporal range considered Walin's theory and experimental results are consistent. More precisely, the velocity profile predicted by the Walin's theory falls inside the range of fluctuations of the measured velocity.

Note that the discrepancies just after the start of the run in Fig. 6.6 may be due to the fact that the fluid was not perfectly in solid body rotation at $t/T < 0$. In fact, this disagreement affects the region far away from the bottom boundary and is lacking in the region close to the Ekman layer (Fig. 6.5). However, the initial discrepancies in the azimuthal velocity are at maximum of the order of 5%, and thus the general meaning of the discussion is not modified.

6.4 Improvement to Walin's theory

SIDE VIEW Data

A different picture emerges from the long time evolution of the azimuthal velocity. Fig.s 6.8 and 6.9 correspond to Fig.s 6.5 and 6.6 for a wider temporal range. The discrepancies between the experimental results and the Walin's theory are considerable. Since the Walin's solution keeps in account only the contribution of the secondary circulation, when the partial spin-up of the fluid is completed no further velocity decrease is expected.

Hyun (1983) [37] suggested that any viable model for stratified spin-up should include the viscous-diffusion effects in both the boundary layers and the interior region. We decided, thus, to incorporate the viscous-diffusion effects in the Walin's analytical solution (3.17a) as to improve the azimuthal velocity predictions.

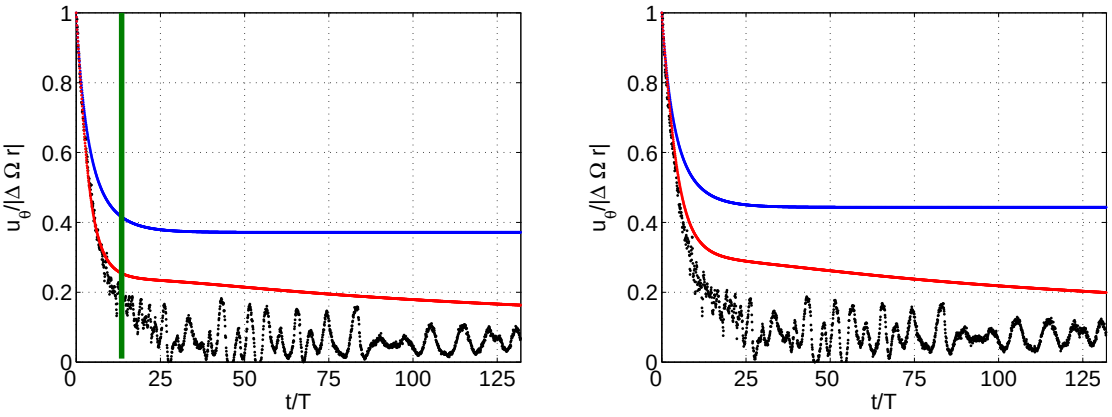

(a) $z/H = 0.10$

(b) $z/H = 0.13$

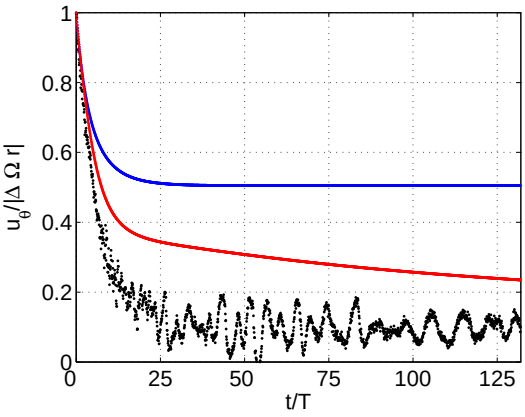

(c) $z/H = 0.16$

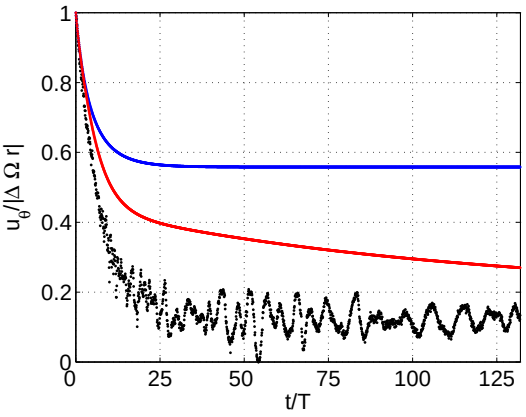

(d) $z/H = 0.19$

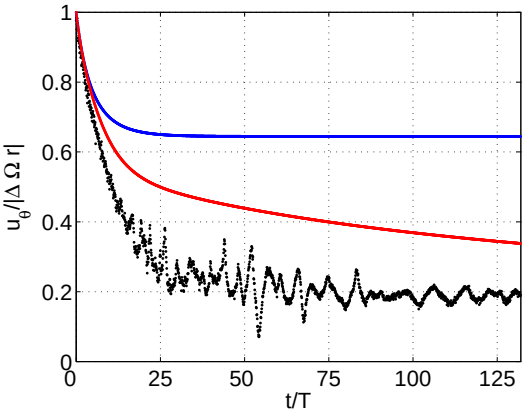

(e) $z/H = 0.22$

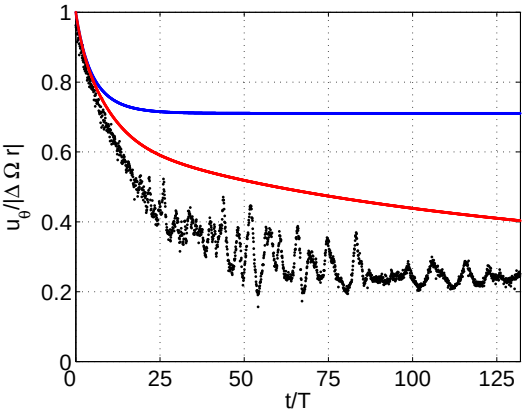

(f) $z/H = 0.25$

Fig. 6.8: SIDE VIEW UP 3 ($\{\epsilon, Bu\} = \{0.32, 4.34\}$) - non-dimensional azimuthal velocity [−] - temporal evolution at different vertical locations: —●— experimental results; —●— Walin's theory; —●— our model. The spin-up time has been reported in fig. 6.8(a) as a green vertical line.

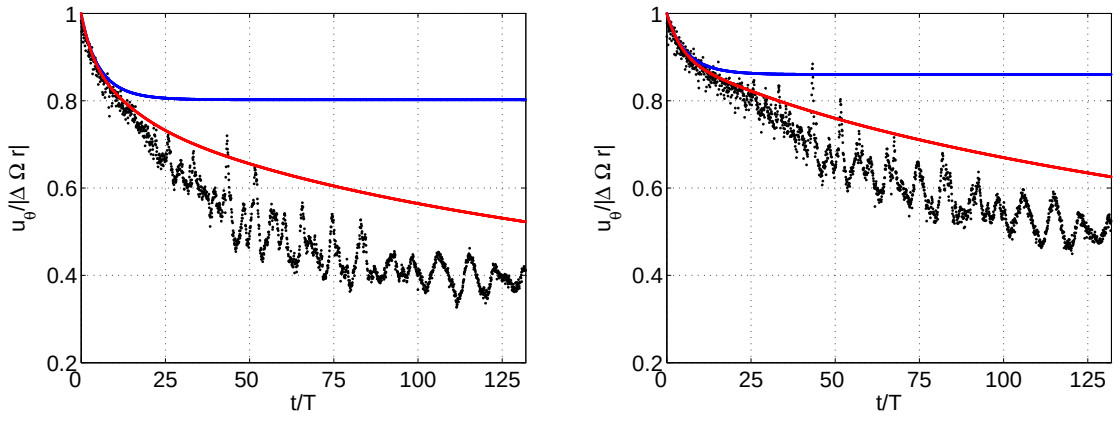

(a) $z/H = 0.35$

(b) $z/H = 0.45$

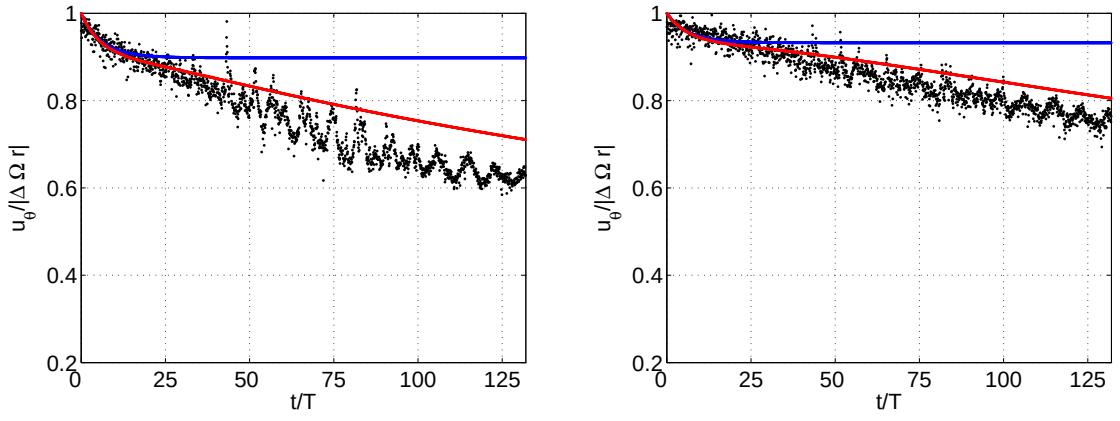

(c) $z/H = 0.55$

(d) $z/H = 0.65$

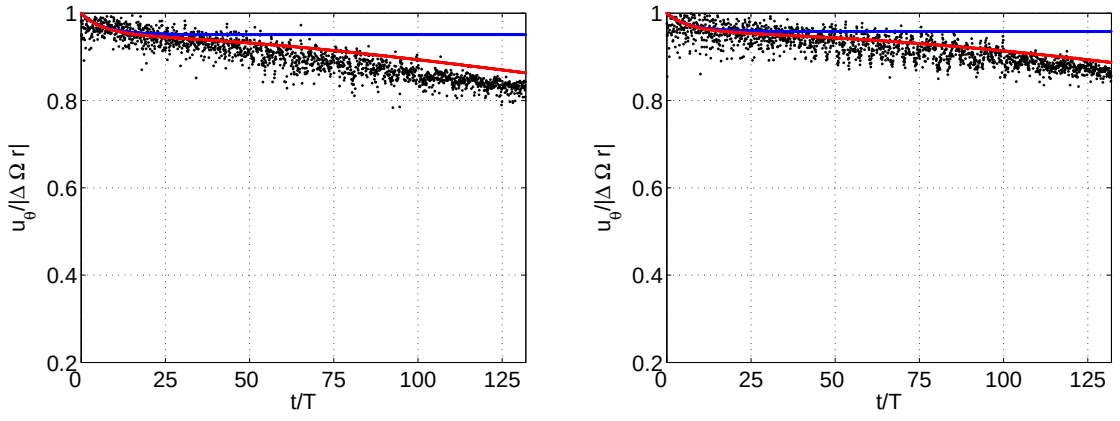

(e) $z/H = 0.80$

(f) $z/H = 0.90$

Fig. 6.9: SIDE VIEW UP 3 ($\{\epsilon, Bu\} = \{0.32, 4.34\}$) - non-dimensional azimuthal velocity [–] - temporal evolution at different vertical locations: —●— experimental results; —●— Walin's theory; —●— our model

In cylindrical coordinates, the azimuthal component of Eq.n (3.12a) is

$$\tau' \frac{\partial u'_\theta}{\partial t'} + 2u'_r = E\nabla'^2 u'_\theta \tag{6.1}$$

We used the finite differences method for solving Eq.n (6.1), omitting the Coriolis term. In fact, this term provides the contribution of the secondary circulation, and it is already considered in the analytical solution of Walin (1969). Since the vertical Ekman number $E_v = \nu/\Omega H^2$ is larger than the horizontal Ekman number $E_h = \nu/\Omega L^2$ ($L >> H$)

$$\tau' \frac{\partial u'_\theta}{\partial t'} = E_v \frac{\partial^2 u'_\theta}{\partial z'^2} \tag{6.2}$$

being the azimuthal velocity of the flow at the fixed radial position $r/R \simeq 0.85$ (i.e., the radial position of the SIDE VIEW data) function of time $t' = t/T$ and height $z' = z/H$, i.e., $u'_\theta = u'_\theta(z', t')$. We impose $\tau' \sim O(1)$: since in ¶ 3.2 we defined $t' = t/\tau$, being $\tau \equiv \Omega^{-1}\tau'^{-1}$, this assumption simply states $t' = t/T$. Then, Eq.n (6.2) is the vertical diffusion equation of the azimuthal velocity,

$$\frac{\partial u'_\theta}{\partial t'} = E \frac{\partial^2 u'_\theta}{\partial z'^2} \tag{6.3}$$

being $E \equiv E_v$.

The basic idea of the finite differences method for solving partial differential equations is to replace spatial and time derivatives by suitable approximations, then to numerically solve the resulting difference equations. Specifically, instead of solving for $u'_\theta(z', t')$ with z' and t' continuous, we have solved for ${u'_\theta}_i^j(z'_i, t'_j)$, where $z'_i \equiv i\,\delta z'$ and $t'_j \equiv j\,\delta t'$ define the grid shown in Fig. 6.10. The discrete time t'_j was chosen according to the sampling time (15 s) and the height was discretized in $nlev = 45$ vertical levels z'_i.

The first order derivative

$$\frac{\partial u}{\partial z} \equiv \lim_{\Delta z \to 0} \frac{\Delta u}{\Delta z}$$

(being $u \equiv u'_\theta$, $z \equiv z'$ and $t' \equiv t$ in order to lighten the notation), evaluated at the grid points (z_i, t_j), may be approximated in many different ways, the simplest being the following

- Forward Difference

$$\left(\frac{\partial u}{\partial z}\right)_i^j \approx \frac{u_{i+1}^j - u_i^j}{z_{i+1} - z_i} = \frac{u_{i+1}^j - u_i^j}{\delta z}$$

- Backward Difference

$$\left(\frac{\partial u}{\partial z}\right)_i^j \approx \frac{u_i^j - u_{i-1}^j}{z_i - z_{i-1}} = \frac{u_i^j - u_{i-1}^j}{\delta z}$$

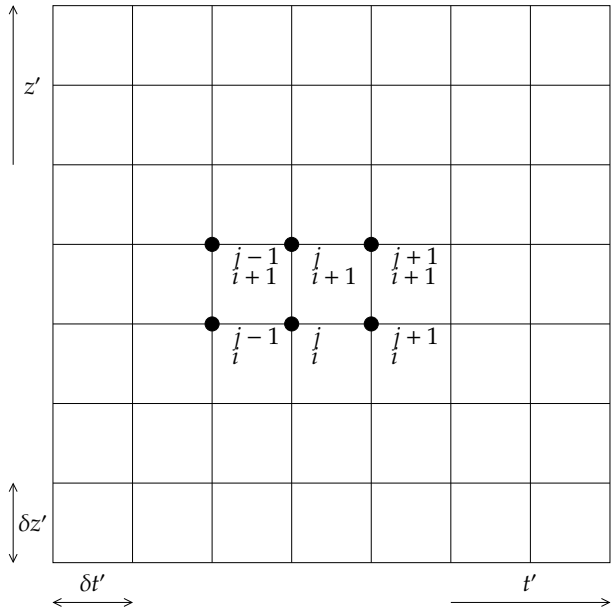

Fig. 6.10: Grid for our finite difference approximations. The point labelled i, j corresponds to $(z', t') = (z'_i, t'_j)$.

- Central Difference

$$\left(\frac{\partial u}{\partial z}\right)_i^j \approx \frac{u_{i+1}^j - u_{i-1}^j}{z_{i+1} - z_{i-1}} = \frac{u_{i+1}^j - u_{i-1}^j}{2\,\delta z}$$

The second order derivative

$$\frac{\partial^2 u}{\partial z^2} \equiv \lim_{\Delta z \to 0} \frac{\Delta\left(\frac{\partial u}{\partial z}\right)}{\Delta z}$$

may be evaluated at the (fictitious) grid points $(z_{i+\frac{1}{2}}, t_j)$ using the central difference approximations

$$\left(\frac{\partial^2 u}{\partial z^2}\right)_{i+\frac{1}{2}}^j \approx \frac{\left(\frac{\partial u}{\partial z}\right)_{i+\frac{1}{2}}^j - \left(\frac{\partial u}{\partial z}\right)_{i-\frac{1}{2}}^j}{z_{i+\frac{1}{2}} - z_{i-\frac{1}{2}}} = \frac{u_{i+1}^j - 2u_i^j + u_{i-1}^j}{(\delta z)^2} \tag{6.4}$$

Following the same reasoning for the derivative with respect to time

$$\left(\frac{\partial u}{\partial t}\right)_i^j \approx \frac{u_i^{j+1} - u_i^j}{t_{j+1} - t_j} = \frac{u_i^{j+1} - u_i^j}{\delta t} \tag{6.5}$$

Using Eq.ns (6.4) and (6.5) in Eq.n (6.3), and rearranging, the considered finite difference equation can be iterated in order to find the approximate solution to the diffusion equation,

$$u_i^{j+1} = u_i^j + s(u_{i+1}^j - 2u_i^j + u_{i-1}^j) = s(u_{i+1}^j - u_{i-1}^j) + (1 - 2s)u_i^j \quad (i = 2 : nlev - 1) \tag{6.6}$$

being

$$s \equiv E\frac{\Delta t}{(\Delta z)^2} \tag{6.7}$$

To solve this difference equation both initial and boundary conditions are required. The initial condition is the solid body rotation of the whole fluid with no-slip condition at the bottom (i.e., $u^{j=1}_{i=2:nlev} = 1$ and $u^{j=1}_{i=1} = 0$), while local Ekman friction and no-flux are the boundary conditions at the bottom and at the free surface, respectively.

The local Ekman friction condition at the bottom states

$$\left(\frac{\partial u}{\partial z}\right)^j_{i=1} \approx \frac{u^j_{i=1}}{\delta_E}$$

then

$$\frac{u^j_{i=2} - u^j_{i=1}}{\delta z} = \frac{u^j_{i=1}}{\delta_E}$$

which allows to calculate $u^j_{i=1}$

$$u^j_{i=1} = \frac{u^j_{i=2}}{1+\kappa} \tag{6.8}$$

being $\kappa \equiv \delta z/\delta_E$.

The no-flux condition at the free surface is a form of stress boundary condition. Since the free surface is uniform in composition and temperature, the tangential stress is continuous across the interface

$$E_w\left(\frac{\partial u}{\partial z}\right)^j_{i=nlev} = E_a\left(\frac{\partial u}{\partial z}\right)^j_{i=nlev}$$

where E_w and E_a are the Ekman number in water and air respectively. Since $E_a \ll E_w$ ($\nu_a \ll \nu_w$) the shear stress vanishes at the free surface, i.e,

$$\left(\frac{\partial u}{\partial z}\right)^j_{i=nlev} \approx \frac{u^j_{i=nlev} - u^j_{i=nlev-1}}{\delta z} = 0 \tag{6.9}$$

which allows to impose $u^j_{i=nlev} = u^j_{i=nlev-1}$.

In our model, at each time, the contributions of both secondary circulation and viscous-diffusion to the decay rate of the azimuthal velocity are considered. More precisely, the diffusion equation is solved using the velocity field which keeps in account the decay rate due to both secondary circulation and diffusion during the previous times. In this way, velocity gradients created in the interior by the secondary circulation are considered at each time in the diffusion equation. The Walin's solution is calculated independently by means of the analytical solution (Eq.n (3.17a)) of Walin (1969). Since its contribution is larger than diffusion during the spin-up time scale, then it should be only slightly affected by the inclusion

of viscous-diffusion effects. Consequently, we suppose that the analytical solution of Walin is still valid to represent the secondary circulation also in presence of velocity gradients. When the secondary circulation has spun-up the fluid in a region adjacent to the bottom of the tank, its contribution nullifies and the velocity decay is due wholly to diffusion.

This is an attempt to provide an easy procedure to include viscous-diffusion effects in

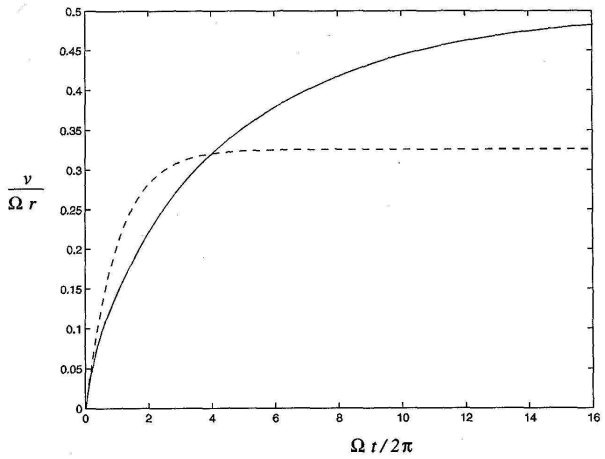

Fig. 6.11: Azimuthal velocity ($r' = 0.5$, $z' = 0.5$) during large-σ spin-up at relatively large Burger number. The Walin's solution (- - -); composite of Walin's solution and viscous-diffusion effects (—). Note that the frame of reference rotating with the initial angular velocity is considered. Reproduced from Duck & Foster (2001) [13].

the Walin's solution. In fact, Duck & Foster (2001) [13], considering the longer, diffusive timescale (by setting $\tau' = E^{-1}$) and solving Eq.ns (3.12) found that the solution takes a particularly simple form in the case of large Schmidt number limit ($\sigma \to \infty$). They included the viscous-diffusion solution in the Walin's solution (Fig. 6.11) and agreed that the absence in the Walin's theory regarding the modeling of the diffusive timescale behavior may be responsible for the discrepancies. However, they did not explain further the procedure and perform any comparison with neither experimental nor numerical results.

The inclusion of the viscous-diffusion effects allows a general enhancement of the consistency with the experimental results. In the interior region, close to the Ekman layer (Fig.s 6.5 and 6.8), the divergence with the experimental results starts later and is less considerable. Our model behaves even better in the interior region, well away from the Ekman layer (Fig.s 6.6(a)-(b)-(c) and Fig.s 6.9(a)-(b)-(c)). In fact, substantial flow gradients are created by the secondary circulation in this region. Thereby, the inclusion of viscous-diffusion effects causes a faster decrease of the azimuthal flow, even over the spin-up time scale. In the upper half part of the fluid (Fig.s 6.6(d)-(e)-(f) and Fig.s 6.9(d)-(e)-(f)) the experimental results and

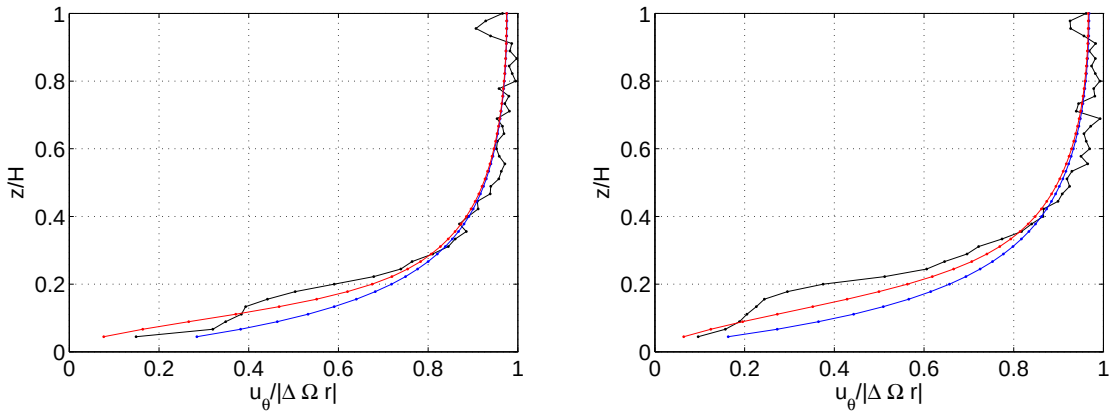

(a) $t/T = 5$

(b) $t/T = 10$

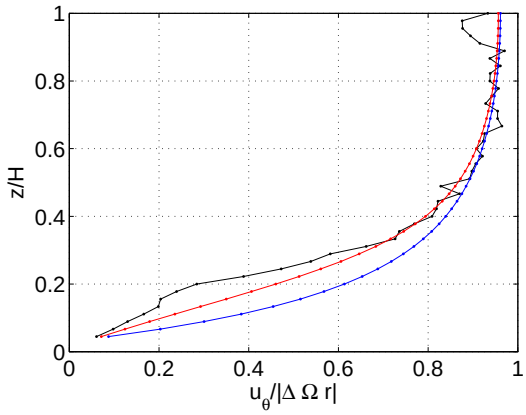

(c) $t/T = 20$

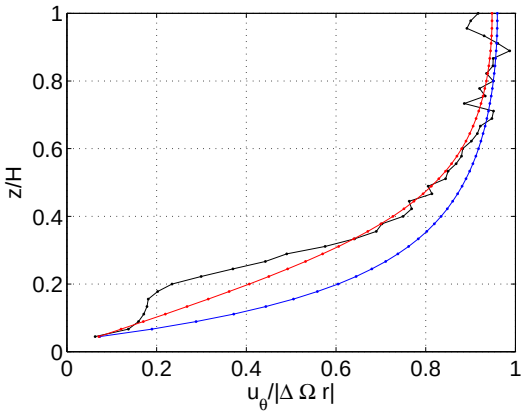

(d) $t/T = 40$

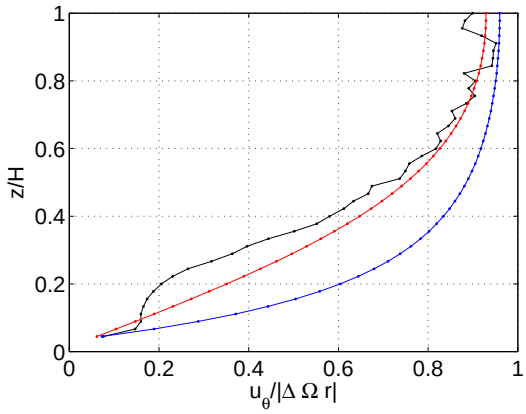

(e) $t/T = 80$

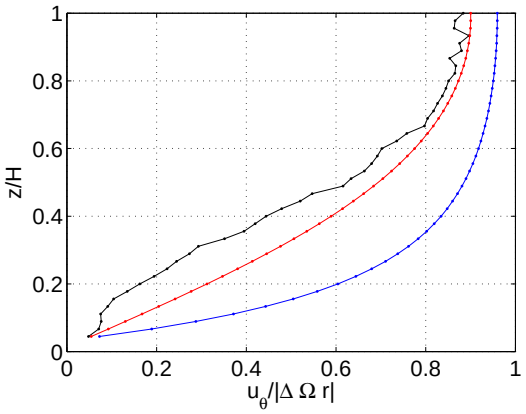

(f) $t/T = 120$

Fig. 6.12: SIDE VIEW UP 3 ($\{\epsilon, Bu\} = \{0.32, 4.34\}$) - non-dimensional azimuthal velocity [−] - vertical profile temporal evolution: —●— experimental results; —●— Walin's theory; —●— our model

our model are in very good agreement. This is the region where the secondary circulation does not penetrate and its effect is slightly felt. Consequently, the diffusion equation plays a preeminent role and it is capable to correctly estimate the azimuthal velocity decay. This suggests that, even if the Reynolds number [1] is $\sim O(10^4)$ in the interior region, stratification and rotation efficiently prevent the onset of turbulence.

Note that the lower locations of the flow exhibit the development of velocity oscillations from $t/T \simeq 25$ (Fig. 6.8). These locations are inside the rotational shear layer, where the flow is characterized by a vertical shear in the azimuthal velocity. This suggests that a computation of the Burger number using the full depth of the fluid, which corresponds to $Bu > O(1)$, might not be representative of the flow dynamics in the whole domain. A Burger number based on the effective penetration depth of the secondary circulation is consistent with the presence of baroclinic instability at lower vertical locations, according to Eq.n (2.29).

Fig. 6.12 shows the temporal evolution of the vertical profile of the azimuthal velocity. Note that the Walin's solution is constant from $t/T = 20$ (Fig. 6.12(c)) because the spin-up time scale has elapsed. Fig. 6.12 confirms that the best accordance between the experimental data and our model takes place generally in the upper half part of the fluid. These profiles match very well with the theoretical penetration depth $h'_p = 0.65$: in fact, the velocity decrease is very weak above this level pointing to the confinement of the secondary circulation. The good agreement between the experimental results and our model persists even over large time scales.

6.5 Vanishing of the Ekman Layer

The bottom Ekman layer is the region where the interior azimuthal velocity adjusts to the velocity of the bottom boundary, and it decays as the interior fluid gradually spin-up. The Ekman layer eventually vanishes when the secondary circulation is eliminated. The flow transported along the bottom boundary could develop series of horizontal roll vortices associated with instabilities in the laminar Ekman layer. Experimental (e.g., Faller (1963) [18]; Faller & Kaylor (1966a) [20] ; Tatro & Mollo-Christensen (1967) [71]) and numerical investigations (e.g., Lilly (1966) [44]; Faller & Kaylor (1966b) [19]) have shown that the Ek-

[1] The (vertical) *Reynolds number*, $Re \equiv UH/\nu$, indicates the relative importance of advective term to viscous force.

man layer becomes unstable for *local* Reynolds numbers [2] around $Re_{\delta_e} = 55$. There are two different types of instability associated with this boundary layer: type I waves, due to an inflectional instability, and type II waves, resulting from an interaction of shear and Coriolis force (see, e.g., Greenspan (1968) [30]). A new, stable, laminar motion could result from these disturbances, or a transition to turbulence might take place, which eventually destroys the instabilities. Using laboratory experiments, Caldwell & Van Atta (1970) [7] gave support for the theoretical criterion and found that the transition threshold to fully turbulent regime does not occur until $Re_{\delta_e} = 148$.

The vertical laser sheet used ($60\ cm \times 60\ cm$) is not really appropriate for local measure-

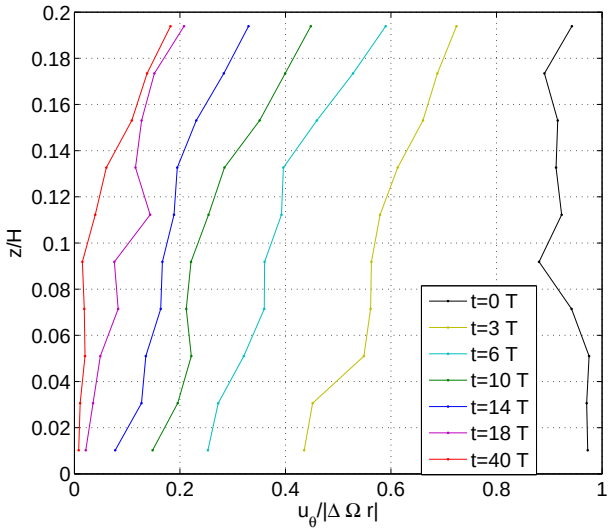

Fig. 6.13: SIDE VIEW UP 3 ($\{\epsilon, Bu\} = \{0.32, 4.34\}$) - non-dimensional azimuthal velocity [−] - vertical profile temporal evolution in a region near the bottom Ekman layer

ments in the Ekman layer. In fact, an Ekman layer thickness can be defined as $\delta_e \equiv E^{1/2}H = (\nu/\Omega_f)^{1/2} \simeq 0.57\ cm \rightarrow \delta_e/H \simeq 0.01$, too thin to be revealed by the measurement technique considered. Note that another definition of Ekman layer thickness is the distance at which the radial velocity analytical solution (Eq.n (3.6a)) has its first zero away from the boundary, namely $\delta_e/H = \pi E^{1/2} \simeq 0.03$. Anyway, our model was developed for large scale velocity profile, using crude boundary conditions, and does not allow to properly compare velocity fields in the range $z/H < 0.03$. Therefore, in Fig. 6.13 we report only the vertical profile of

[2] A Reynolds number based on the local measured values may be defined in the Ekman layer, $Re_{\delta_e} \equiv U\delta_e/\nu = U/(\nu\Omega)^{1/2}$, since its structure depends critically on the local external flow field.

the experimental non-dimensional azimuthal velocity at different times in a region close to the Ekman layer.

Just after the change in the rotation rate of the tank ($t/T = 0$) the fluid rotates approximatively at the imposed angular velocity ($u'_\theta \simeq 1$), even close to the Ekman layer. As time elapses, the velocity profile decays quickly, and the vertical shear in the bottom reduces greatly. From these measurements it appears that the interior azimuthal velocity satisfy the bottom boundary conditions directly over intermediate time scales. More precisely, the interior azimuthal flow adjusts smoothly from the interior region to the bottom boundary without undergoing boundary-like variations, unlike the homogeneous case (cf., Fig. 3.1). This indicates, according to the numerical results of Hyun (1984) [38], that the Ekman layer disappears in the temporal range $t/T \sim 18$, which is approximatively the spin-up time scale (i.e., $\tau_{ss} \sim 13.5\ T$).

Fig. 6.14 shows a comparison between the experimental azimuthal velocity and the

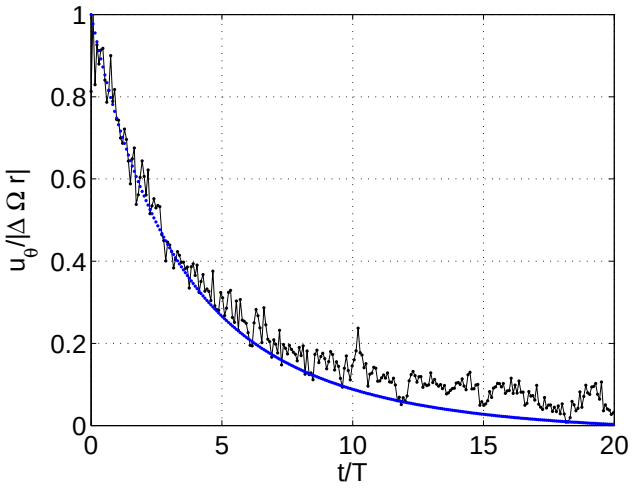

Fig. 6.14: SIDE VIEW UP 3 ($\{\epsilon, Bu\} = \{0.32, 4.34\}$) $z/H = 0.01$ - non-dimensional azimuthal velocity [–] - temporal evolution: —●— experimental results; —●— Walin's theory

Walin's theoretical prediction at $z/H \simeq 0.01$, which may be considered very close to the Ekman layer. This result is very different with respect to the comparison performed in a region located in the range $0.10 \leq z/H \leq 0.25$ (e.g., Fig. 6.8(a)). In fact, at $z/H = 0.01$ the experimental results do not decay faster than the analytical solution, and the theory is capable to reproduce properly the decay rate. This because the decrease of the azimuthal velocity is mostly due to the secondary circulation, and the viscous-diffusion effects are negligible.

Note that the theoretical curve correctly reproduces the spin-up time scale.

The local Reynolds number is $Re_{\delta_e} \simeq 312$, and thus we expect that the regime in the Ekman layer is fully turbulent. The experimental curve shows some small fluctuations, confirming that the turbulence is restricted to the Ekman layer and the instabilities of the boundary layer do not measurably disrupt the quasi-geostrophic flow, according to previous studies (e.g., Weidman (1976) [76]).

6.6 Summary

In this chapter the axisymmetric spin-up run has been deeply analyzed. The general features of the spin-up process, as the penetration depth of the secondary circulation and the radial dependence of the vortex stretching, have been experimentally confirmed.

A comparison with the analytical solution of Walin (1969) [74] for the interior azimuthal velocity has shown, according to the literature, that the experimental results decay faster, even over the shorter spin-up time scale. Only very close to the Ekman layer, the region mostly affected by the secondary circulation, the Walin's solution reproduces properly the azimuthal decay rate. These results lead credence to the hypothesis that viscous-diffusion effects arising from interior flow gradients are the cause of the discrepancy with the theory.

An attempt to improve the analytical solution by including viscous-diffusion effects via finite-different method has been proposed. In our model, we computed at each time the contribution of both secondary circulation and momentum diffusion to the decay rate of the azimuthal velocity. While the vertical diffusion equation was solved using the velocity field which keeps in account both the processes, the classical Walin's solution has been computed independently. Therefore, this procedure assumes that the secondary circulation is not affected by the viscous-diffusion process. This seems a reasonable hypothesis since the contribution of the secondary circulation is larger than diffusion over the spin-up time scale. Later in time, the secondary circulation progressively weakens as the fluid is spun-up, and it nullifies over the viscous time scale.

The numerical results show a general enhancement of the predictions. In the interior region, well away from the Ekman layer, the experimental results and our model are in good agreement, even if the Reynolds number is $\sim O(10^4)$. However, in the lower part of the rotational shear layer, where the secondary circulation is mostly located, the faster decay rate of the measurements persists. This suggest that viscous-diffusion effects may produce a feedback on the secondary circulation.

The rotational shear layer appears to be unstable, with oscillations superimposed to the basic decay trend, and the vanishing of the boundary layer has been experimentally visualized as the the fluid gradually spins-up.

Chapter 7

Unstable spin-up

We analyze here an experimental run which appears to be baroclinically unstable with non-axisymmetric disturbances in the velocity field. The results for the case characterized by the smallest Rossby number (UP 1: $\{\epsilon, Bu\} = \{0.08, 0.26\}$) have been preferred since it is closer to the condition of quasi-geostrophy assumed in the theory. Therefore, the run UP 1 is characterized by the long-wave instability in its purest form, and the nonlinearity effects associated with a non-vanishing Rossby number are secondary to the effects of baroclinic waves traveling around the turntable (Linden (1977) [45]).

7.1 Comparison to Walin's theory

SIDE VIEW Data

Fig. 7.1 shows the non-dimensional azimuthal velocity versus time in the temporal range $t/T \leq 50$ with the corresponding theoretical predictions of Walin (1969). The velocity behavior is substantially different with respect to the axisymmetric case (i.e., the run UP 3). In fact, the azimuthal velocity decay is nearly uniform in the interior region, showing only small differences between the region close to the Ekman layer (e.g., Fig 7.1(a)) and the region well away (e.g., Fig 7.1(d)). This confirms that spin-up in weakly stratified fluid (i.e., dominating rotation) is similar to the homogeneous case in so far as the attainment of solid body rotation is concerned (Siegmann (1971) [67]).

There is an initial agreement between experimental results and theoretical predictions for a time $t/T \sim 10$ after the start of the run, but the curves begin to diverge with experimental measurements decaying slower than the theory. The appearance of the discrepancies corre-

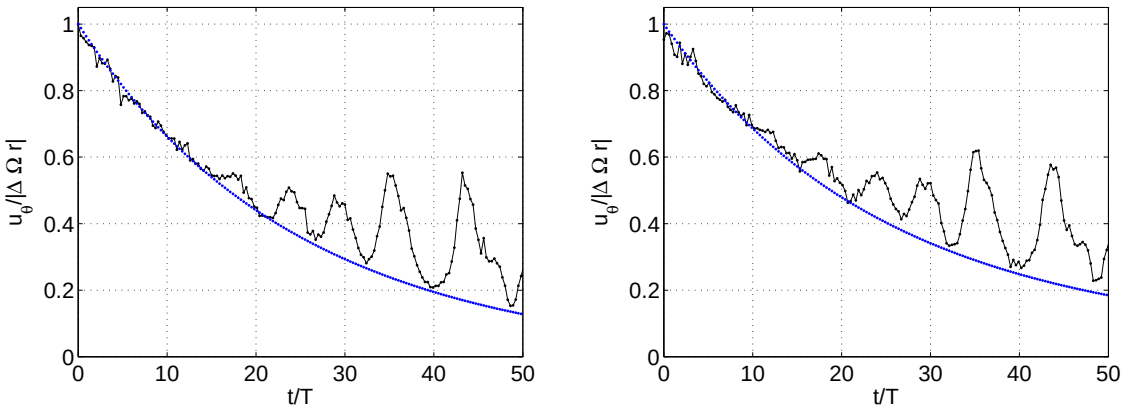

(a) $z/H = 0.20$

(b) $z/H = 0.30$

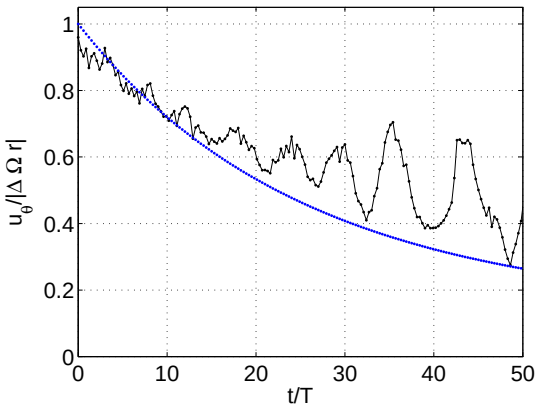

(c) $z/H = 0.40$

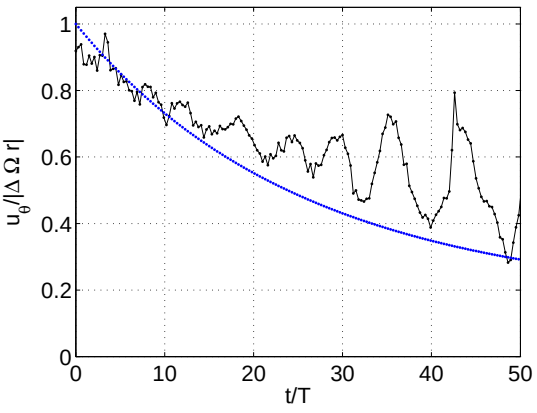

(d) $z/H = 0.50$

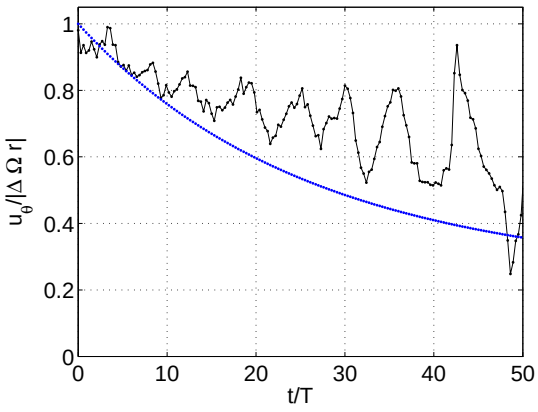

(e) $z/H = 0.70$

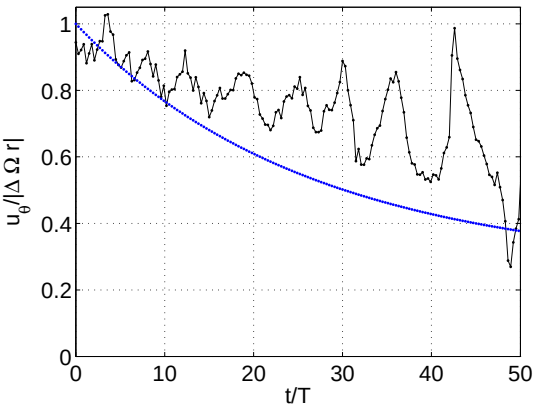

(f) $z/H = 0.90$

Fig. 7.1: SIDE VIEW UP 1 ($\{\epsilon, Bu\} = \{0.08, 0.26\}$) - non-dimensional azimuthal velocity [–] - temporal evolution at different vertical locations: —●— experimental results; —●— Walin's theory

sponds to the onset of growing oscillations associated with the long-wave instability. This contrast with the stable run UP 3 for which the experimental results decay faster than the theory after the initial agreement.

Neither experimental nor numerical analysis of azimuthal velocity were performed at

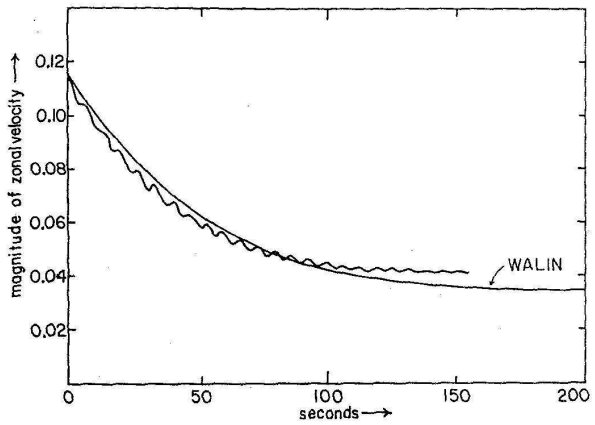

Fig. 7.2: Plot of zonal velocity versus time at mid depth and mid radius for $Bu_i = 1.76$. The tank rotation period is $T \simeq 12.2\,s$, thus $t = 100\,s \rightarrow t/T \simeq 8$. Reproduced from Barcilon *et al.* (1975) [1]

such small Burger number over a long temporal range. However, Barcilon *et al.* (1975) [1] performed a numerical simulation characterized by $Bu_i = 1.76$ (being Bu_i the Burger number calculated with the initial angular velocity) for $t/T \simeq 12$ (Fig. 7.2), and found that the Walin's theoretical solution lied below the numerical prediction, in agreement with our experimental results (UP 1: $Bu = 0.26 \rightarrow Bu_i = 0.32$). For larger Burger number they confirmed that the numerical results are located below the Walin's theoretical solution, as we found in the stable case (¶ 6.3). Note that the same trend was experienced in the work of Buzyna & Veronis (1971) [6] (cf., Fig.s 6, 10 and 11 of their paper).

Fig. 7.3 corresponds to Fig. 7.1 for a wider temporal range. The Walin's solution is generally below the experimental results until $t/T \sim 150$. From these measurements it appears that the hypothesis of Smirnov *et al.* (2005) [68] claiming that the large-scale eddies provide an additional mechanism for the vertical transport of angular momentum does not seem to be valid. In fact, in our experiment the Walin's solution, which omits the long-wave instability, is capable to correctly estimate the general decay rate. Moreover, it seems that the non-axisymmetric disturbances do not allow the fluid to reach the solid body configuration faster than the secondary circulation would perform.

Later in time ($t/T > 150$) the experimental results fall generally below the Walin's solu-

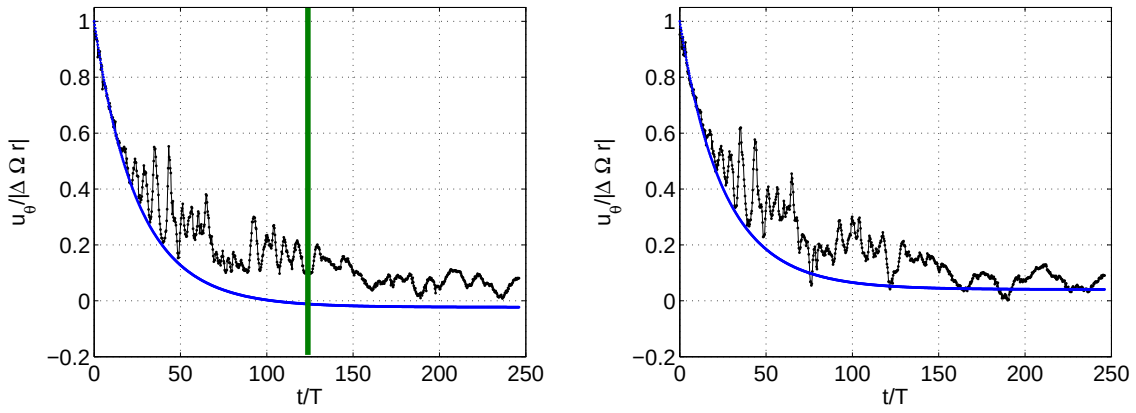

(a) $z/H = 0.20$ (b) $z/H = 0.30$

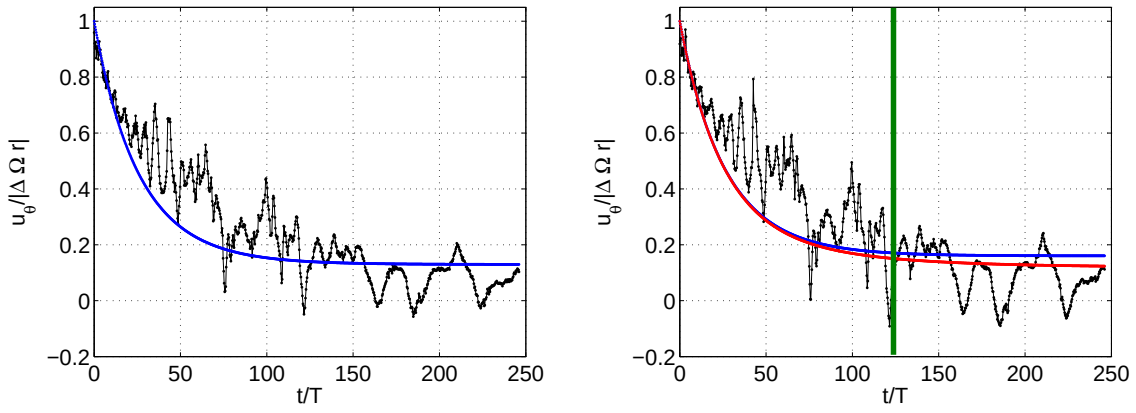

(c) $z/H = 0.40$ (d) $z/H = 0.50$

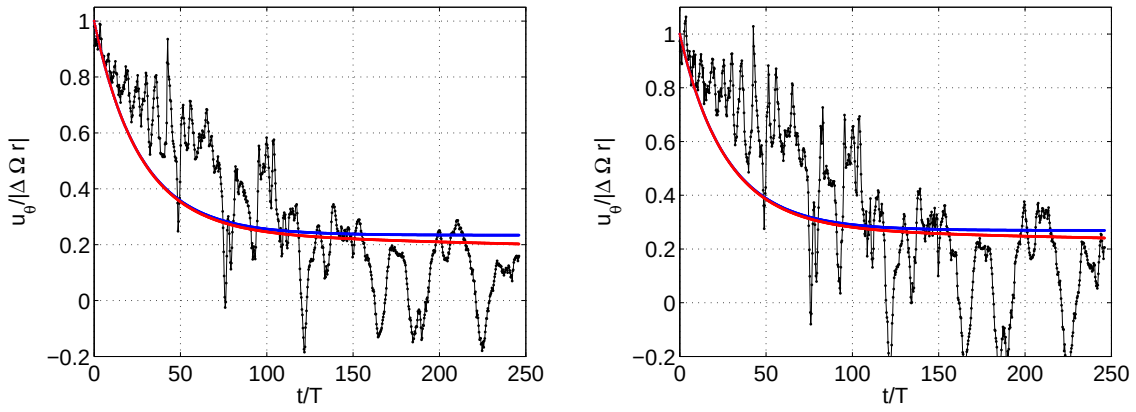

(e) $z/H = 0.70$ (f) $z/H = 0.90$

Fig. 7.3: SIDE VIEW UP 1 ($\{\epsilon, Bu\} = \{0.08, 0.26\}$) - non-dimensional azimuthal velocity [–] - temporal evolution at different vertical locations: —●— experimental results; —●— Walin's theory; —●— our model

tion, except relatively close to the Ekman layer (Fig 7.3(a)). However, this trend might be caused by the onset of other mechanisms rather than due to the long-wave instability.

Fig. 7.3 reports also the theory of Walin (1969) with the inclusion of the viscous-diffusion effects (¶ 6.4) at the upper vertical locations. It appears that the vertical diffusion of momentum does not add any contribution to the azimuthal velocity decay. Moreover, the small discrepancies between the curves due to viscous-diffusion effects is noticeable only over a time larger than the spin-up time scale (Fig. 7.3(d)). This was a predictable result: the lower Burger number states the weaker importance of stratification with respect to rotation. Therefore, the secondary circulation can penetrate deeper in the interior region, and the vertical gradients of azimuthal velocity are considerable reduced. This reflects the nearly uniform velocity decay of the experimental results in Fig. 7.3.

The spin-up time $\tau_{ss} \sim 126\ T$, computed by means of Eq.n (3.15), has been reported in Fig. 7.3(a) and 7.3(d) as a green vertical line. It appears a very good agreement with the Walin's theoretical prediction since the spin-up time coincides with the time in which the Walin's solution reaches its asymptotic value. Note that in the stable case (i.e., the run UP 3) the relatively strong stratification restricts the secondary circulation in a region adjacent to the horizontal boundary, and consequently the spin-up time is sensibly shorter. However, the bulk of the fluid adjusts to solid body rotation in the longer viscous time scale. In the unstable case (i.e., the run UP 1), the relatively weak stratification allows the secondary circulation to penetrate deeper in the interior region, and the spin-up time is longer since wider is the area in which the fluid is spun-up by the secondary circulation. However, in the run UP 1 the bulk of the fluid adjusts to solid body rotation in a shorter time with respect to the run UP 3 (cf., e.g., Fig.s 6.9(f) and 7.3(f)).

Fig. 7.4 shows the temporal evolution of the vertical profile of the azimuthal velocity. The vertical shear in the interior region is notably smaller with respect to the stable case (cf., Fig. 6.12), and the Walin's solution accurately reproduces the early time profile (Fig. 7.4(a)). Subsequently, the theoretical results decay faster than the measurements in the upper part of the fluid, while a general agreement persists in the region close to the Ekman layer. Note that in the stable case a better accordance between experiments and theory was generally found in the upper part of the fluid. Later in time, the discrepancies progressively reduces (Fig. 7.4(e)) and after $t/T \sim 120$, which correspond to the spin-up time scale, the vertical shear in the interior region nullifies (Fig. 5.4(b)). The Walin's solution is incapable to predict this behavior and we suggest that the discrepancies are due to the presence of the long-wave

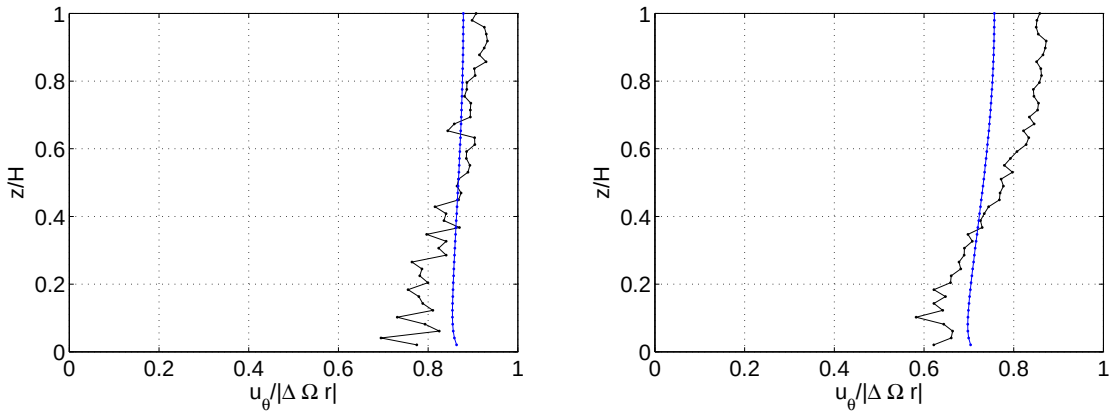

(a) $t/T = 5$

(b) $t/T = 10$

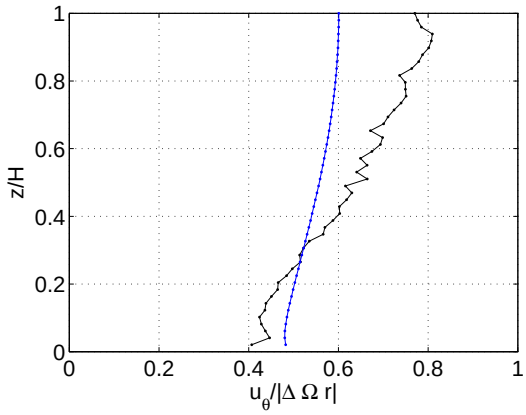

(c) $t/T = 20$

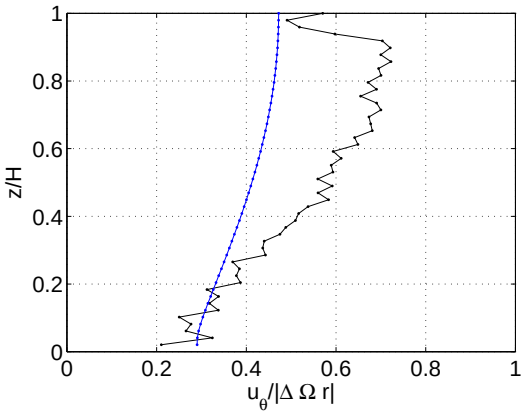

(d) $t/T = 40$

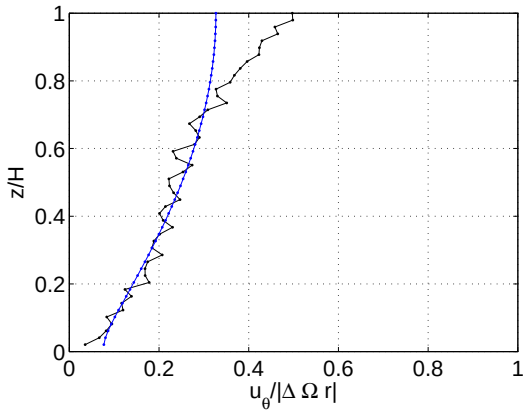

(e) $t/T = 80$

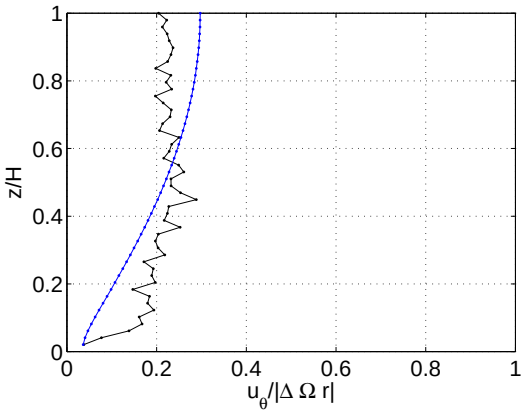

(f) $t/T = 120$

Fig. 7.4: SIDE VIEW UP 1 ($\{\epsilon, Bu\} = \{0.08, 0.26\}$) - non-dimensional azimuthal velocity [−] - vertical profile temporal evolution at different times: —●— experimental results; —●— Walin's theory

instability. Specifically, baroclinic instability acts to release the available potential energy, addressing the fluid to a state characterized by uniform azimuthal velocity in the interior region. The azimuthal velocity decay is larger than theory in the upper part of the fluid, while it is smaller in the lower part (Fig. 7.4(f)). The effect of instability is therefore equivalent as a weakening of the stratification.

7.2 Qualitative Analysis

TOP VIEW Data

Let us focus on the growth of the oscillations just after the change in the rotation rate of the tank. Fig.s 7.5 and 7.6 show the non-dimensional azimuthal velocity versus time at different radial positions and vertical locations in the temporal range $t/T \leq 50$. Note that data acquisition was begun about two rotation periods prior to the initiation of the run. The vertical locations of the horizontal laser sheet are summarized in Tab. 7.1. The levels

LEV	**vertical positions**	
	$z\ [cm]$	$z'\ [-]$
1	60	1
2	56	0.93
3	51	0.85
4	46	0.77
5	40	0.67
6	32.5	0.54
7	23	0.38

Tab. 7.1: UP 1 ($\{\epsilon, Bu\} = \{0.08, 0.26\}$) - vertical positions of the horizontal laser sheet

considered are located in the interior region, relatively well away from the Ekman layer.

These fluctuations of the azimuthal velocity appear generally correlated both radially and vertically, with some exceptions, pointing that all the measurements are performed in the area occupied by the same eddies. It appears that the oscillations are superimposed to a mean decay trend which presents the same characteristics analyzed in § 6.2: the spin-up proceeds initially more rapidly at smaller radii and decreases as the radius increases (Fig. 7.5). The amplitude of the oscillations decreases in the lower part of the fluid (Fig. 7.6).

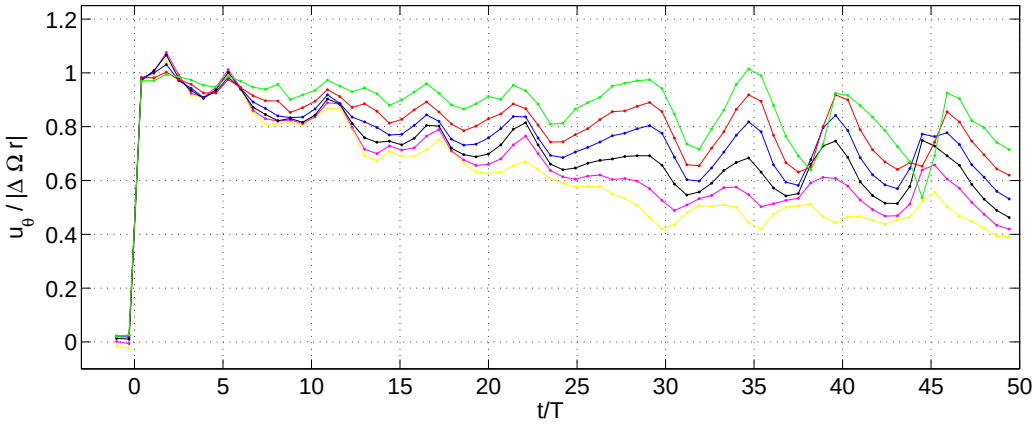

(a) level 5: $z/H = 0.67$

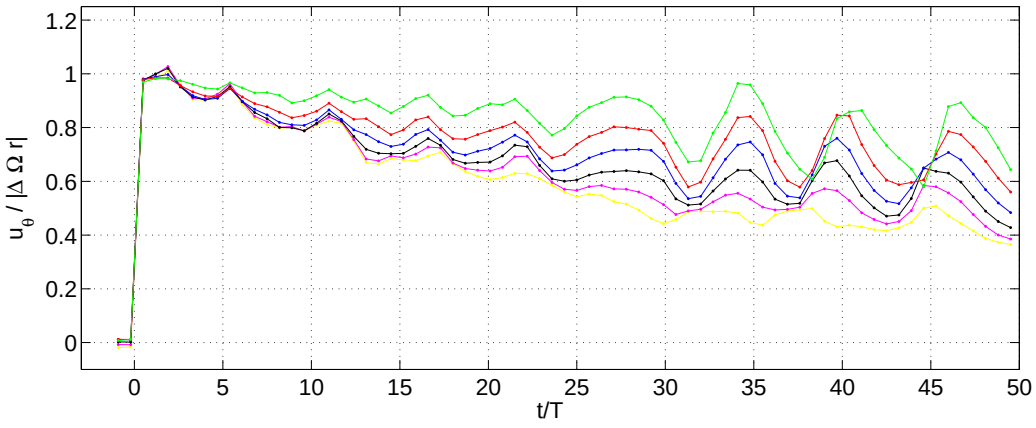

(b) level 6: $z/H = 0.54$

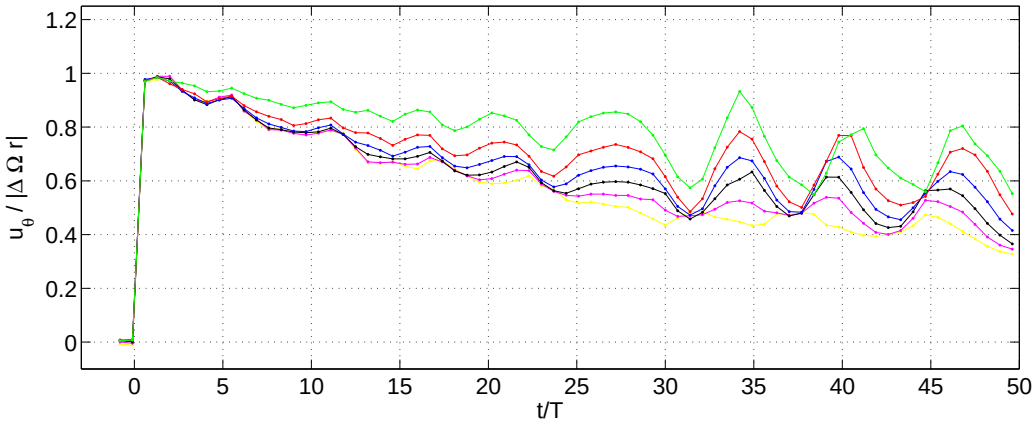

(c) level 7: $z/H = 0.38$

Fig. 7.5: TOP VIEW UP 1 ($\{\epsilon, Bu\} = \{0.08, 0.26\}$) - non-dimensional azimuthal velocity [−] - temporal evolution at different radial positions: $r/R = 0.70$; $r/R = 0.75$; $r/R = 0.80$; $r/R = 0.85$; $r/R = 0.90$; $r/R = 0.95$

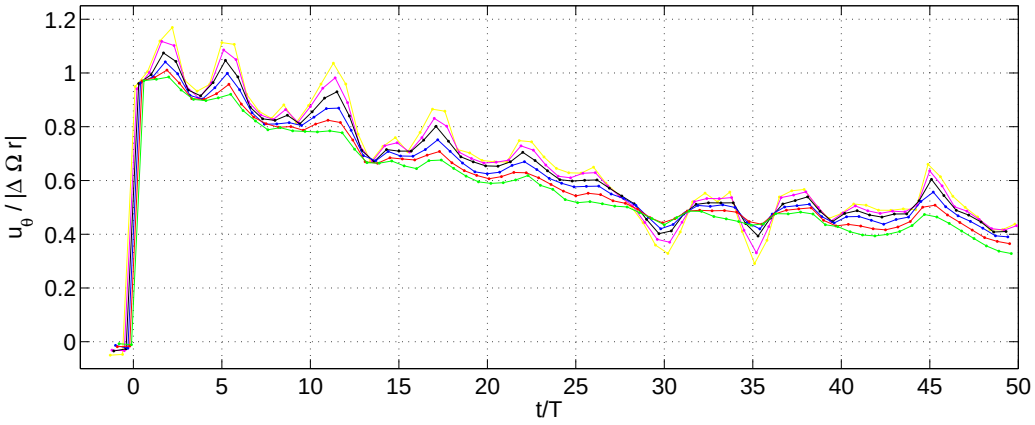

(a) $r/R = 0.70$

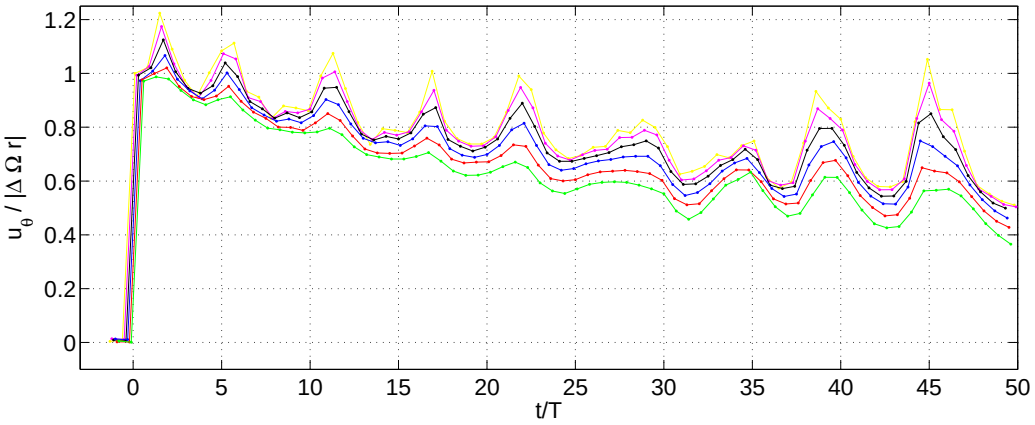

(b) $r/R = 0.80$

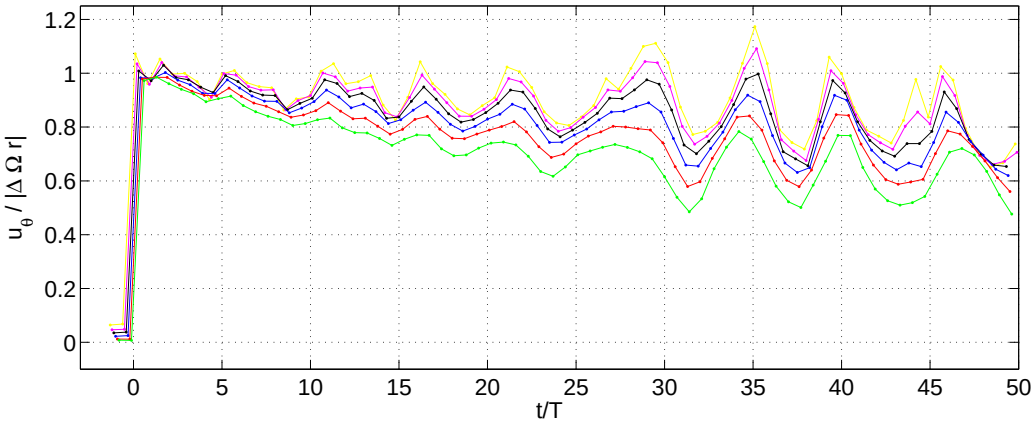

(c) $r/R = 0.90$

Fig. 7.6: TOP VIEW UP 1 ($\{\epsilon, Bu\} = \{0.08, 0.26\}$) - non-dimensional azimuthal velocity [−] - temporal evolution at different vertical locations: level 2; level 3; level 4; level 5; level 6; level 7

Smirnov *et al.* (2005) [68] reported that the beginning of the eddy formation depends on the value of the Rossby number, while it is substantially independent of the Burger number. Their data analysis showed that the formation time decreases with increasing the Rossby number. Since the run UP 1 is characterized by ($\{\epsilon, Bu\} = \{0.08, 0.26\}$), then the time of onset of eddy formation should be comparable with the corresponding in their run with parameters $\{\epsilon, Bu^1\} = \{0.10, 0.23\}$. Instead, the time of onset of the growing oscillations is $t/T \sim 1$ in the run UP 1, while they reported a time of $t/T \sim 50$ for their run. In order to deepen this discrepancy, let us highlight that Smirnov *et al.* (2005) proposed their extended Eady's model since the structure of the observed waves was not consistent with the classical Eady's model. In fact, in their runs the eddies first appeared close to the sidewall and thus they reputed necessary to include the region of lateral shear into the analysis. Initially thin boundary layers at sidewall diffuse to become shear layers sufficiently thick for the baroclinic motion within them to be essentially inviscid. The extended Eady's model thus implies that the principal factor limiting the development of the instability is the time required for the sheared sidewall layers to grow under viscous-diffusion. The formation of baroclinic cyclonic (anticyclonic) eddies during spin-up (spin-down) was attributed to the growth of sheared wall layers.

Smirnov *et al.* (2005) carried out their experiments in a cylindrical tank of radius $R = 91\,cm$: the presence of sheared sidewall layers compensates for the narrowness of the cylinder and provides a realistic estimate for the time of onset of eddies formation. Our experiments were performed in a cylindrical tank of radius $R = 650\,cm$, therefore baroclinic waves are allowed to grow with the appropriate wave structure. Moreover, the flow region affected by the sidewall layer is noticeably smaller: thus, the extended Eady's model proposed by Smirnov *et al.* (2005) is not appropriate for our experimental realization.

Before the start of the run the velocity field should be almost zero, signifying that the system is in a state of solid body rotation. Fig. 7.7(a) rather indicates that near the free surface there is a residual velocity field which gradually decreases moving towards the horizontal boundary, becoming negligible only at mid-depth (Fig. 7.7(b)). However, the azimuthal symmetry of the flow is immediately established after the impulsive change in the rotation rate of the tank, as shown in Fig. 5.6(a). We believe that this perturbation is caused by shear stresses exerted by the air on the free surface, although attention was placed to avoid this

[1] note that Smirnov *et al.* (2005) defines the Burger number as $Bu \equiv NH/fL$, and its value has been converted according our definition

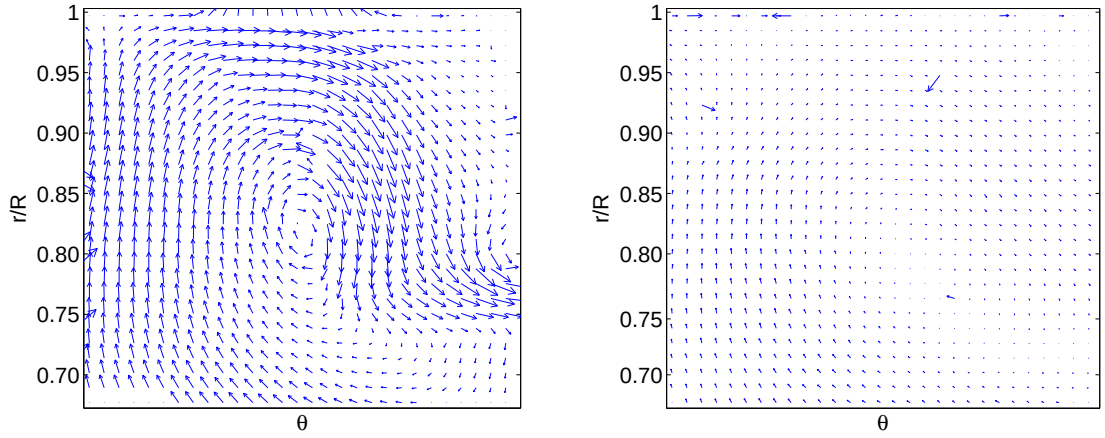

(a) level 2: $z/H = 0.93$ (b) level 6: $z/H = 0.54$

Fig. 7.7: TOP VIEW UP 1 ($\{\epsilon, Bu\} = \{0.08, 0.26\}$) - velocity field at $t/T \sim -2$

effect by means of floating foam canopy during the filling of the tank and before each run. This effect is totally lacking in the experiments of Smirnov *et al.* (2005) since they maintained the tank covered with a transparent canopy at all times. We suppose that this residual motion may play a role to explain the evidence of the almost instantaneous development of the eddies in the run UP 1 ($\{\epsilon, Bu\} = \{0.08, 0.26\}$), at variance with Smirnov *et al.* (2005), who reported a time $t/T \sim 50$ for a run with comparable Rossby and Burger numbers.

7.3 Quantitative Analysis

TOP VIEW Data

It seems reasonable that the long-wave disturbances are due to the onset of the baroclinic instability, but the nature of the fluctuations must be determined quantitatively. Note that the *Richardson number* [2] is large ($Ri \simeq 60$), thus the instability is not due to turbulence induced by a strong vertical shear (see, e.g., Cushman-Roisin (1994) [10]).

Although the comparison of the spatial profile evolution of the azimuthal velocity (Fig.s 7.5 and 7.6) is clearly not suitable to study the instability pattern, it may give insight on the instability properties. Fig. 7.8(a) reports a comparison of the azimuthal velocity versus time at $\{r/R, z/H\} \simeq \{0.85, 0.75\}$ between the stable (i.e., UP 3 $\{\epsilon, Bu\} = \{0.32, 4.34\}$) and the unstable

[2] the *bulk* Richardson number, $Ri \equiv N^2/(\mathrm{d}U/\mathrm{d}z)^2$ indicates the relative importance of stratification to the vertical shear of the horizontal velocity

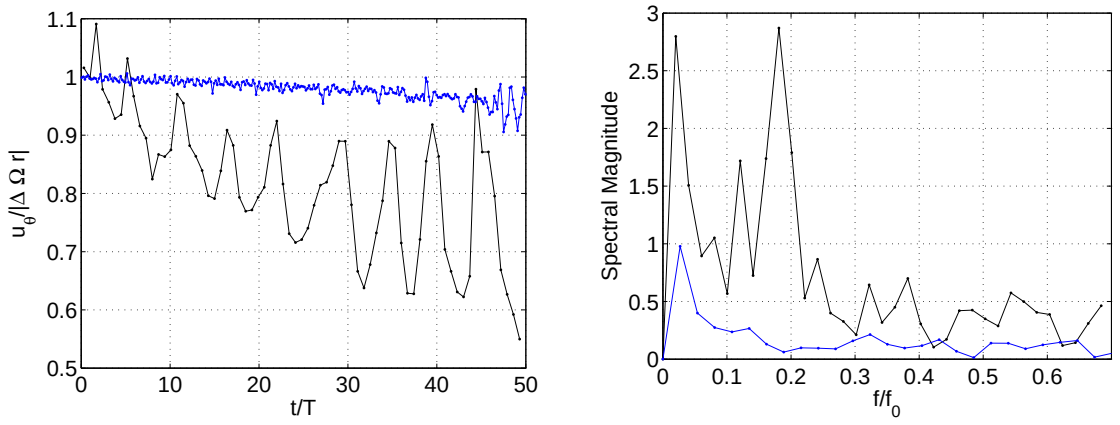

(a) temporal evolution

(b) Fourier transform

Fig. 7.8: TOP VIEW $\{r/R, z/H\} \simeq \{0.85, 0.75\}$: non-dimensional azimuthal velocity [-] - —●— UP 1 ($\{\epsilon, Bu\} = \{0.08, 0.26\}$); —●— UP 3 ($\{\epsilon, Bu\} = \{0.32, 4.34\}$)

(i.e., UP 1 $\{\epsilon, Bu\} = \{0.08, 0.26\}$) runs. The temporal Fourier spectrum (Fig. 7.8(b), being $f_0 = 1/T$ the rotation frequency) is not well defined since, aside from noise, the oscillations are superimposed to a mean decay trend. However, the Fourier transform allows to investigate the temporal characteristics of the instability, showing that the azimuthal velocity in the run UP 1 oscillates with a frequency $f/f_0 \simeq 0.18$. This frequency corresponds to an oscillation period $t/T \sim 5.52$, confirming that the azimuthal flow becomes unstable forming large periodic eddies. In agreement, Smirnov *et al.* (2005) [68] reported the development of the instability in form of eddies of regular low-frequency oscillations $f/f_0 \sim 0.2$ for the run characterized by comparable Rossby and Burger numbers.

In order to estimate the wavelength of the instability, the azimuthal velocity was averaged in small boxes such as that they had the same radial coordinate, but were separated from each other by a given distance in the azimuthal direction, as sketched in Fig. 7.9. Fig. 7.10(a) shows the azimuthal velocity temporal profile: the phase shift between the two curves is caused by the time an eddy takes to travel from one box to the other. Each thick line in Fig. 7.10(a) is the corresponding fit of the minima, with no direct physical meaning. However, in order to enlighten the amplitude of the oscillations we removed the decay trend obtained in this way from the velocity field. Fig. 7.10(b) shows the growing of the oscillation due to baroclinic instability in the temporal range $t/T \leq 50$. The corresponding temporal Fourier transform (Fig. 7.11(a)) confirms the previous result of a perturbation with frequency $f/f_0 \simeq 0.18$. The cross-correlation function (Fig. 7.11(b)) allows to know the relative time between the two

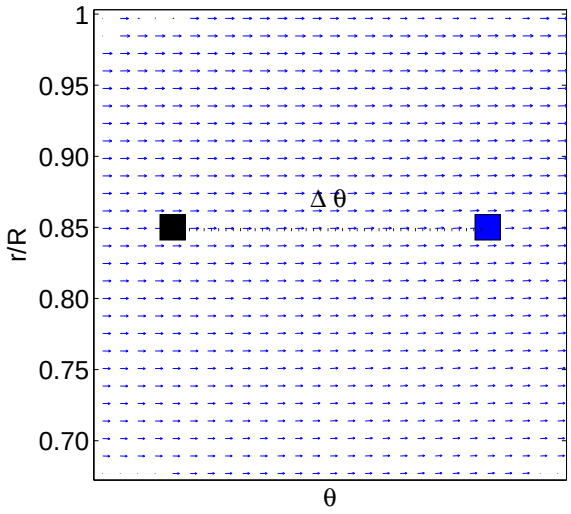

Fig. 7.9: Sketch of the two boxes configuration on the horizontal laser sheet: boxes b1 —●— and b2 —●— are positioned at $r/R = 0.85$ and separated some distance in the azimuthal direction, with the box b1 being upstream

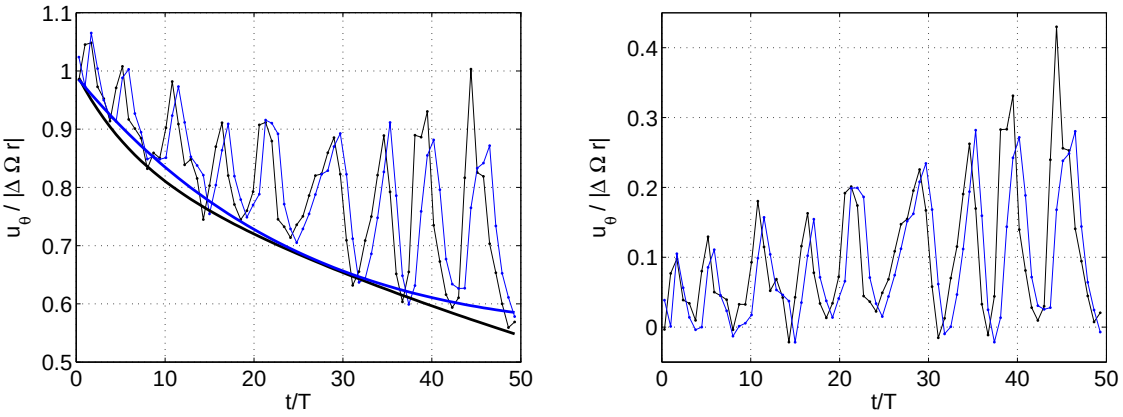

(a) temporal evolution (b) oscillation growing

Fig. 7.10: TOP VIEW $\{r/R, z/H\} \simeq \{0.85, 0.75\}$ UP 1 ($\{\epsilon, Bu\} = \{0.08, 0.26\}$): non-dimensional azimuthal velocity [-] - boxes b1 —●— and b2 —●—

curves, $\Delta t/T = 0.7$.

Knowing the frequency of the signal as well as the time spent by the perturbation to move between the two boxes, we estimated the wave number of the instability. Referring to Fig. 7.9, ($\Delta\theta$ such as $\Delta\theta_r = \pi/12$ *rad*, see ¶ 4.5.2), let us assume a perturbation of form analogous to Eq.n (2.40). This is possible since, locally, the polar frame of reference may be considered as a cartesian frame of reference, with the radial and azimuthal axis coincident

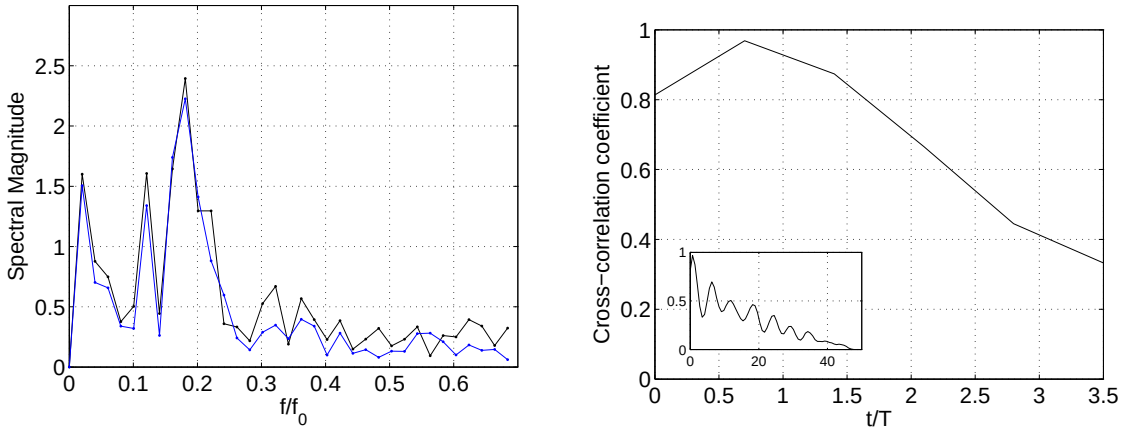

(a) Fourier transform

(b) Cross-correlation function

Fig. 7.11: TOP VIEW $\{r/R, z/H\} \simeq \{0.85, 0.75\}$ UP 1 ($\{\epsilon, Bu\} = \{0.08, 0.26\}$): boxes b1 —●— and b2 —●—

with the y and x axis, respectively. In this approximation, the perturbation of the interior pressure field may be written (in non-dimensional variables) as

$$\phi' = |A'|e^{k'c_i't'}\cos(k'\theta_r - \omega't' + \alpha')\cos l'_m r' \tag{7.1}$$

where $k' = kL$, $\omega' = \omega T$, $l'_m = (m + 1/2)\pi$.

At a fixed vertical location holds the relation

$$k'\Delta\theta_r = \omega'\Delta t' \tag{7.2}$$

and since $\omega' = 2\pi\ f/f_0$ then

$$k' = 2\pi\frac{f}{f_0}\frac{\Delta t'}{\Delta\theta_r} \simeq 3.04$$

The non-dimensional zonal wave number k' provides the number of eddy pairs in the system. Fig. 7.12 shows a sketch of the instability pattern predicted: three pairs of cyclones and anticyclones advected in the anticyclonic direction by the basic flow. The corresponding dimensional zonal wave number is $k = k'/L \simeq 0.47\ m^{-1}$, and hence the dimensional wavelength is $\lambda = 2\pi/k \simeq 13.43\ m$. The dimensional perturbation period is $T_p = 1/f \simeq 276.25\ s$ ($T_p/T \sim 5.52$).

The theoretical growth rate is expressed by Eq.n (2.38). In non-dimensional variables it takes the form

$$k'c_i' = \frac{k'}{\mu'}\left[\left(\coth\frac{\mu'}{2} - \frac{\mu'}{2}\right)\left(\frac{\mu'}{2} - \tanh\frac{\mu'}{2}\right)\right]^{1/2}$$

(being $\mu' = (k'^2 + l'^2_m)Bu$) displayed in Fig. 7.13 for the most unstable radial mode ($m = 0$).

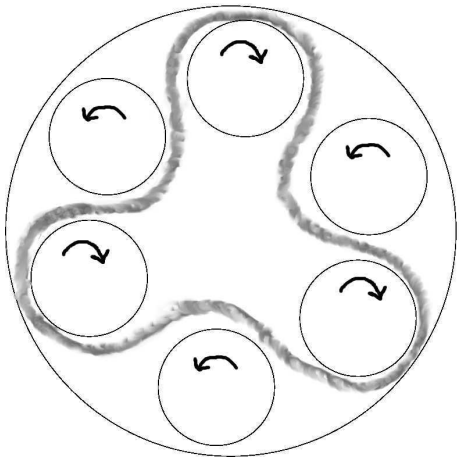

Fig. 7.12: Sketch of the instability pattern as predicted by the Eady's model.

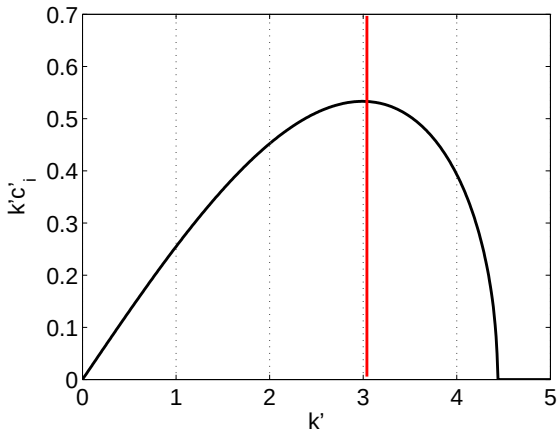

Fig. 7.13: UP 1 ($\{\epsilon, Bu\} = \{0.08, 0.26\}$): —●— the growth rate $k'c_i'$ [−] for the most unstable radial mode; —●— experimental wave number

The red line, indicating the experimental measurement, corresponds almost exactly with the maximum in the growth rate, suggesting a very good agreement with the theoretical wave number predicted by the Eady's model.

Note that Kanda (2004) [40] reported that the growth rate is not uniform, and the eddies differ in size. Once they are fully grown, larger eddies grow further by catching up with smaller one and merging them. This later phase of vortex coalescence goes beyond the scope of this thesis.

The growth rate predicted by the Eady's model does not match with the experimental results, but it appears to be one order of magnitude larger than the optimal one. Note

that the classical Eady's model assumes a linear vertical profile in the azimuthal velocity as initial condition. In our experiments, the fluid is approximatively in solid body rotation just after the change in the rotation rate of the tank (cf., Fig. 5.3), and the vertical profile evolves in time. In axisymmetric case (i.e., the run UP 3), the fluid interior reaches in the spin-up time scale an azimuthal velocity linear vertical profile in the rotational shear layer (cf., Fig. 6.12). In non-axisymmetric case (i.e., the run UP 1), this process is weakened by the deeper penetration of the secondary circulation and altered by the appearance of baroclinic instability at early times (cf., Fig. 7.4).

Smirnov *et al.* (2005) [68] derived the Eady's model in cylindrical geometry, using rather as initial condition a linear vertical profile in the rotational shear layer. This is an appropriate initial condition for their experimental configuration since the formation of large eddies is experienced after the spin-up time scale. Note that now we consider the derivation of the Eady's model by Smirnov *et al.* (2005) without the inclusion of the sidewall boundary layer. The boundedness along the azimuthal direction sets discrete wave numbers $k'_n = n$ ($n = 1, 2, 3, \ldots$), and the Eady's condition for instability is (cf., Eq.n 15 of their paper)

$$nc'_i = 2\pi\epsilon\, Bu \left[\frac{1}{X} \left(\coth X - \frac{1}{X} \right) - \frac{1}{4} \right]^{1/2} \tag{7.3}$$

being $X \equiv NK_nH/2\Omega$ such as $J_n(K_nR) = 0$, where J_n is the n-order Bessel function. The

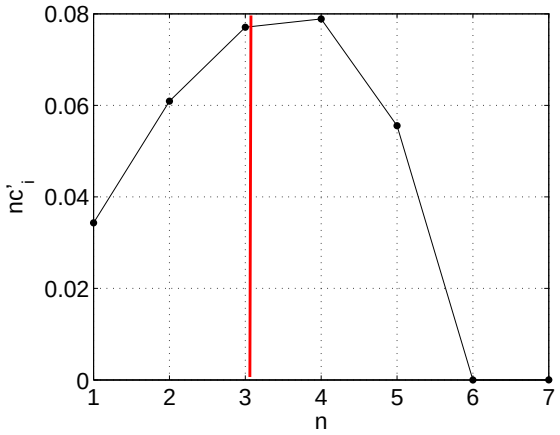

Fig. 7.14: UP 1 ($\{\epsilon, Bu\} = \{0.08, 0.26\}$): —●— the growth rate $n'c'_i$ [−] for the most unstable radial mode as derived by Smirnov *et al.* (2005) [68]); —●— experimental wave number

theoretical growth rate expressed by Eq.n 7.3 is showed in Fig. 7.14 for the most unstable radial mode (the first zero of the Bessel function). The most rapidly growing waves are

characterized by $n = 3$ and $n = 4$, in accordance with the experimental results, while the growth rate is one order of magnitude less than the predictions of the classical Eady's model. Moreover, keeping into account that in the run UP 1 the vertical shear in the azimuthal velocity is almost half than the assumption of Smirnov *et al.* (2005) at the appearance of the instability, we suggest to divide by two their prediction, which indicates $nc_i' \simeq 0.075$ for $n = 3$. This is a reasonable procedure since the growth of the oscillations is controlled by the available potential energy, and the horizontal density gradient is proportional to the vertical shear. Fig. 7.15 reports the growing oscillations in the range $t/T \leq 50$ and the growth trend

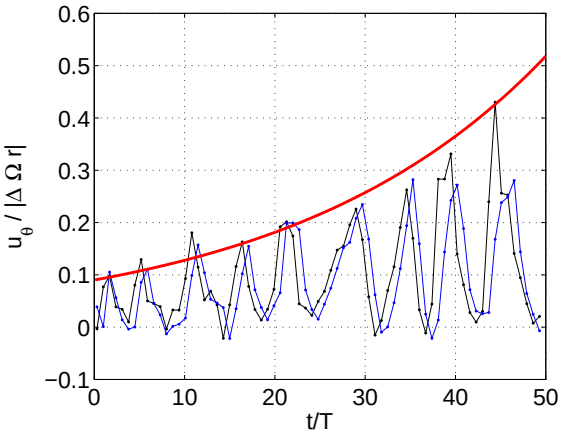

Fig. 7.15: Fig. 7.10(b) with the growth trend —●— computed by means of Eq.n 7.4

$$A' = A'_0 \, e^{k' c_i' t'} \tag{7.4}$$

being $nc_i' = 0.035$ and $A'_0 = 0.09$. A good agreement is indeed obtained using the derivation of Smirnov *et al.* (2005) and considering the actual vertical shear.

7.4 Basic Flow and Fluctuations

TOP VIEW Data

The azimuthal velocity field in the temporal range $t/T \leq 50$ was interpreted as a composition of two distinct physical processes. The flow is dominated by an anticyclonic current, generated by the change in the angular velocity of the tank, which adjusts in time to the new angular velocity of the boundaries. A series of long-waves oscillations of average period $t \simeq 276.25\ s$ are superimposed to the basic fluctuation-free state. The knowledge of the

oscillation period allows to separate the basic anticyclonic velocity field from the velocity fluctuation field characteristic of the instability. The sampling time (5 s) provides a measurement periodicity of 35 s for each horizontal level, indicating that each oscillation contains about eight bursts. A 1-period central moving average algorithm was used as low-frequency band pass filter. This tool removes the short term fluctuations leaving only the long term trend due to the anticyclonic current. This velocity field has filtered out the velocity associated with the fluctuations and defines an observed mean flow state. It cannot be considered the basic flow since it implicitly assumes the existence of fluctuations (Pedlosky (1987) [58]). The velocity fluctuation field is then obtained by subtracting the observed mean velocity field from the original velocity field. This procedure may compensate the absence of dye visualization which would allow to know qualitatively the instability pattern.

In order to check the accuracy of the procedure, the temporal evolution of the original

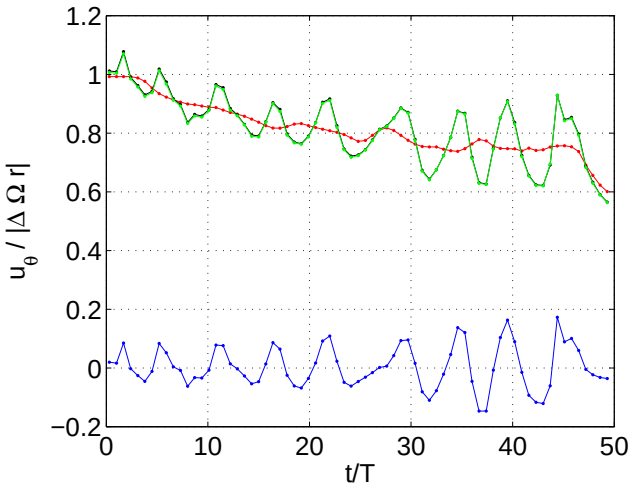

Fig. 7.16: TOP VIEW $\{r/R, z/H\} \simeq \{0.85, 0.75\}$ UP 1 ($\{\epsilon, Bu\} = \{0.08, 0.26\}$) - non-dimensional azimuthal velocity - temporal evolution: original velocity —●—; basic flow —●— and fluctuation —●— obtained by means of moving average tool; —●— reconstructed original flow. The —●— and —●— results are almost coincident.

velocity field is then reconstructed and compared to the original one. The agreement is excellent at each time in the range considered. Fig. 7.16, which reports such a comparison at $\{r/R, z/H\} \simeq \{0.85, 0.75\}$, may be considered representative of the whole domain. We are therefore allowed to study the instability pattern by means of the moving average tool. Fig. 7.16 confirms that the fit of the minima removed from the original velocity field in ¶ 7.3 had no physical meaning: note that it was used only to enlighten the fluctuation trend.

7.5 Visualization of the Instability Pattern

TOP VIEW Data

Considering a series of velocity fluctuation fields corresponding to the same oscillation, the first field is taken as a reference and the subsequent ones are suitably shifted along the azimuthal direction of a distance

$$\Delta\theta = \frac{\omega'}{k'} R \Delta t'$$

(cf., Eq.ns (4.6) and (7.2)), being $\Delta t'$ the time interval between the first velocity fluctuation field and the considered subsequent one. Velocity fluctuation fields belonging to the same vertical location are then merged together in order to obtain a series of *extended* velocity fields, one for each level, which allow to reconstruct the horizontal perturbation pattern at an arbitrary time. The procedure is illustrated and detailed in Fig. 7.17. Since all the fields are suitably shifted, the series of merged velocity fluctuation fields may permit to investigate the vertical profile of the perturbation.

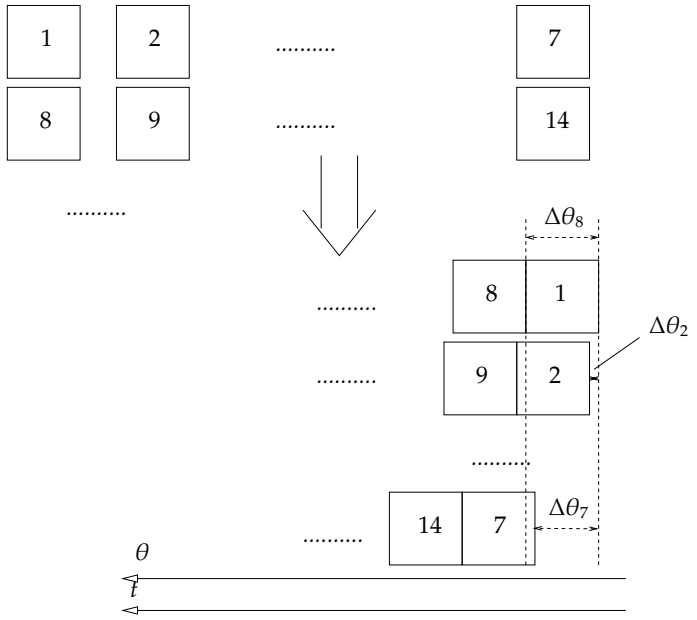

Fig. 7.17: Shifting and merging field procedure. Let us imagine a series of velocity fluctuation fields corresponding to the same oscillation, sketched by the squares on the top of figure. The first field belongs to the first horizontal level, and so on until the seventh field. The fields belonging to the same horizontal level are suitably shifted and merged together as to generate extended velocity field representative of the whole oscillation. In the example on the bottom of figure $\Delta\theta_i$ is the shift along the azimuthal direction which corresponds to the time interval between the first velocity fluctuation field and the considered subsequent one, named *i*. This procedure originates a narrow overlap region between the fields merged.

We obtained nine velocity fluctuation fields corresponding to the velocity oscillations in the temporal range $t/T \leq 50$. Fig. 7.18 displays the most representative vorticity fluctuation fields at $z/H \simeq 0.92$ (second level). Note that in the overlap regions the grid points do not perfectly coincide, generating a splitting effect in the vorticity field. We did not reverse the azimuthal velocity in these extended fields (¶ 4.5), and therefore anticyclonic (cyclonic) patterns in the vorticity field correspond to positive (negative) fluctuations in the observed evolution of the azimuthal velocity (e.g., Fig. 7.8(a)). Along the abscissa we consider the azimuthal variable, and the time increases from right to left, since the flow located upstream will cross afterwards the horizontal laser sheet. The value of the azimuthal variable was reported since it allows to obtain time information on the structure of the instability. Bearing in mind Eq.ns (4.6) and (7.2)

$$\Delta t' = \frac{k'}{\omega'} \frac{\Delta\theta}{R}$$

Then, as example, $\Delta\theta = 100$ *rad* corresponds to $\Delta t' \simeq 0.41 \rightarrow \Delta t \simeq 20.6$ *s*.

Fig. 7.18 allows to visualize the development of the baroclinic instability. During the first oscillation (Fig. 7.18(a)) cyclonic and anticyclonic vorticity patterns present a small extension and are alternated in the flow field. Fig. 7.18(b) shows the formation of positive vorticity near the sidewall due to the radial shear of the interior velocity. This stage is followed by extension and organization of the eddies, while strong cyclonic vortices appear at the sidewall (Fig. 7.18(c)). During the seventh oscillation (Fig. 7.18(d)) the baroclinic instability appears to be wholly developed, with a large anticyclone centered in the vorticity field. Note that the azimuthal range considered along the abscissa is $\Delta\theta \simeq 1100$, which corresponds to $\Delta\theta_r \simeq 2\pi/k'$, being $k' = 3$ the experimental wave number. Therefore, the range along the azimuthal direction is of the order of the experimental wavelength of the perturbation, and Fig. 7.18(d) clearly shows one cyclone-anticyclone pair moving around the flow domain (the whole anticyclone and two half cyclones are displayed).

Note that in the lateral boundary layer the cyclones induced by the horizontal shear follow to grow in size, and finally detach from the sidewall (Fig. 7.18(e)). We suggest that this mechanism could be responsible for the faster decay of the azimuthal velocity over long time, as evinced from Fig. 7.3. Therefore, the radial transport of momentum may play a role in explaining the complex dynamics of the spin-up in weakly stratified fluid (i.e., dominating rotation).

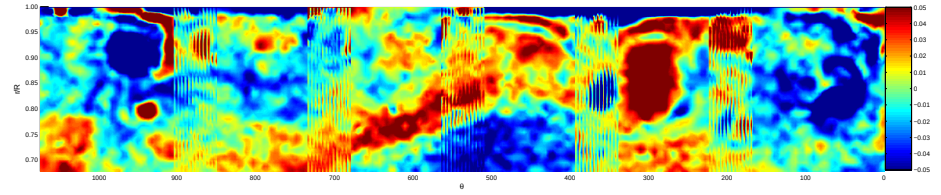

(a) first oscillation $t/T \simeq 1$

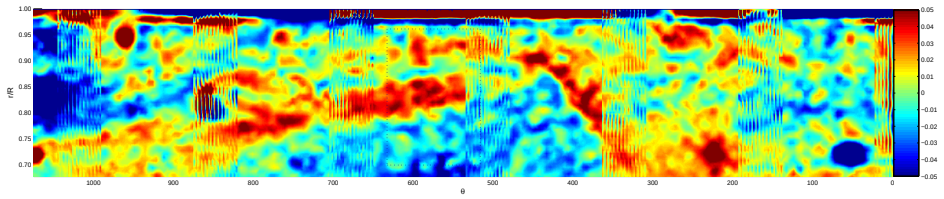

(b) third oscillation $t/T \simeq 10$

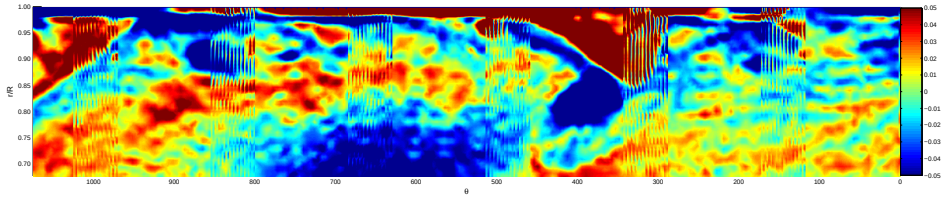

(c) fifth oscillation $t/T \simeq 20$

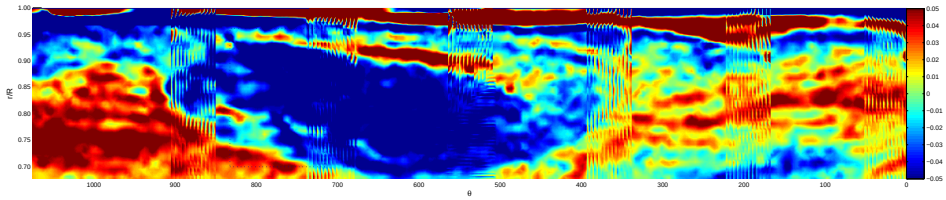

(d) seventh oscillation $t/T \sim 35$

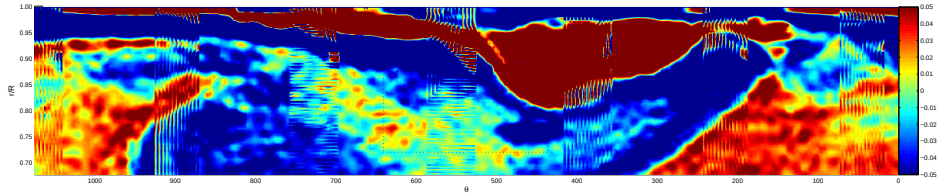

(e) ninth oscillation $t/T \sim 45$

Fig. 7.18: TOP VIEW UP 1 ($\{\epsilon, Bu\} = \{0.08, 0.26\}$) - level 2 - vorticity fluctuation fields.

7.6 Information on Phase and Amplitude

TOP VIEW Data

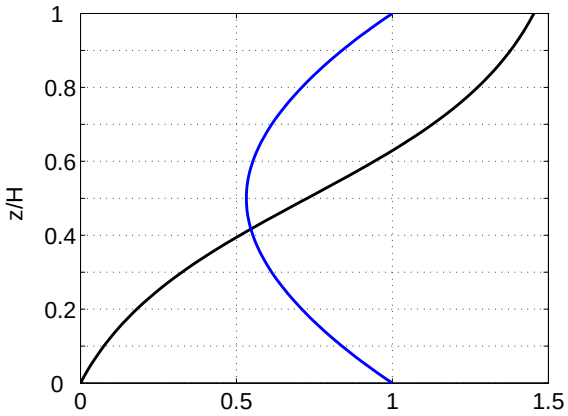

Fig. 7.19: UP 1 ($\{\epsilon, Bu\} = \{0.08, 0.26\}$): vertical profile - the phase —●— and the amplitude —●— for the most unstable wave.

Fig. 7.19 shows the non-dimensional wave amplitude $|A'|$ and phase α' as function of the non-dimensional height for the most unstable wave, characterized by $k' \simeq 3$. Note that the non-dimensional form of Eq.ns (2.39) and (2.41) is

$$A'(z') = \cosh \mu' z' - \frac{\sinh \mu' z'}{\mu' c'}$$

$$\alpha'(z') = \arctan\left[\frac{2c'_i \sinh \mu' z'}{2\mu'|c'|^2 \cosh \mu' z' - \sinh \mu' z'}\right]$$

The theory predicts that the amplitude of the disturbance is symmetric about the mid-depth, where it attains its minimum value. The phase is an increasing function of z', and thus the orientation of the lines of constant phase is against the basic flow, precisely opposite to the direction a passive tracer would be tilted by the shear flow. The wave at $z' = 0$ leads the wave field at $z' = 1$ by very nearly $\pi/2$ *rad*, i.e., the crests and troughs of the perturbation pattern at the upper level lag the bottom wave by nearly 90°. In fact, the increase of α' with z' implies the tilting rearward of the waves with height. It may be shown that this is precisely the condition for the baroclinic conversion of energy from the basic flow to the perturbations (Pedlosky (1987) [58]).

Fig.s 7.20 and 7.21 report anticyclonic and cyclonic eddies extracted by the perturbation field corresponding to the first oscillation at different vertical locations. Note that the

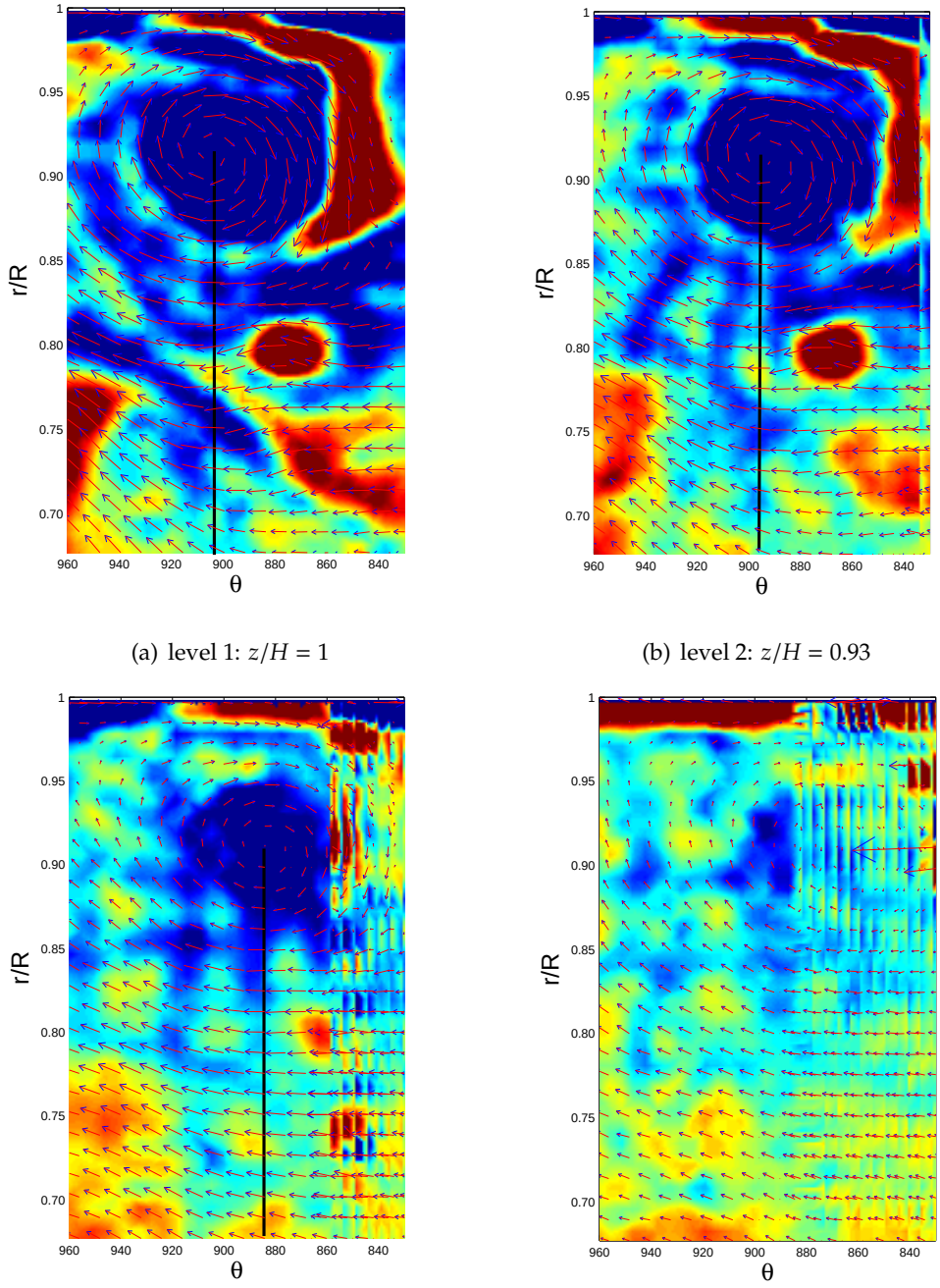

(a) level 1: $z/H = 1$

(b) level 2: $z/H = 0.93$

(c) level 3: $z/H = 0.85$

(d) level 4: $z/H = 0.77$

Fig. 7.20: TOP VIEW UP 1 ($\{\epsilon, Bu\} = \{0.08, 0.26\}$): anticyclone extracted from the perturbation field of the first oscillation. The legend is the same of Fig. 7.18

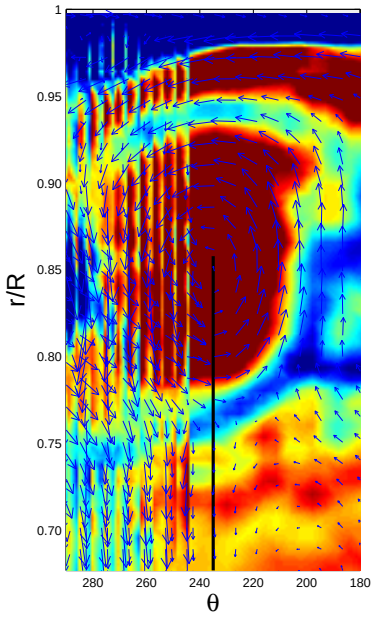

(a) level 1: $z/H = 1$

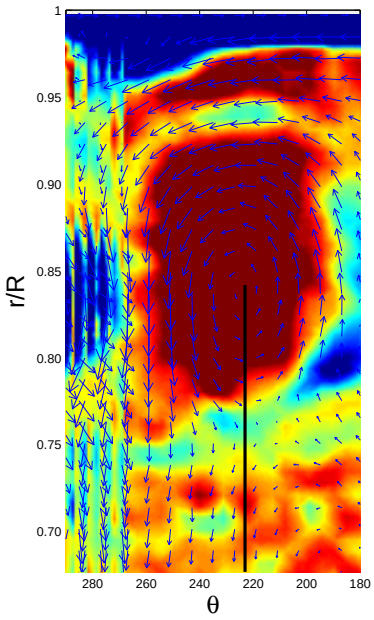

(b) level 2: $z/H = 0.93$

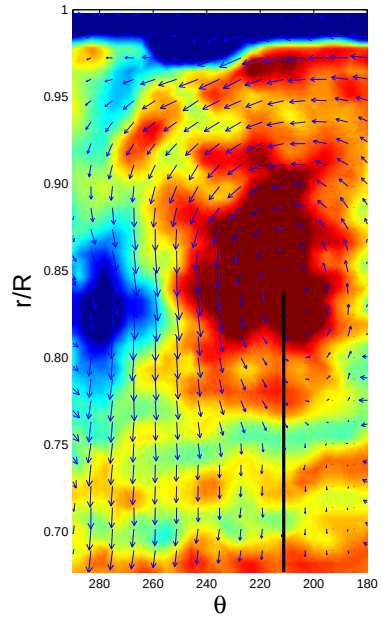

(c) level 3: $z/H = 0.85$

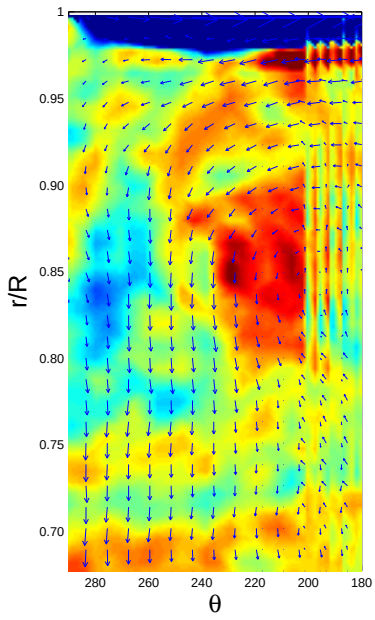

(d) level 4: $z/H = 0.77$

Fig. 7.21: TOP VIEW UP 1 ($\{\epsilon, Bu\} = \{0.08, 0.26\}$): cyclone extracted from the perturbation field of the first oscillation. The legend is the same of Fig. 7.18

perturbation field at the second level is reported entirely in Fig. 7.18(a). Only the first four levels were considered since the vorticity intensity decreases approaching mid-depth, and the instability structures are no more recognizable in the perturbation field moving further in deep. This is in agreement with the theoretical vertical profile of the wave amplitude; however, since the linear theory is incapable of determining the amplitude of the disturbance, no further information can be obtained.

In Fig.s 7.20 and 7.21 a black line approximatively indicates the center of the vortices, but the overlap region does not allow to precisely individuate it in the fourth level. Fig. 7.22 shows the vertical profile of the phase, as predicted by the theory, in the range $0.85 \leq z/H \leq 1$, which pertains to the horizontal levels considered. It provides $\Delta\alpha' \simeq 0.12$ between the first and the third level, and the relation (7.1) states (chosing θ_r as independent variable)

$$\Delta\alpha' = k'\Delta\theta_r \tag{7.5}$$

Thus, the theoretical phase suggests an azimuthal separation of the instability structures

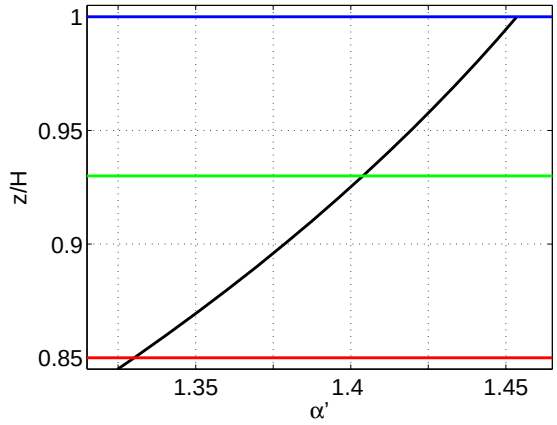

Fig. 7.22: UP 1 ($\{\epsilon, Bu\} = \{0.08, 0.26\}$): vertical profile in the range $0.75 \leq z/H \leq 1$ of the phase for the most unstable wave. The vertical location of the three first levels is indicated: —●— level 1; —●— level 2; —●— level 3

between the first and the third level of $\Delta\theta_r \simeq 0.04\ rad$, which corresponds to $\Delta\theta \equiv R\Delta\theta_r \simeq 26$. In Fig.s 7.20 and 7.21 the azimuthal separation of the center of the eddies between the levels considered is, respectively, $\Delta\theta \simeq 20$ and $\Delta\theta \simeq 25$. Therefore, although the procedure is not rigorous, the measurements point to the same order of magnitude predicted by the theory.

7.7 Summary

In this chapter the long-wave instability, leading to non-axisymmetric spin-up, has been investigated in detail. The results for the run characterized by the smallest Rossby number have been presented in order to best approach the quasi-geostrophic dynamics.

In spite of the instability, the Walin's solution turns out to provide a reasonable prediction of the decay trend. However, the experimental decay is slower than the theory, pointing that the large scale eddies do not provide an additional mechanism for the transport of angular momentum, as suggested by Smirnov *et al.* (2005) [68].

It has been confirmed that the viscous-diffusion effects are related to the penetration of the meridional circulation. In fact, in the weakly stratified run considered it appears that the secondary circulation affects the whole fluid, and the viscous-diffusion effects do not add a significant contribution to the decay rate of the azimuthal velocity.

The measurements indicate that the *extended* Eady's model proposed by Smirnov *et al.* (2005) is not applicable to our experimental realization. The baroclinic eddies do not first appear close to the sidewall, and their time of onset is not delayed. The large-scale dimension of the facility allows the waves to attain the appropriate structure, and the effects of the wind stress may play a role to enhance their development.

A quantitative comparison with the classical Eady's model has shown a good agreement, and both the wavelength of the most unstable wave and the vertical dependence of the phase have been favorably compared with theory. However, the growth rate appears to be one order of magnitude larger than the optimal one. The growth rate derived by Smirnov *et al.* (2005) in cylindrical geometry, without the inclusion of the sidewall boundary layer, has been optimized in order to keep in account the actual initial shear in the azimuthal velocity. This growth rate fits properly with the experimental results, and the mechanism of baroclinic instability becomes the most plausible explanation for the existence of the observed long-wave instability in spin-up process.

Since the analysis of the spatial structure of the flow was flawed, we removed the observed mean flow and displayed the perturbation field associated with the baroclinic instability. Series of extended vorticity fluctuation fields have shown that the instability mechanism is well developed after $t/T \sim 40$. Moreover, the formation of strong penetrative cyclonic vortices at the sidewall suggests the involvement of the radial transport of momentum over long time scales.

Chapter 8

Conclusions

In this thesis an experimental investigation of stratified spin-up and spin-down has been presented. The experiments were performed in the large rotating tank of the Coriolis-LEGI laboratory, with linear density stratification over flat bottom. The runs differ in the change of the rotation rate and in the final rotation of the tank, while the background stratification was kept constant. The theory of stratified spin-up relies on a multi-timing treatment which reflects the existence of three separated time scales. In a time $t \sim \Omega^{-1}$ an Ekman layer develops and becomes quasi-steady on the horizontal boundary. In the rotational shear layer, where the secondary circulation is located, the fluid is spun-up to the final rotation rate of the container in a time $t \sim \Omega^{-1}E^{-1/2}$. Finally, at very large time $t \sim \Omega^{-1}E^{-1}$, viscous diffusion has affected the whole interior region and the fluid adjusts to solid body rotation. We set a very small Ekman number ($E \sim O(10^{-5})$) as to obtain a good separation between these time scales in order to properly analyze the flow behavior over the spin-up time scale. The non-dimensional parameters important in determining the observed response are the Burger and Rossby numbers. We have considered the case of small Rossby number ($\epsilon \leq 0.3$), corresponding to an incremental (or linear) spin-up and spin-down. Then, the Burger number plays a preeminent role in the flow development.

Our study has revealed two very different behaviors. For Burger number > 1 (i.e., dominating stratification), three layers can be distinguished from Walin's analysis. The usual Ekman layer, adjacent to the horizontal boundary, not modified by stratification; the rotational shear layer, in which the spin of the fluid by secondary circulation is confined; the upper region, unaffected by the convective spin process, characterized by a slow velocity decrease.

We observe that the flow is remarkably axisymmetric in the bulk of the fluid in spite of the large Reynolds number ($Re \sim O(10^4)$). The Richardson number ($Ri \gg 1/4$) excludes shear instability, and thus the oscillations in the lower region of the fluid may be associated with the development of baroclinic instability. For spin-down runs, centrifugal instability is observed, but it is restricted to the sidewall region.

A comparison with the Walin's analytical solution shows that the experimental results decay faster than the theoretical prediction. Considerable discrepancies are found in the rotational shear layer, even over the shorter spin-up time scale. The early stage of the flow is correctly described by the addition of viscous-diffusion effects, but the faster decay rate of the measurements persists. The largest discrepancies between numerical and experimental velocities are found in the lower part of the rotational shear layer, suggesting that viscous-diffusion effects may produce a feedback on the secondary circulation. However, our model has captured the importance of the viscous-diffusion effects which should be included for a proper model of stratified spin-up.

For Burger numbers < 1 (i.e., dominating rotation), the rotational shear layer is not vertically limited, but occupies the whole depth of the fluid. The development of non-axisymmetric disturbances has been observed and a comparison with the Walin's theory shows a different trend with respect to the axisymmetric case. The decay is well described in the early stage by the analytical solution, but later in time the experimental results decay slower than the theoretical prediction. It has been found out that the discrepancies correspond to the onset of the instability, and thus the eddies do not allow the fluid to spin-up faster than enabled by the secondary circulation. This is in contradiction with the suggestion by Smirnov *et al.* (2005) that the large-scale eddies provide an additional mechanism for the vertical transport of angular momentum from the Ekman boundary layer. Nevertheless, at late times, stronger decay is observed, and it may be explained by radial transport of momentum from the sidewall boundary.

The longer spin-up time scale with respect to the work of Smirnov *et al.* (2005) has permitted to observe the long-wave instability at an early stage. The narrowness of their facility limits in time the development of the instability, and the sidewall boundary layers must diffuse to become sufficiently thick to allow a baroclinic motion essentially inviscid within them. The classical Eady's model is shown to be consistent with the structure of the observed waves in our experimental investigation. Its derivation by Smirnov *et al.* (2005) in cylindrical

geometry using reliable initial conditions, without considering the dynamics of the sidewall boundary, allows a reasonable estimation of the growth rate, which was untenable in the classical theory. Indeed, the mechanism of baroclinic instability becomes the most plausible explanation for the existence of the long-wave instability in spin-up and spin-down process.

A visualization of vorticity fluctuation fields associated to the large-scale eddies has been proposed, and it appears that baroclinic instability is well developed after several tens of rotation periods.

8.1 Perspectives

It would have been very hard to present a complete description of spin-up or spin-down process in stratified fluid. We focussed on viscous-diffusion effects and long-wave instability, but many other mechanisms are involved. Moreover, even in the domain investigated a deeper study would be desirable.

Our model of vertical diffusion is empirical, and consequently insufficient for a fully quantitative description of the interaction between secondary circulation and viscous-diffusion effects. It appears interesting to include viscosity more properly in the Walin's theory, and both analytical and numerical investigations would be welcome.

The inclusion of viscous-diffusion effects in the linear theory of Walin may provide an appropriate initial condition for the study of the baroclinic instability. On the other hand, it would be feasible to investigate the further development of the baroclinic instability in large facility as to obtain small viscosity effects.

Moreover, our analysis implicitly assumes that the destabilizing shear is mainly vertical, while actually both vertical and horizontal shear are present, and either may control the development of non-axisymmetric disturbances.

Appendix A

Rotating Tank Dynamics

A.1 Solid body rotation

Let us consider a cylindrical tank filled with fluid which is rotating about its vertical axis of symmetry. If both the tank and the fluid rotate rigidly with the same constant angular velocity $\vec{\Omega} = \Omega_i \hat{k}$ the motion is referred as solid body rotation. In the absolute frame of reference the fluid shows a curve motion, thus a centripetal force is acting on the fluid. This force is the pressure gradient force, due to the tilting of the free surface, directed radially inward,

$$-\frac{{U_\theta}^2}{r} = -\frac{1}{\rho}\frac{\partial p}{\partial r} \tag{A.1}$$

In the frame of reference co-rotating with the tank the fluid is at rest: a balance between centrifugal and pressure gradient force pertains along the radial direction,

$$-\frac{1}{\rho}\frac{\partial p}{\partial r} + \Omega_i^2 r = 0 \tag{A.2}$$

It is straightforward to obtain Eq.n (A.2) from Eq.n (A.1) using the relation $U_\theta = u_\theta + \Omega_i r$ which constrains the azimuthal velocities in the absolute, U_θ, and in the relative, u_θ, frame of reference. Assuming hydrostatic balance,

$$-\frac{1}{\rho}\frac{\partial p}{\partial z} - g = 0 \tag{A.3}$$

since $p = p(r, z)$

$$\delta p = \frac{\partial p}{\partial r}\delta r + \frac{\partial p}{\partial z}\delta z$$

Referring to Fig. A.1, since the free surface is an isobaric surface, in the limit $\delta r, \delta z \to 0$

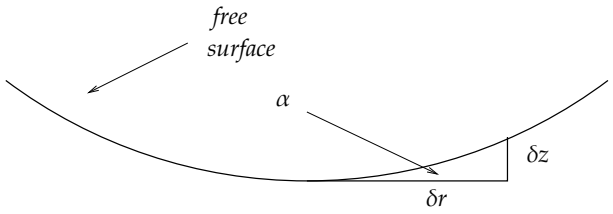

Fig. A.1: free surface in a rotating tank

$$\tan\alpha \equiv \left(\frac{\partial z}{\partial r}\right)_p = \frac{\partial H}{\partial r} = -\frac{(\partial p/\partial r)_z}{(\partial p/\partial z)_r} \tag{A.4}$$

being $H = H(r)$ the height of the free surface while rotating. Using Eq.ns (A.2) and (A.3) in a nearly homogeneous fluid ($\Delta\rho/\rho_0 \sim 10^{-2}$), Eq.n (A.4) becomes

$$\frac{\partial H}{\partial r} = \frac{\Omega_i^2 r}{g} \Rightarrow H = \frac{\Omega_i^2 r^2}{2g} + \mathbf{C} \tag{A.5}$$

being **C** a suitable constant. The value of **C** can be calculated by imposing the conservation of the fluid volume. Being H_0 the height of the fluid at rest

$$V = 2\pi H_0 \int_0^R r\mathrm{d}r = 2\pi \int_0^R H(r) r\mathrm{d}r \Rightarrow \mathbf{C} = H_0 - \frac{\Omega_i^2 R^2}{4g} \tag{A.6}$$

Substituting Eq.n (A.6) in Eq.n (A.5)

$$H(r) = H_0 + \frac{\Omega_i^2}{2g}\left(r^2 - \frac{R^2}{2}\right) \tag{A.7}$$

The value of $H(r)$ at sidewall ($r = R$) is then

$$H(R) = H_0 + \frac{\Omega_i^2 R^2}{4g} \tag{A.8}$$

A.2 Relative motion

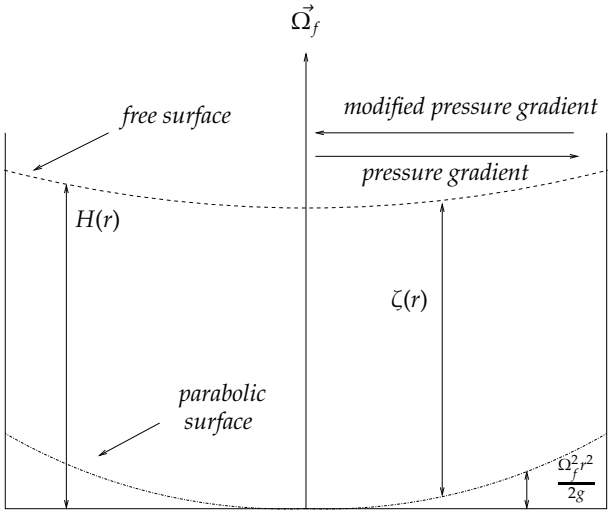

Fig. A.2: Spin-up: pressure gradient vs modified pressure gradient

After the change in the rotation rate of the tank the spin-up process, by which the fluid adjusts to the new angular velocity of the boundaries, takes place. Since the cameras co-rotate with the tank, it is convenient to consider the frame of reference rotating with the final angular velocity, Ω_f, in which the radial balance in the interior region is

$$-\frac{1}{\rho}\frac{\partial p}{\partial r} + \Omega_f^2 r \mp 2\Omega_f u_\theta + \frac{u_\theta^2}{r} = 0 \tag{A.9}$$

where u_θ is assumed positive. Eq.n (A.9) can be obtained from the radial balance (A.2), valid in the frame of reference rotating with the initial angular velocity, by means of the condition $\Omega_f = \Omega_i \pm \Delta\Omega$, being $\Delta\Omega = u_\theta / r$. In fact, the impulsive change in the angular velocity of the tank does not perturb suddenly the motion of the fluid in the interior region, far from the boundaries. Note that the curvature term u_θ^2/r is negligible in linear approximation and it will not be considered anymore. Using Eq.n (A.5) the radial balance (A.9) becomes

$$-g\frac{\partial H}{\partial r} + \Omega_f^2 r \mp 2\Omega_f u_\theta = 0 \tag{A.10}$$

Eq.n (A.10) may be simplified by writing $\Omega_f^2 r = \partial(\Omega_f^2 r^2/2)/\partial r$ and defining a quantity ζ such as

$$\zeta = H - \frac{\Omega_f^2 r^2}{2g}$$

as the level of the free surface measured relatively to the reference parabolic surface $\Omega_f^2 r^2/2g$. Then Eq.n (A.10) may be written as

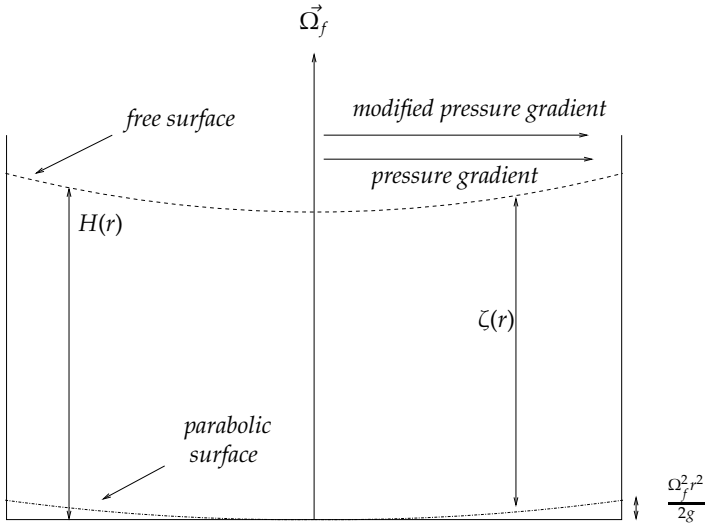

Fig. A.3: Spin-down: pressure gradient vs modified pressure gradient

$$-g\frac{\partial \zeta}{\partial r} \mp 2\Omega u_\theta = 0 \tag{A.11}$$

Obviously

$$\frac{\partial p}{\partial r} \propto \frac{\partial H}{\partial r}, \qquad \frac{\partial \tilde{p}}{\partial r} \propto \frac{\partial \zeta}{\partial r}$$

where $\tilde{p}$ is the *modified* pressure (Fig.s A.2 and A.3), which includes the centrifugal and gravitational effects

$$p(r,z) = p_0 - \rho g\Big[H(r) - z\Big] + \tilde{p}(r,z)$$

Appendix B

Data Analysis by C.I.V.

The Correlation Imaging Velocimetry technique is based on the calculation in physical space of the cross-correlation of local regions between image pairs.

Referring to Fig. B.1, the procedure starts by setting the elementary box sizes (B_x, B_y)

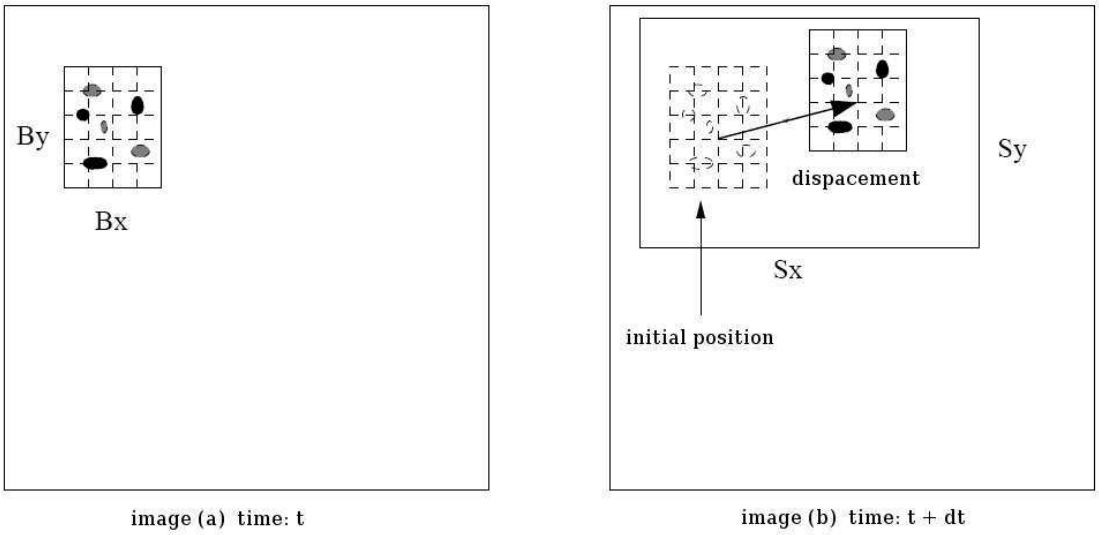

Fig. B.1: Sketch of the C.I.V. procedure.

(in pixel) on the first image (a). This box, named *pattern box*, defines the region in which correlations will be calculated along each direction (x, y). Large values lead to low spatial resolution since the velocity obtained is an average in this elementary box. The second step consists in setting the box which must contain the expected optimum pattern position on the second image (b), named *search box*. It is defined by its center, equal to zero in the absence of a

priori knowledge, and its size in each direction, (S_x, S_y). An excessive value of this range does not change the result, but it increases the computation cost, and may lead to the appearance of false vectors due to spurious covariance maxima. If the search range is too small, the true maximum covariance is missed and false vectors are obtained. The cross-correlation is then calculated with all the possible positions of the pattern box (B_x, B_y), inside the search box (S_x, S_y).

Let us consider the pixel luminous intensities $I_a(k,l)$ and $I_b(k+i, l+j)$, being $k = 1, \ldots B_x$, $l = 1, \ldots B_y$. The subscripts a and b refer to the two images between which the cross-correlation is eventually calculated. The index origin $(1,1)$ is set at the lower left-hand corner of the pattern box on the image (a). On the image (b), the pattern box is shifted from the original position by a vector (i, j) which represents the displacements allowed by the search box. The averages of the pattern box luminous intensities

$$\begin{aligned} \overline{I_a} &= \frac{1}{B_x B_y} \sum_{k=1}^{B_x} \sum_{l=1}^{B_y} I_a(k,l) \\ \overline{I_b} &= \frac{1}{B_x B_y} \sum_{k=1}^{B_x} \sum_{l=1}^{B_y} I_b(k+i, l+j) \end{aligned}$$

are subtracted to each intensity, and the cross-correlation normalized by the variance, or covariance $C(i,j)$, is computed as

$$C(i,j) = \frac{\sum_{k=1}^{B_x} \sum_{l=1}^{B_y} (I_a(k,l) - \overline{I_a})(I_b(k+i, l+j) - \overline{I_b})}{\left[\sum_{k=1}^{B_x} \sum_{l=1}^{B_y} (I_a(k,l) - \overline{I_a})^2 \sum_{k=1}^{B_x} \sum_{l=1}^{B_y} (I_b(k+i, l+j) - \overline{I_b})^2 \right]^{1/2}} \tag{B.1}$$

for each displacement (i, j) allowed by the search box. The velocity vector is then obtained as the displacement which maximizes this covariance, multiplied by the geometrical scale (*cm* per *pixel*) and the time interval. A key feature of C.I.V. technique is the interpolation of this covariance to non integer displacements in order to reach sub-pixel precision.

The velocity vectors correspond to the position at the middle between the initial pattern box center and its optimum displacement. For each point (x, y) on the measurement grid, it has coordinates $(x + \Delta x/2, y + \Delta y/2)$. The velocity field is therefore never obtained on a regular grid, but it can be referred to a regular grid by interpolation, which also provides the spatial derivatives.

A major difficulty in C.I.V. technique is the occurrence of secondary maxima of the covariance, which can spuriously exceed the maximum associated with the local displacement. One method for limiting such false velocity vectors is to restrict the search box, using some a

priori knowledge of the velocity field. This knowledge is generally provided by a first C.I.V. treatment, which can be thus refined in a hierarchical way. In fact, the results from the first C.I.V. processing can be improved in an iterative way by a succession of false vector removal, interpolation procedure, and C.I.V. processing with reduced search zone, using the estimate from the previous processing.

Under optimum conditions, the measured mean *root mean square error* on the velocity field is less than 2 %.

Bibliography

[1] B , A., L , J., P , S., W -V , A. C. Numerical experiments on stratified spin-up. *Geophys. Fluid Dyn. 7* (1975), 29–42.

[2] B , J. A. Stability of a coastal upwelling front. Part 1. Model developing and a stability theorem. *J. Geophys. Res. 94* (1989), 10844–10856.

[3] B , G. K. *An Introduction to Fluid Dynamics*. Cambridge Univ. Press, 1967.

[4] B , J. R., C , A. Spin-up. *Annu. Rev. Fluid Mech. 6* (1974), 257–280.

[5] B , W. R., W , H. A. A numerical study of time dependent rotating flows in a cylindrical container at low and moderate Reynolds numbers. *Proc. 2nd Int. Conf. Numerical Method in Fluid Dyn., Berkeley* (1971), 377–384.

[6] B , G., V , G. Spin-up of a stratified fluid: theory and experiment. *J. Fluid Mech. 50* (1971), 579–608.

[7] C , D. R., V A , C. W. Characteristics of Ekman boundary layer instabilities. *J. Fluid Mech. 44* (1970), 79–95.

[8] C , J., S , M. E. On the stability of internal baroclinic jets in a rotating atmosphere. *J. Atmos. Sci. 19* (1962), 159–172.

[9] C , J. G. The dynamics of long waves in a baroclinic westerly current. *J. Meteorol. 4* (1947), 135–162.

[10] C -R , B. *Introduction to Geophysical Fluid Dynamics*. Prentice Hall, 1994.

[11] D , P. A., G , Y., B , D. L., F , A. M. The flow generated by the rotation of a horizontal disk in a stratified fluid. *Fluid Dyn. Res. 17* (1995), 27–47.

[12] D , S. H. The stability of time-periodic flows. *Annu. Rev. Fluid Mech. 8* (1976), 57–74.

[13] D , P. W., F , M. R. Spin-up of homogeneous and stratified fluids. *Annu. Rev. Fluid Mech. 33* (2001), 231–263.

[14] E , E. T. Long waves and cyclone waves. *Tellus 1* (1949), 33–52.

[15] E , V. W. On the influence of the Earth's rotation on ocean currents. *Ark. Mat. Astron. Fys. 2* (1905), 1–52.

[16] E , V. W. Beitrage zur theorie der meeresstromungen. *Ann. d. Hydrogr. 34* (1906), 23–72.

[17] E , H. Ein neuer hydrodynamischer wirbelsatz. *Meteorol. Z. 59* (1942), 277–281.

[18] F , A. J. An experimental study of the instability of the laminar Ekman boundary layer. *J. Fluid Mech. 15* (1963), 560–576.

[19] F , A. J., E., K. R. A numerical study of the instability of the laminar Ekman boundary layer. *J. Atmos. Sci. 23* (1966), 466–480.

[20] F , A. J., K , R. E. Investigations of stability and transition in rotating boundary layers. *Dynamics of Fluids and Plasmas, Proc. Symp. in honor of Professor Johannes M. Burgers, Maryland* (1966), 309–329.

[21] F , A., D , G. Advanced optimization of correlation imaging velocimetry algorithms. *Exp. Fluids Suppl. 29* (2000), S013–S022.

[22] F , A., S , G. R. Low cost, high resolution DPIV for measurement of turbulent fluid flow. *Exp. Fluids 23* (1997), 449–463.

[23] F , J. B., B , J. W. M., U , M. An experimental investigation of spin-up from rest of a stratified fluid. *Geophys. Astrophys. Fluid Dyn. 98* (2004), 277–296.

[24] F , J. B., U , M., B , J. W. M. Spin-up from rest in a stratified fluid: boundary flows. *J. Fluid Mech. 472* (2002), 51–82.

[25] F , J. M. H. Theory and application of two supplementary methods of constructing density gradient columns. *J. Polymer Sci. 44* (1960), 505–515.

[26] F , D., L , R. R., O , G. V., B , W., K , R., W , J. Studies of thermal convection in a rotating cylinder with some implications for large-scale atmospheric motions. *Meteor. Monog. 4* (1959), 121.

[27] G , ., M C , P., R , P. Boundary mixing and arrested Ekman layers: rotating stratified flow near a sloping boundary. *Annu. Rev. Fluid Mech. 25* (1993), 291–323.

[28] G , A., G , J. S. A., S , A. Energy partition in the large-scale ocean circulation and the production of mid-ocean eddies. *Deep-Sea Res. 21* (1974), 499–528.

[29] G , A. E. *Atmosphere-Ocean Dynamics*. Academic Press, 1982.

[30] G , H. P. *The theory of rotating fluids*. Cambridge Univ. Press, 1968.

[31] G , H. P. A note on the spin-up from rest of a stratified fluid. *Geophys. Astrophys. Fluid Dyn. 15* (1980), 1–5.

[32] G , H. P., H , L. N. On a time-dependent motion of a rotating fluid. *J. Fluid Mech. 17* (1963), 385–404.

[33] H , R. An experimental study of thermal convection in a rotating liquid. *Phil. Trans. Roy. Soc. A 250* (1958), 441–478.

[34] H , J. R. The influence of viscous boundary layers on transient motions in a stratified rotating fluid. *J. Atmos. Sci. 22* (1965), Part I, 402–411.

[35] H , J. R. *An Introduction to Dynamic Meteorology*. Academic Press, 1992.

[36] H , J. R., S , P. H. A note on the spin-up of a stratified fluid. *J. Fluid Mech. 33* (1968), 127–129.

[37] H , J. M. Axisymmetric flows in spin-up from rest of a stratified fluid in a cylinder. *Geophys. Astrophys. Fluid Dyn. 23* (1983), 127–141.

[38] H , J. M. Flows within the Ekman layer during spin-up of a thermally stratified fluid. *Geophys. Fluid Dyn. 29* (1984), 65–79.

[39] H , J. M., F , W. W., W -V , A. Numerical solutions for the spin-up of a stratified fluid. *J. Fluid Mech. 117* (1982), 71–90.

[40] K , I. A laboratory study of columnar baroclinic vortices in a continuously stratified fluid. *Dyn. Atmos. Oceans 38* (2004), 69–92.

[41] K , P. K. *Fluid Mechanics*. Academic Press, 1990.

[42] K , H. L. Dynamic instability of two-dimensional nondivergent flow in a barotropic atmosphere. *J. Meteor. 6* (1949), 105–122.

[43] L , S. M. *An investigation of stratified spin-up using a rotating laser-Doppler velocimeter*. M.S thesis, Florida State University, 1975.

[44] L , D. K. On the instability of the Ekman boundary flow. *J. Atmos. Sci. 23* (1966), 481–494.

[45] L , P. F. The flow of a stratified fluid in a rotating annulus. *J. Fluid Mech. 79* (1977), 435–447.

[46] L , J. M. Flow between a stationary and a rotating disk shrouded by a co-rotating cylinder. *Phys. Fluids 8* (1996), 2605–2613.

[47] L , J. M., W , P. D. Stability of stationary endwall boundary layers during spin-down. *J. Fluid Mech. 326* (1996), 373–398.

[48] M C , P., R , P. B. Buoyant inhibition of Ekman transport on a slope and its effect on stratified spin-up. *J. Fluid Mech. 223* (1991), 631–661.

[49] M D , B. E., D , R. H. Solar oblateness and fluid spin-down. *Science 158* (1967), 1562–1564.

[50] M L , A. R. The unsteady motion produced in a uniformly rotating cylinder of water by a sudden change in the angular velocity of the boundary. *Phil. Mag. 44* (1922), 1–14.

[51] M N , B., C , A., E , Z. A., M , R. W., P , J., S , K., S , W. H. Design and construction of an affordable rotating table for classroom demonstrations of geophysical fluid dynamics principles. *B. Am. Meteorol. Soc. 84* (2003), 1827–1834.

[52] M , J. L., N , J. E. Buoyancy and solar spin-down. *Science 166* (1969), 291–291.

[53] M , F. Y., F , J. B. On the spin-up by a rotating disk in a rotating stratified fluid. *J. Fluid Mech. 516* (2004), 155–180.

[54] M , R. J., D , P. A. The flow generated in a continuosly stratified rotating fluid by the differential rotation od a plane horizontal disc. *Fluid Dyn. Res. 38* (2006), 522–538.

[55] N , G. P., D , S. H. Centrifugal instabilities during spin-down to rest in finite cylinders. numerical experiments. *J. Fluid Mech. 102* (1981), 329–352.

[56] P , J. The spin-up of a stratified fluid. *J. Fluid Mech. 28* (1967), 463–479.

[57] P , J. Flow in rotating stratified systems. *Notes on the 1970 Summer Prog. Geophys. Fluid Dyn. Woods Hole Ocean. Inst. 1* (1970), 1–67.

[58] P , J. *Geophysical Fluid Dynamics*. Springer-Verlag, 1987.

[59] P , H. Über das sogenannte schaumrandphänomen. *Göteb. Kungl. Vetensk. Vitterh.-Samh. Handl. 2* (1931), 1–21.

[60] R , C. G. On the mutual adjustment of pressure and velocity distributions in certain simple current systems. *J. Marine Res. 1* (1938), 239–263.

[61] S , T. Spin-down of boussinesq fluid in a circular cylinder. *J. Phys. Soc. Japan 26* (1969), 840–848.

[62] S , T. Spin-down problem of rotating stratified fluid in thermally insulated circular cylinders. *J. Fluid Mech. 37* (1969), 689–699.

[63] S , T., C , A., C , P. A. A note on spin-down of boussinesq fluid in a circular cylinder. *J. Phys. Soc. Japan 30* (1971), 1517–1517.

[64] S , T., C , A., C , P. A. Spin-down of a boussinesq fluid of small Prandtl number in a circular cylinder. *J. Fluid Mech. 49* (1971), 753–773.

[65] S , W. S. Görtler vortices. *Annu. Rev. Fluid Mech. 26* (1994), 379–409.

[66] S , K. D., B , R. C. An experimental study of the spin-up of a thermally stratified rotating fluid. *Geophys. Fluid Dyn. 7* (1975), 1–28.

[67] S , W. L. The spin-down of rotating stratified fluids. *J. Fluid Mech. 47* (1971), 689–711.

[68] S , S. A., B , P. G., B , D. L., V , S. I., S -M , A. N. Long-time evolution of linearly stratified spin-up flows in axisymmetric geometries. *Phys. Fluids 17* (2005), 016601.

[69] S , D., S , J., D , G. A tsai's model based S-PIV method for velocity measurements in a turbulent Ekman layer. *Under consideration for publication in Exp. Fluids* (2008).

[70] S , G. S. M., F , M., D , P. The transient response of a contained rotating stratified fluid to impulsively started surface forcing. *J. Fluid Mech. 243* (1992), 33–50.

[71] T , P. R., M -C , E. L. Experiments on Ekman layer instability. *J. Fluid Mech. 20* (1967), 531–543.

[72] T , G. I. Motions of solids in fluid when the flow is irrotational. *Proc. Roy. Soc. A 93* (1917), 99–113.

[73] T , R. Y. An efficient and accurate camera calibration technique for 3d machine vision. *Proc. IEEE Conf. on Computer Vision and Pattern Recognition, Miami Beach* (1986), 364–374.

[74] W , G. Some aspects of time-dependent motion of a stratified rotating fluid. *J. Fluid Mech. 36* (1969), 289–307.

[75] W -V , A., F , W. W., P , S., L , S. M. Numerical solutions and laser-Doppler measurements of spin-up. *J. Fluid Mech. 85* (1978), 609–639.

[76] W , P. D. On the spin-up and spin-down of a rotating fluid. Part 2. Measurements and stability. *J. Fluid Mech. 77* (1976), 709–735.